UNIVERSITÀ DEGLI STUDI DI NAPOLI
FEDERICO II

Scuola Politecnica e delle Scienze di Base
Dipartimento di Ingegneria Elettrica e Tecnologie dell'Informazione

DOCTORAL THESIS

Analysis and Control of Bacterial Populations in Synthetic Biology

Author:
Agostino Guarino

Tutor:
Prof. Mario di Bernardo

Co-Tutor:
Dr. Davide Fiore

Submitted in fulfilment of the requirements for the degree of Doctor of Philosophy in Information Technology and Electrical Engineering, XXXIII Ciclo.
Coordinator: Prof. Daniele Riccio.

30 April 2021

To Mattia,
grow strong,
dive deep,
have fun.

Abstract

Synthetic Biology is a new field of research that aims at engineering new functionalities in living beings. Analogously to electronic circuits, more advanced functionalities can be realised by putting together smaller functional modules that perform elementary tasks; however, the interaction of these basic pieces is somewhat complex and fragile. Therefore, to increase the robustness and reliability of the whole system, typical tools from Control Theory, such as feedback loops, can be employed. In the first part of this thesis we propose feedback control strategies to balance the gene expression of a bistable genetic circuit, known as *genetic toggle switch*, in an unstable region far away from its stable equilibria – a problem analogous to the stabilization of the inverted pendulum in mechanics. The effectiveness of the proposed control strategies is validated via realistic agent-based simulations of a bacterial population endowed with the genetic toggle switch. Later in the thesis we move towards the growth control of bacterial cells in bioreactors, introducing a novel open-source and versatile design of a turbidostat to host *in vivo* control experiments. In the last part, we want to control bioreactors to guarantee the coexistence of multiple species in the same environment. We analyse the dynamics of a simple one-chamber bioreactor, proposing control strategies to achieve the control goal. However, simple bioreactors have several drawback when the concentrations of multiple species are regulated at the same time; for these reason, we propose a novel layout for a bioreactor, with two growth chambers and a mixing one, to be used in multicellular *in vivo* control experiments.

Acknowledgements

I sincerely would like to thank Professor Mario di Bernardo, who tutored me with passion, wisdom and patience during these years. He contributed significantly to this work but, most importantly, to my personal and professional development; I will be always grateful to him and to all the people in his research group. In particular, I would like to thank Dr. Davide Fiore for being my mentor since the first day and a very good friend as well. I would like to thank Dr. Fabio Della Rossa from Politecnico di Milano for the helpful discussions and for his precious support. A special thanks to Dr. Maria Lombardi, Fabrizia Auletta and all the people at the University of Bristol, who made me feel home far away from home. I thank my family, endless source of love and support, steady as a backbone. A special thanks to my beloved grandparents, passed away during these years but always a constant presence in my heart.
Part of this work has been conducted during the Covid-19 pandemic, a dramatic event that twisted our lives changing the World as we used to know it. I wish to thank all the people and all the friends who fought with me against loneliness, isolation and frustration. *Dulcis in fundo*, thanks to the flame that kindled my joy and love during these months, whatever lives have in store for us.

The author acknowledges support from the research project COSY-BIO (Control Engineering of Biological Systems for Reliable Synthetic Biology Applications) funded by the European Union's Horizon 2020 research and innovation programme under grant agreement No. 766840.

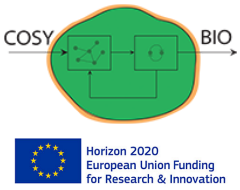

Contents

1 Introduction

The last decades saw a significant increase in the number of applications of engineering tools and techniques to the field of biology, which gave rise to the new and promising research field of *system biology*.

Systems biology [79] involves both computational and mathematical methods to model complex biological systems supporting the analysis of experimental data. In this context, the process of production of proteins from the instructions contained in the *genome* is seen as a *complex system* made up of interacting biological modules [78]; the interactions between these components let *collective behaviours*, such as *life*, emerge. The aim of system biology is to study protein interactions formulating sets of differential equations that describe their dynamics [26]; the parameters of the equations are related to the speed of the reactions in the system and can be determined by experiments and by applying computational techniques [140, 24]. Similarly, *bioinformatics* [94] aims at developing methods and tools to understand biological data combining elements from computer science.

While in systems biology and bioinformatics engineering tools are applied and developed to enhance the comprehension of living beings, *synthetic biology* [15, 21, 37] aims at creating new life forms, or at modifying existing ones to provide new functionalities to living organisms, by engineering and embedding into them new *gene regulatory networks* (GRN). Biological pathways that behave in a way that mimic memory elements, oscillators, logic gates or more complex electrical circuits have been designed [74]. In general, GRNs can be combined as functional modules to build more advanced and larger systems; however, the more complicated the system, the more prone to noise and fragile it becomes [137]. The disruptive effects of stochastic noise, cell-to-cell variability, retroactivity, metabolic burden, and other unobservable phenomena can be mitigated by adopting feedback loops [17]. For these reasons, *control theory* tools – such as feedback control – are of crucial importance in the creation of new synthetic living beings.

Gene expression is the fundamental mechanism by which the information stored in the DNA is converted into proteins, determining the behaviour of the cells [29, 30], so that living beings are capable of responding to changing envi-

ronments, to external signals, and other stimuli. The first scientific question we address in this thesis is to understand whether it is **possible to steer the behaviour of living cells via feedback control strategies in a robust and reliable manner. If so, it is of utmost importance to investigate how these strategies can be designed to tackle the unavoidable process uncertainties.** To answer this question, we will focus on the *genetic toggle switch*, a bistable *gene regulatory network* made up by two proteins that repress each other's promoter. For its intrinsic bistable nature, the genetic toggle switch has been recognised as the biological version of the inverted pendulum [93, 72], being a valuable *test bench* for the control of GRNs. In particular, we propose feedback control strategies for its stabilization in an unstable region of its state space far away from its stable equilibrium points.

Due to some limiting factors, such as excessive metabolic burden, competition of limited resources or incompatible chemical reactions, complex functionalities can sometimes not be implemented in a *single cell*. A chance to overcome these limitations is offered by *multicellular systems* where a "desired goal" can be achieved via a distribution of the tasks (and their metabolic burden) over different subpopulations of cells [16]. In this way, two or more bacterial populations cooperate to achieve a "common goal", forming a *microbial consortium*. Recent examples of consortia include prey-predator systems [11], oscillators [28] and a feedback control loop where the functions are split between species [46]. However, due to unavoidable differences in the cell growth in the populations constituting the consortia it is necessary to stabilize their co-culture. *Ad hoc* regulation mechanisms can be embedded into cells [117]; however, especially in industrial applications, some external regulation strategies may be preferred to avoid the additional metabolic burden introduced by *embedded* solutions. Therefore, the second objective of this thesis is to **design control strategies for bioreactors to guarantee coexistence and regulate the ratio of competing bacterial populations in the same environment.** In this thesis we analyse the dynamics of two competing bacterial species in the same environment to reveal the conditions that lead to their coexistence. Then, we propose control strategies that guarantee their stable coexistence and regulate the ratio of the two populations, validating their effectiveness via *in silico* experiments. The resulting closed-loop systems exhibit at times slow dynamics that are incompatible with the time scale of *in vivo* experiments; therefore, to overcome these limitations, we formulate the mathematical model of a new chemostat layout and propose a possible control strategy that shows promising results in simulations.

1.1 Outline of the Thesis

This thesis can be conceptually divided into two parts: the first is focused on the external control of some cell *phenotype* while the second is concerned with *growth control* and the regulation of the ratio of two competing bacterial populations in the same chemostat.

Chapter 2 illustrates the state of the art on the control of bacterial populations endowed with synthetic gene regulatory networks.

In Chapter 3, the analysis and the external control of the *genetic toggle switch* is discussed; after deriving a simplified mathematical description of the system, we propose two control strategies to balance the expression of the two repressor proteins in a target region of its state-space. The proposed control strategies are then validated via extensive *in silico* experiments and their performances quantified and compared using some aggregate indexes. The results of this Chapter have been presented in [44]; the control strategies have been published in [56, 57].

The focus of Chapter 4 is on bioreactors used to conducts *in vivo* experiments. We present an open-source modular design of a *turbidostat*, which is a bioreactor with a closed control loop that regulates the *turbidity* of a cells solution. The device we assembled has a 3D printed structure and is controlled by an *Arduino* microcontroller; these characteristics make the device very flexible and *easy to extend*, while keeping the total assembly cost under $200. The work has been conducted during a 3 month visiting period at the University of Bristol, in collaboration with Dr. Barbara Shannon; results from this Chapter were presented in [58].

In Chapter 5 control strategies are designed to regulate the density of two competing cell populations in a bioreactor. After showing the strong limitation of a simple one chamber set-up, we propose a new three chambers layout – with two growth chambers and a mixing one where the species coexist – and a simple control strategy that shows good performances in *in silico* experiments. Part of the results were obtained in collaboration with Dr. Davide Fiore and Dr. Fabio Della Rossa from Politecnico di Milano and are available in [43].

Conclusions are drawn in Chapter 6. Appendix A provides further details about the design of the turbidostat shown in Chapter 4.

In order for each Chapter to be self contained, the relevant background is given at its beginning rather than all being collected in Chapter 2.

1.2 Research Products

During the PhD course, the following works were published in journals or conference proceedings:

1. Davide Fiore, Agostino Guarino, and Mario di Bernardo. "Analysis and control of genetic toggle switches subject to periodic multi-input stimulation." *IEEE Control Systems Letters* 3(2): 278-283, 2019. Also *IEEE Conference on Decision and Control 2018*.
2. Agostino Guarino, Davide Fiore, and Mario di Bernardo. "In-silico feedback control of a MIMO synthetic toggle switch via pulse-width modulation." In Proc of the *2019 18th European Control Conference (ECC)*, pages 680-685 2019.
3. Agostino Guarino, Barbara Shannon, Lucia Marucci, Claire Grierson, Nigel Savery, and Mario di Bernardo. "A low-cost, open-source turbidostat design for in-vivo control experiments in synthetic biology." *IFAC-PapersOnLine*, 52(26):244–248, 2019. Also discussed in *8th IFAC Conference on Fundations of Systems Biology in Engineering (FOSBE) 2019*.
4. Agostino Guarino, Davide Fiore, Davide Salzano, and Mario di Bernardo. "Balancing cell populations endowed with a synthetic toggle switch via adaptive pulsatile feedback control." *ACS Synthetic Biology*, 9(4):793–803, 2020.
5. Fabio Della Rossa, Davide Salzano, Anna Di Meglio, Francesco De Lellis, Marco Coraggio, Carmela Calabrese, Agostino Guarino, Ricardo Cardona-Rivera, Pietro De Lellis, Davide Liuzza, Francesco Lo Iudice, Giovanni Russo and Mario di Bernardo. "A network model of Italy shows that intermittent regional strategies can alleviate the COVID-19 epidemic." *Nature Communications* 11(1):1–9, 2020.
6. Davide Fiore, Fabio Della Rossa, Agostino Guarino, Mario di Bernardo. "Feedback ratiometric control of two microbial populations in a single chemostat." Submitted to *IEEE Control Systems Letters*. Preprint available on bioRxiv [43].

2 State of the Art on Control of Bacterial Populations

In this Chapter we review the state of the art on the control of bacterial populations. We introduce the problem that will be addressed in Chapter 3 and we discuss, in broader terms, the most relevant techniques for the control of bacteria in microfluidics devices and bioreactors.

2.1 Gene Regulatory Networks

Gene expression is the cellular process that allows the production of proteins from the information encoded in sequences of nucleotides called *genes* [112]. Sequences of genes and their spatial distribution in the genome regulate the behaviour of cells, serving as target sites for transcription factors. In this sense, regions of DNA can be seen as unitary control modules, receiving inputs from the environment and producing proteins, that can be interconnected to form complex networks [3, 69]. By collecting and analysing gene expression data it is possible to infer networks of genes that describe complex gene expression dynamics [40]. These networks, known as *gene regulatory networks* (GRNs), are logic maps or "blueprints" that describe the relationship between transcriptional regulatory activities and some inputs [87].

The high degree of complexity of large-scale genetic networks can be handled by decomposing the whole system into modules [116, 122] that are interconnected through input and output signals. This point of view raises an interesting analogy between electrical and genetic circuits [98, 99]: as electronic engineers design circuits, genetic network engineers can use biologically equivalent modules to assemble gene regulatory networks to control cellular functions [71]. Over the past decades, simpler modules have been combined to obtain larger systems that behave similarly to electronic circuits. This is the case of memory-like circuits [53, 136], counters [50], logic gates [59, 144], oscillators [39] and others.

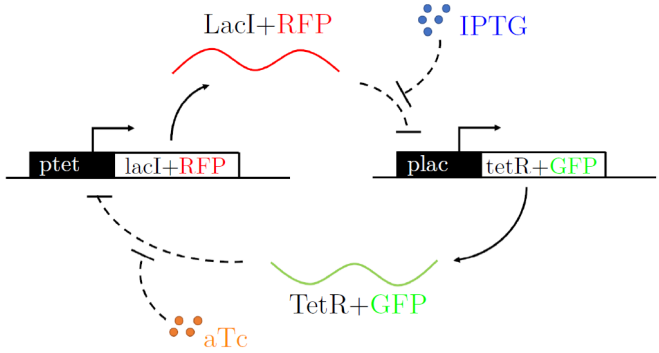

Figure 2.1: Schematic of the genetic toggle switch circuit structure as presented in [93]. The two genes (LacI and TetR) – respectively bound with RFP(mKate2) and GFP(mEGFP) – mutually repress each other; the external inducers, IPTG and aTc, modulate the strengths of the repression exerted by LacI and TetR on each other.

Among all the synthetic GRNs that were implemented over the last few decades, two networks raised significant interest: the *repressilator* [39] and the *genetic toggle switch* [53]. The repressilator is a GRN composed by at least three genes arranged in a closed sequence where each gene represses its successive one; in this way, the network forms a *feedback loop* through *transcriptional receptors*. Hence, its design emulates an electrical circuit that exhibits stable oscillations with fixed period [19]. The repressilator was implemented in *E. coli* bacteria to build an artificial circadian clock that mimics its natural counterpart and it is currently the object of research to study synchronization [52], neurodegenerative diseases [66], and growth abnormalities in cancer cells [133]. The genetic toggle switch, which will be used as a benchmark system in the rest of this thesis, will be described next.

2.1.1 The Genetic Toggle Switch

The genetic toggle switch (GTS), as first described in [53] and shown in Figure 2.1, consists of two repressor proteins and two constitutive promoters. Both proteins repress each other's promoter, so that only one is fully expressed at any time. The mutually inhibitory actions make this system intrinsically bistable; in the absence of external inducers, the system settles onto one of the two stable states where one protein is fully expressed, while the other is repressed. A saddle point corresponding to an equilibrium where neither of the two reporter proteins is fully expressed is also possible, with its stable manifold separating the basins of attraction of the two stable equilibria. The switch from one stable state to the other is possible by acting on the external inducers, reducing the inhibitory actions of the proteins over the promoters.

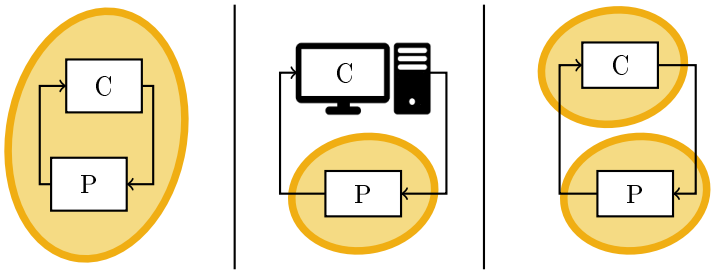

Figure 2.2: Left panel: In-cell *embedded* feedback control implementation. The process and the controller are implemented by biomolecular reactions embedded in the same cell. Central panel: *In silico* feedback control implementation. The process is embedded in the cell while the controller is implemented in an external architecture. Right panel: *Multicellular* feedback control implementation. The process and the controller are implemented in two different cells.

Concerning its implementation, the toggle switch is commonly implemented via a single plasmid, although it is possible to separate its components in different plasmids without altering its functionalities [53]. This idea of separation has inspired a recent implementation of the toggle switch across a microbial consortium [118].

Since its design in the year 2000, the GTS has played a fundamental role in synthetic biology, especially in the study of cell differentiation [51, 148, 120, 84] and decision making [5, 27]. Its importance comes from its ability to endow host cells with memory of some previous stimulus reporting this information as high expression rate of a specific repressor protein [53, 138, 147, 64].

2.2 Control of Bacterial Populations

In synthetic biology, biomolecular circuits are embedded in living cells with the aim of steering cellular behaviour so as to realize new functionalities with relevant applications in different fields of Science and Technology, from energy, to environment, to medicine [21]. However, the inner nature of the biological components, which are non-linear, stochastic, and uncertain, undermines the modularity of the biomolecular processes; hence, the realization of synthetic biomolecular circuits is often a lengthy and ad hoc process [23]. To tackle these problems, control theory techniques have been applied to engineer these systems, guaranteeing modularity of the whole systems and its reliability in real applications.

Although promising results have been achieved, the implementation of robust and reliable biological systems can be cumbersome. Indeed, there is no method to simply translate existing theories developed for control systems directly to a biomolecular setting [36]. Currently, control systems to modify gene expression in cells can be realised according to three different paradigms [76], visually reported

in Figure 2.2. A first architecture (see Figure 2.2, left panel) – known as *internal* or *embedded* control – consists of endowing the same cell with both the functional blocks in the classical control schematic, the *process* P and the *controller* C. The exchange of information, which is the state of the process (or its output) and the control input, remains confined inside the cell without passing through the cell membrane. A second architecture (see Figure 2.2, central panel) requires external devices to control the process embedded in the cell; for this reason, it is known as *in silico* or *external* control. The state of the process is measured via an external sensor (i.e., a microscope) and is sent to a computer (the controller) that evaluates the control input to be applied to the system. The input can be actuated using different methods, such as via inducer molecules or optogenetics techniques. The last paradigm is one known as *multicellular control* (Figure 2.2, right panel) and consists of the separation of the functional blocks in different cells. Commonly, a species is endowed with the process P and another one with the controller C, forming together a microbial consortium. The communication between the functional blocks requires a mechanism of intracellular communication, such as *quorum sensing* [104]. Obviously, in this paradigm, the feedback loop exists only when the two population of cells coexist in a stable manner, with the extinction of one of the two resulting into a failure of the control strategy.

In the following sections we will review the state of the art of the three control architectures for biological systems presented above, showing the most relevant results and discussing the advantages and limitations of each paradigm.

2.2.1 Embedded Control

Emdedded control strategies consist of designing and directly embedding into the cells new genetic circuits that modify their behavior so that a genetic process of interest can be regulated as desired. The first result, in this sense, was in the early years of synthetic biology when a negative feedback loop was constructed in *E. coli* [14], achieving stable regulation and reducing variability. Following the results obtained in bacteria, negative feedback loops have been implemented also in *yeast* [12] and *mammalian* cells [124]. Comprehensive reviews of embedded controllers can be found in [76, 36, 67].

Recently, embedded *antithetic feedback controllers* [89, 7] in *E. coli* raised lots of interests, showing perfect rejection of constant disturbances by means of a biological *integral control action*. In *E. coli*, the implementation of a quasi-integral feedback controller is reported in [2] and two negative feedback circuits have been proposed and validated in [73]. However, the implementation of embedded controllers requires several conceptual and practical problems to be addressed. Some of the main challenges are the presence of *intrinsic stochastic noise*, the *context dependence* of the parameters of the cells, the *lack of knowledge* of some network topologies, and, especially, the *excessive metabolic burden* to which the cells are exposed.

2.2.2 In Silico Control

In silico controllers require an external architecture to close a feedback loop over the process embedded into cells, (see central panel in Figure 2.2). The external architecture is essentially composed of three elements: a *sensing device*, a *computer*, and an *actuator*. The sensing device (i.e., a microscope) is required to measure or estimate the state of the process; this is usually done by evaluating the expression of some fluorescent reporters. The computer evaluates the control input on the basis of the measure and the setpoint of the experiment. The actuators deliver the control law to the system; different actuation solutions have been used, such as *optogenetics* or regulation of *external inducers*.

Over the years, different synthetic genetic components that tune transcription processes on the basis of light stimuli they sense have been developed [90]. Optogenetics [35], by exploiting these components and controlled light sources (i.e., LEDs), allows for the fast control – on the order of milliseconds – of gene regulatory networks. A first example of a feedback loop based on this technology was been demonstrated in yeast cells in 2002 [123]. In bacteria, over the last few years, several applications of optogenetics have been proposed to achieve dynamic regulation of gene expression [103, 102, 101, 110, 109]. The applications of optogenetics, however, are not limited to the control of synthetic gene regulatory networks but include other fields such as neuronal control. The fast-scale and the versatility of this technique makes it suitable for a large number of potential applications; however, in reality, phenomena like *selective expression*, *light absorption spectrum* interferences, and *spatial response* are open problems that require further studies [150].

Alternatively to optogenetics techniques, cells can be controlled by an external system that pumps *inducer molecules* into the media where the cells are hosted and grow. Advantages of this control method are its versatility and scalability: it can be applied to microfluidics set-ups using controlled syringe pumps as well as large continuous bioreactors using peristaltic pumps [80]. *Microfluidics* offers several advantages in terms of costs – working with limited volumes reduces the quantities of reagents needed in the experiments – and in terms of control – the small microfluidic chamber is continuously monitored by a microscope, allowing for real-time quantification of reporter proteins [76]. Over the years, control with microfluidics-based inputs demonstrated its effectiveness in several applications [113, 114, 48, 93, 47]. Theoretically, these examples of feedback controllers implemented in microfluidics can be scaled up to larger bioreactors; in doing so hard practical challenges need to be addressed. In particular, the bottleneck is the measurement process: usually, in larger bioreactors, samples of the solution must be taken and analysed via *fluorescence activated cell sorting* (FACS) [62], which is a slow process that introduces long delays in the control loop. In the last few years, techniques to speed-up the measurement process have been proposed [85, 88], however their implementation costs limit their diffusion. Alternatively, new bioreactors have been developed and embedded with fluorescent measuring circuits [130], allowing real-time monitoring of reporter proteins [131].

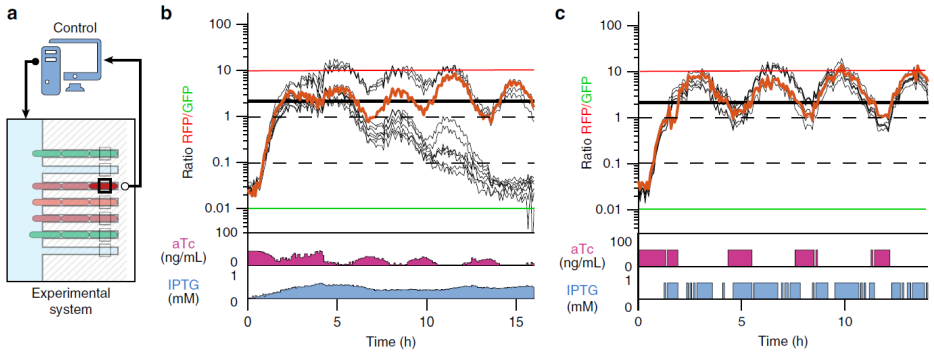

Figure 2.3: *In-Silico* control strategies proposed by *Lugagne et al.*; figure taken from [93]. Panel **a**: Experimental control principle. The external controller uses fluorescence measures of a single cell to compute the control inputs. Panel **b**: Ratio of RFP (*LacI*) and GFP (*TetR*) levels of the controlled cell (in orange) and of the other 11 cells in the population (black), when controlled by the *PI* controllers. Panel **c**: Ratio of RFP (*LacI*) and GFP (*TetR*) levels of the controlled cell (in orange) and of the other 11 cells in the population (black), when controlled by the *Bang-Bang* controllers.

In-Silico Control of the Genetic Toggle Switch

The problem of controlling the toggle switch dynamics has been the subject of many papers in the literature, and was highlighted by *Lugagne et al.* [93] as the genetic equivalent of controlling an inverted pendulum. Pulse Shaping Control [126, 128, 127] and Reinforcement Learning control approaches [129] were both proposed to drive the system from a stable equilibrium to the other. Stochastic Motion Planning [41] and Piecewise Linear Switched Control [25] were used to stabilize the circuit around its unstable equilibrium. In all these cases, however, the results are only tested *in-silico* and no experimental validation is provided.

Lugagne et al. [93] demonstrated the potential of *external* feedback control strategies by stabilizing a population of toggle switches in a region near its unstable equilibrium for an extended period of time; to do so, *in-vivo* control experiments were conducted in a microfluidic device (see Figure 2.3, panel **a**). In this work, the authors at first propose two *proportional-integral* (PI) controllers to regulate the expression of the fluorescent proteins (RFP bounded with *LacI* and GFP bounded with *TetR*) at target levels close to the unstable equilibrium, succeeding in the stabilization of a single cell but with the rest of the population committing to either one of the two stable states (see Figure 2.3, panel **b**). Then, they proposed a *Bang-Bang* control strategy that showed excellent control result while being technically less challenging to implement, succeeding in their control goal (see Figure 2.3, panel **c**). This efficiency, however, comes with the limitation that only a single cell can be controlled at a time with the control inputs

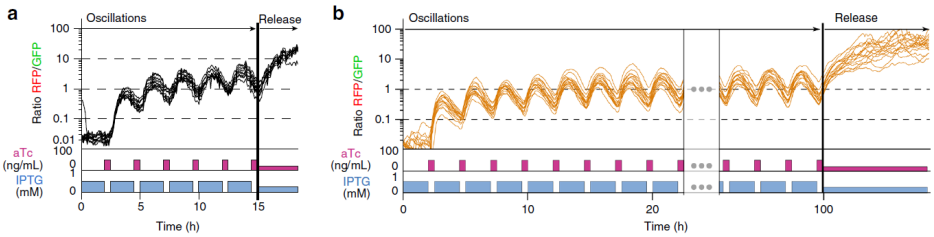

Figure 2.4: A cell population can be maintained in a state of balanced expression using periodic stimulations; figure taken from [93]. Panel **a**: Ratio of RFP (*LacI*) and GFP (*TetR*) levels for 8 observed cells. The concentrations of the inducers were varied periodically (120 min of 0.5mM IPTG, 30 min of 50 ng/ml aTc). In such dynamic conditions, the cells were kept in a state of balanced expression. As soon as the periodic stimulation was stopped, with aTc and IPTG set back to their reference levels, the cells were attracted to the RFP-dominant state. Panel **b**: In silico experiment (stochastic simulation) in which periodic stimulation was applied as in panel **a** to a simulated population of 16 cells implementing a stochastic version of the toggle switch model and showing a similar behaviour.

(aTc and $IPTG$) computed on its trajectory and being probably inappropriate to drive the other cells. In principle, controlling several cells simultaneously would require the application of a specific input for each cell. However, as it is possible to stabilize different pendulums (with different masses and lengths) in their upward positions by applying them the same mechanical force, the authors proved that a single periodic forcing can be used to dynamically stabilize the population of switches in a target region. Therefore, they noted that, for carefully chosen periods and duty-cycles of two open-loop mutually exclusive pulse wave inputs, it was indeed possible to stabilize an entire population of switches in an unstable region (see Figure 2.4, *in vivo* experiments in panel **a**, *stochastic simulations* in panel **b**). Too fast, or too slow, periodic stimulations lead cells to eventually commit to either one of the two stable states. Therefore, the problem remains of how to select the required features of the inputs and also of guaranteeing greater robustness given that the proposed strategy is open loop.

We propose a solution to this problem in Chapter 3 where *ad hoc* feedback controllers will be designed to steer the dynamics of a cell population endowed with a genetic toggle switch.

2.2.3 Multicellular Control

Embedded controllers can often be hard to integrate into a single cell due to the excessive metabolic burden placed on the host [82, 145]. Another limiting aspect is that any change in the control strategy requires re-engineering of the entire control system; this paradigm results in poor modularity and adaptability of the design and its parts [95]. Distributing the components of the control system, as in Figure 2.2 right panel, across multiple species in a microbial consortium is a promising solution to overcome these limitations. This alternative concept goes under the name of *multicellular control*.

In the multicellular control paradigm, a "controller" species receives the "measures" and regulates a "target" cell population, realising a feedback control loop. A key element that must be present in the controller species is a sort of biological comparator to evaluate the "difference" between a "reference" signal and the measure of the target population output; an example of biological comparator were implemented in *E. coli* in [6]. In order to close the loop, the two populations must be able to communicate to exchange information about their state and the control input. Usually, this is accomplished by keeping the two populations in the same solution while they exchange *quorum sensing* molecules. An implementation of this control architecture has been proposed in [47], which validated its effectiveness via *in silico* experiments.

Multicellular control strategies have shown promising results in several applications. In [9] coordinated self-organization of cells in patterns has been demonstrated. Control strategies to control cell growth and regulate populations at a desired equilibrium has been proposed in [121]. Other examples include maintaining the density of *E. coli* at a desired level via a population control circuit [149] or via a feedback control strategy [117]. In [42] a co-culture is controlled by a single strain of bacteria expressing and secreting a bacteriocin that targets a competitor. Recently, a multicellular feedback control strategy has been proposed to toggle a population of genetic toggle switches [45].

In this Chapter we presented the state of the art on control of bacterial populations, discussing the different control techniques and the results achieved in the literature. In the next Chapter, we design external feedback control strategies to balance the genetic toggle switch in a region of its state space where none of its two competing proteins are fully expressed.

3 External Control of the Genetic Toggle Switch

3.1 Introduction

The *genetic toggle switch* (GTS) has been highlighted as a fundamental synthetic circuit to endow cells with memory-like features [64] or to differentiate mono-strain cultures into different populations [51, 148, 120, 84]. A crucial problem in all reversible bistable systems is the ability to reset their state by means of appropriate inputs to balance the system in an indeterminate state located in between the two stable states. A striking example is *dedifferentiation* in stem cells applications [20, 111] where a terminally differentiated cell reverts and is maintained as an undifferentiated stem cell.

In this Chapter, we consider the problem of balancing the genetic toggle switch in a region surrounding its unstable equilibrium by manipulating two external inputs that can affect its dynamics. Solving this problem was suggested as an important benchmark [93] in the applications of control theory to synthetic biology, similar to that represented by the classical inverted pendulum (cart-pole) stabilization in control engineering [72]. The control strategies we propose to deal with the problem fall in the class of *external control* strategies, given the architecture they require to operate; their implementation needs a microfluidic device to host the living population of bacteria, a sensing unit that is a fluorescence microscope to measure the state of the system and actuated syringes to deliver the input, see Figure 3.1. A microfluidic chamber traps and hosts a population of *E. coli* endowed with the genetic toggle switch feeding it with the inducers received from a connected actuation system made up of controlled automated syringes. Through a fluorescence microscope that takes pictures of the cells, the average red and green fluorescence proteins values (namely, RFP and GFP) are evaluated through segmentation algorithms and sent to the controller. A control algorithm compares the fluorescence values with the setpoint of the experiment and computes online the inputs to be delivered in the solution with the cells. The control signal is then passed to the actuators that produce the action needed to feed the population of cells in the chamber.

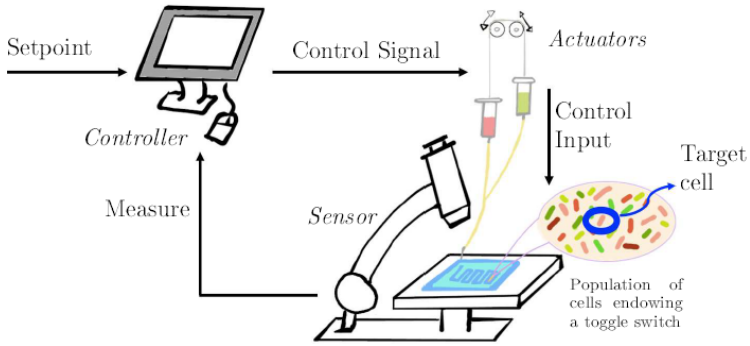

Figure 3.1: Architecture of the external feedback control of cell populations in microfluidic platform: basic elements of an experimental platform.

Recently, it was experimentally observed [93], and later proved analytically [44], that a specific class of *pulsatile periodic inputs* with carefully selected periods, duty-cycle and amplitudes can be used to dynamically balance a population of cells, endowed with a genetic toggle switch, in a region close to their unstable equilibrium point. To achieve this goal, it is indeed necessary to use time-varying input signals as, for the particular implementation of the toggle switch considered in this Chapter, stabilization near the unstable equilibrium has been proved impossible by means of constant control inputs [92]. Moreover, when periodic forcing is used, better coherence across cells in the population was observed in both *in-silico* and *in-vivo* experiments.

A pressing open problem is that such a balancing goal was only achieved for certain forcing inputs whose features (amplitudes, period, and duty-cycle) were carefully selected offline by trial-and-error. When different periods and amplitudes were tested *in-vivo*, often coherence and control were lost with many cells in the population falling towards one of the two stable equilibria rather than remaining balanced around the desired undifferentiated state [93]. Moreover, cell growth, cell-to-cell variability, uncertainties and noise can make any offline choice of the forcing inputs unable to fulfill the control goal in practice. Therefore, closed-loop action needs to be found able to compensate against these effects by adapting inputs' features in real-time to cope with changing environmental conditions, growth, diffusion and other unmodelled effects.

Differently from previous results in the literature, here we present strategies strongly oriented to assess the feasibility of a possible *in-vivo* implementation, taking into account for their validation realistic constraints on the inputs and other phenomena such as cell growth and spatial diffusion of the inducers. Therefore, we focus on designing feedback control strategies to stabilize the toggle switch in a region where none of the two proteins are fully expressed by forcing the system with two mutually exclusive periodic inputs.

In the rest of this Chapter we will introduce a nonlinear, nonsmooth 6^{th} order model that captures the dynamics of the GTS. We will show that the dynamics of this model, when subject to mutually exclusive square wave inputs applied in open-loop, can be approximated on average by a 2^{nd} order vector field that captures the mean value at steady state of the oscillations exhibited by the original system. Then, we will exploit this *average model* to design two control strategies able to balance the GTS in a region surrounding its unstable equilibria. The performance of the proposed controllers will be assessed in first place via MATLAB simulations, and later with more realistic agent based simulations. A quantitative comparison of the presented strategies concludes the Chapter.

3.2 Mathematical Model of the Genetic Toggle Switch

The model of the synthetic toggle switch we considered in our analysis was originally developed in Lugagne *et al.* [93]; the biological implementation of the system were already shown in Figure 2.1. The model captures the pseudo-reactions describing transcription

$$\begin{aligned} \emptyset &\xrightarrow{f_{\text{L}}^{\text{m}}(TetR,aTc)} mRNA_{\text{LacI}}, \\ \emptyset &\xrightarrow{f_{\text{T}}^{\text{m}}(LacI,IPTG)} mRNA_{\text{TetR}}, \end{aligned}$$

those describing translation

$$\begin{aligned} mRNA_{\text{LacI}} &\xrightarrow{\kappa_{\text{L}}^{\text{p}}} mRNA_{\text{LacI}} + LacI, \\ mRNA_{\text{TetR}} &\xrightarrow{\kappa_{\text{T}}^{\text{p}}} mRNA_{\text{TetR}} + TetR, \end{aligned}$$

and those related to dilution/degradation

$$\begin{aligned} mRNA_{\text{LacI}} &\xrightarrow{g_{\text{L}}^{\text{m}}} \emptyset, \quad mRNA_{\text{TetR}} \xrightarrow{g_{\text{T}}^{\text{m}}} \emptyset, \\ LacI &\xrightarrow{g_{\text{L}}^{\text{p}}} \emptyset, \quad TetR \xrightarrow{g_{\text{T}}^{\text{p}}} \emptyset. \end{aligned}$$

In the above equations, $f_{\text{L}}(TetR, aTc)$ and $f_{\text{T}}(LacI, IPTG)$ are the gene regulation functions defined as:

$$\begin{aligned} f_{\text{L}}(TetR, aTc) &:= \kappa_{\text{L}}^{\text{m0}} + \kappa_{\text{L}}^{\text{m}} \cdot h^{-}(TetR \cdot h^{-}(aTc, \theta_{\text{aTc}}, \eta_{\text{aTc}}), \theta_{\text{TetR}}, \eta_{\text{TetR}}), \\ f_{\text{T}}(LacI, IPTG) &:= \kappa_{\text{T}}^{\text{m0}} + \kappa_{\text{T}}^{\text{m}} \cdot h^{-}(LacI \cdot h^{-}(IPTG, \theta_{\text{IPTG}}, \eta_{\text{IPTG}}), \theta_{\text{LacI}}, \eta_{\text{LacI}}), \end{aligned}$$

the parameters $\kappa_{\text{L/T}}^{\text{m0}}$, $\kappa_{\text{L/T}}^{\text{m}}$, $\kappa_{\text{L/T}}^{\text{p}}$, $g_{\text{L/T}}^{\text{m}}$, $g_{\text{L/T}}^{\text{p}}$ are basal transcription, transcription, translation, mRNA degradation, and protein degradation rates, respectively, and $h^{-}(x, \theta, \eta) = 1/(1 + (x/\theta)^{\eta})$ represents a decreasing Hill function.

The pseudo-reactions listed above can be put together to obtain the following *deterministic model* of the toggle switch dynamics:

$$\frac{d\,mRNA_{\mathrm{LacI}}}{dt} = \kappa_{\mathrm{L}}^{\mathrm{m0}} + \frac{\kappa_{\mathrm{L}}^{\mathrm{m}}}{1+\left(\frac{TetR}{\theta_{\mathrm{TetR}}}\cdot\frac{1}{1+(aTc/\theta_{\mathrm{aTc}})^{\eta_{\mathrm{aTc}}}}\right)^{\eta_{\mathrm{TetR}}}} - g_{\mathrm{L}}^{\mathrm{m}}\cdot mRNA_{\mathrm{LacI}} \tag{3.1}$$

$$\frac{d\,mRNA_{\mathrm{TetR}}}{dt} = \kappa_{\mathrm{T}}^{\mathrm{m0}} + \frac{\kappa_{\mathrm{T}}^{\mathrm{m}}}{1+\left(\frac{LacI}{\theta_{\mathrm{LacI}}}\cdot\frac{1}{1+(IPTG/\theta_{\mathrm{IPTG}})^{\eta_{\mathrm{IPTG}}}}\right)^{\eta_{\mathrm{LacI}}}} - g_{\mathrm{T}}^{\mathrm{m}}\cdot mRNA_{\mathrm{TetR}} \tag{3.2}$$

$$\frac{d\,LacI}{dt} = \kappa_{\mathrm{L}}^{\mathrm{p}}\cdot mRNA_{\mathrm{LacI}} - g_{\mathrm{L}}^{\mathrm{p}}\cdot LacI \tag{3.3}$$

$$\frac{d\,TetR}{dt} = \kappa_{\mathrm{T}}^{\mathrm{p}}\cdot mRNA_{\mathrm{TetR}} - g_{\mathrm{T}}^{\mathrm{p}}\cdot TetR \tag{3.4}$$

The model is completed by considering the diffusion dynamics of the inducer molecules, aTc and IPTG, across the cells' membranes with the non-symmetrical exchange dynamics as in [93] given by:

$$\frac{d\,aTc}{dt} = \begin{cases} k_{\mathrm{aTc}}^{\mathrm{in}}(u_{\mathrm{aTc}} - aTc), & \text{if } u_{\mathrm{aTc}} > aTc \\ k_{\mathrm{aTc}}^{\mathrm{out}}(u_{\mathrm{aTc}} - aTc), & \text{if } u_{\mathrm{aTc}} \le aTc \end{cases}, \tag{3.5}$$

$$\frac{d\,IPTG}{dt} = \begin{cases} k_{\mathrm{IPTG}}^{\mathrm{in}}(u_{\mathrm{IPTG}} - IPTG), & \text{if } u_{\mathrm{IPTG}} > IPTG \\ k_{\mathrm{IPTG}}^{\mathrm{out}}(u_{\mathrm{IPTG}} - IPTG), & \text{if } u_{\mathrm{IPTG}} \le IPTG \end{cases}, \tag{3.6}$$

where aTc and $IPTG$ denote the concentrations of the inducer molecules inside the cell, while u_{aTc} and u_{IPTG} those in the growth medium of the cells.

The values of all model parameters from [93] are listed in Table 3.1.

$\kappa_{\mathrm{L}}^{\mathrm{m0}}$	3.20e-2 mRNA min^{-1}	$g_{\mathrm{L}}^{\mathrm{m}}$, $g_{\mathrm{T}}^{\mathrm{m}}$	1.386e-1 min^{-1}
$\kappa_{\mathrm{T}}^{\mathrm{m0}}$	1.19e-1 mRNA min^{-1}	$g_{\mathrm{L}}^{\mathrm{p}}$, $g_{\mathrm{T}}^{\mathrm{p}}$	1.65e-2 min^{-1}
$\kappa_{\mathrm{L}}^{\mathrm{m}}$	8.30 mRNA min^{-1}	θ_{LacI}	31.94 a.u.
$\kappa_{\mathrm{T}}^{\mathrm{m}}$	2.06 mRNA min^{-1}	η_{LacI}	2.00
$\kappa_{\mathrm{L}}^{\mathrm{p}}$	9.726e-1 a.u. mRNA min^{-1}	θ_{TetR}	30.00 a.u.
$\kappa_{\mathrm{L}}^{\mathrm{p}}$	9.726e-1 a.u. mRNA min^{-1}	η_{TetR}	2.00
$k_{\mathrm{IPTG}}^{\mathrm{in}}$	2.75e-2 min^{-1}	θ_{IPTG}	9.06e-2 mM
$k_{\mathrm{IPTG}}^{\mathrm{out}}$	1.11e-1 min^{-1}	η_{IPTG}	2.00
$k_{\mathrm{aTc}}^{\mathrm{in}}$	1.62e-1 min^{-1}	θ_{aTc}	11.65 ng/ml
$k_{\mathrm{aTc}}^{\mathrm{out}}$	2.00e-2 min^{-1}	η_{aTc}	2.00

Table 3.1: Value of the parameters of the model Eqs. (1)-(6).

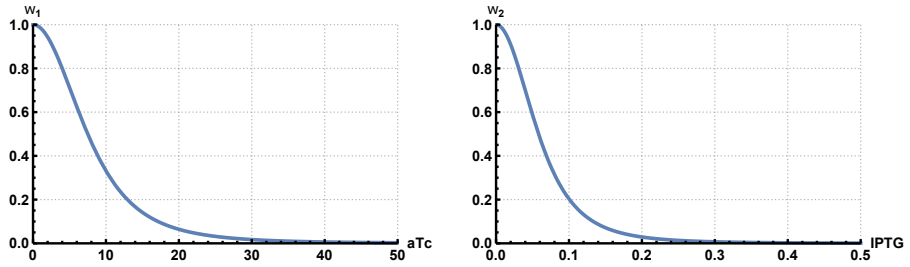

Figure 3.2: Static non-linear functions $w_1(aTc(t))$ and $w_2(IPTG(t))$ as expressed in the equations (3.9) and (3.10).

Quasi Steady-State Model

By assuming (i) instantaneous diffusion of the inducers across the cell membrane, (ii) equal degradation rates for LacI and TetR (that is, $g_{\mathrm{L}}^{\mathrm{p}} = g_{\mathrm{T}}^{\mathrm{p}} = g^{\mathrm{p}}$), and (iii) exploiting the fact that the time scales of the mRNA dynamics are notably faster than those of the proteins [44], we can obtain the following *non-dimensional quasi-steady state model* of the toggle switch:

$$\begin{aligned} \frac{dx_1}{dt'} &= k_1^0 + \frac{k_1}{1 + x_2^2 \cdot w_1(t'/g^{\mathrm{p}})} - x_1 \\ \frac{dx_2}{dt'} &= k_2^0 + \frac{k_2}{1 + x_1^2 \cdot w_2(t'/g^{\mathrm{p}})} - x_2 \end{aligned} \tag{3.7}$$

where

$$t' = g^{\mathrm{p}}\, t, \quad x_1 = \frac{LacI}{\theta_{\mathrm{LacI}}}, \quad x_2 = \frac{TetR}{\theta_{\mathrm{TetR}}}, \tag{3.8}$$

are *rescaled* time and states, and the dimensionless parameters are defined as

$$k_1^0 = \frac{\kappa_{\mathrm{L}}^{\mathrm{m0}}\, \kappa_{\mathrm{L}}^{\mathrm{p}}}{g_{\mathrm{L}}^{\mathrm{m}}\, \theta_{\mathrm{LacI}}\, g^{\mathrm{p}}}, \quad k_1 = \frac{\kappa_{\mathrm{L}}^{\mathrm{m}}\, \kappa_{\mathrm{L}}^{\mathrm{p}}}{g_{\mathrm{L}}^{\mathrm{m}}\, \theta_{\mathrm{LacI}}\, g^{\mathrm{p}}},$$

$$k_2^0 = \frac{\kappa_{\mathrm{T}}^{\mathrm{m0}}\, \kappa_{\mathrm{T}}^{\mathrm{p}}}{g_{\mathrm{T}}^{\mathrm{m}}\, \theta_{\mathrm{TetR}}\, g^{\mathrm{p}}}, \quad k_2 = \frac{\kappa_{\mathrm{T}}^{\mathrm{m}}\, \kappa_{\mathrm{T}}^{\mathrm{p}}}{g_{\mathrm{T}}^{\mathrm{m}}\, \theta_{\mathrm{TetR}}\, g^{\mathrm{p}}}.$$

The nonlinear functions $w_1(t)$ and $w_2(t)$ take into account the static relationship between each repressor protein (TetR or LacI) and its corresponding regulator molecule (aTc or IPTG, respectively). They are defined as

$$w_1(aTc(t)) := \frac{1}{\left(1 + \left(\frac{aTc(t)}{\theta_{\mathrm{aTC}}}\right)^{\eta_{\mathrm{aTc}}}\right)^{\eta_{\mathrm{TetR}}}} \tag{3.9}$$

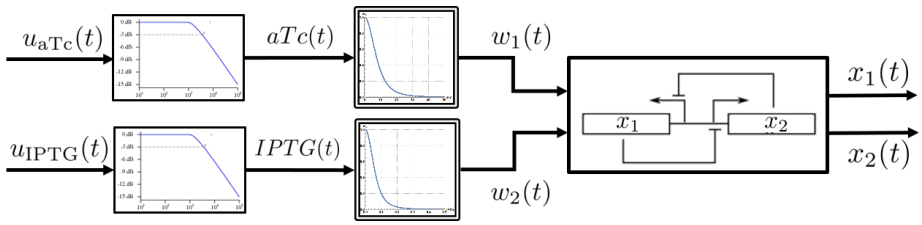

Figure 3.3: Block diagram of the system (3.7) with diffusion dynamics across cell membrane (3.5)-(3.6).

$$w_2(IPTG(t)) := \frac{1}{\left(1+\left(\frac{IPTG(t)}{\theta_{\mathrm{IPTG}}}\right)^{\eta_{\mathrm{IPTG}}}\right)^{\eta_{\mathrm{LacI}}}} \tag{3.10}$$

and they are shown in Figure 3.2.

System (3.7) with the static relations (3.9)-(3.10) and diffusion dynamics across the cell membrane (3.5)-(3.6) can be represented in block form as in Figure 3.3. The cell membrane acts as a linear non-symmetrical first order low-pass filter for the signals $u_{\mathrm{aTc}}(t)$ and $u_{\mathrm{IPTG}}(t)$ with a cut-off frequency that depends on the diffusion exchange rates $k_{\mathrm{aTc}}^{\mathrm{in/out}}$ and $k_{\mathrm{IPTG}}^{\mathrm{in/out}}$. Therefore, $aTc(t)$ and $IPTG(t)$ are filtered versions of their respective input signals whose attenuation depends both on the cut-off frequency and on their spectral density.

3.3 Open Loop Analysis

Let us formulate the following assumption.

Assumption 1: The diffusion dynamics of the inducer molecules, aTc and IPTG, across the cell membrane is instantaneous. So

$$aTc(t) = u_{\mathrm{aTc}}(t) \tag{3.11}$$

$$IPTG(t) = u_{\mathrm{IPTG}}(t) \tag{3.12}$$

for every $t \geq t_0$.

Average Model

System (3.7) can be averaged when fed with two *mutually exclusive pulsatile inputs* of the form

$$\begin{aligned} u_{\mathrm{aTc}}(t) &= \bar{u}_{\mathrm{aTc}} \cdot (1 - s_q(t/T)) \\ u_{\mathrm{IPTG}}(t) &= \bar{u}_{\mathrm{IPTG}} \cdot s_q(t/T) \end{aligned} \tag{3.13}$$

where $s_q(t/T)$ is a periodic square wave of period T with duty-cycle $d \in [0,1]$. Note that $d = 0$ corresponds to "high aTc / no IPTG" in the growth medium;

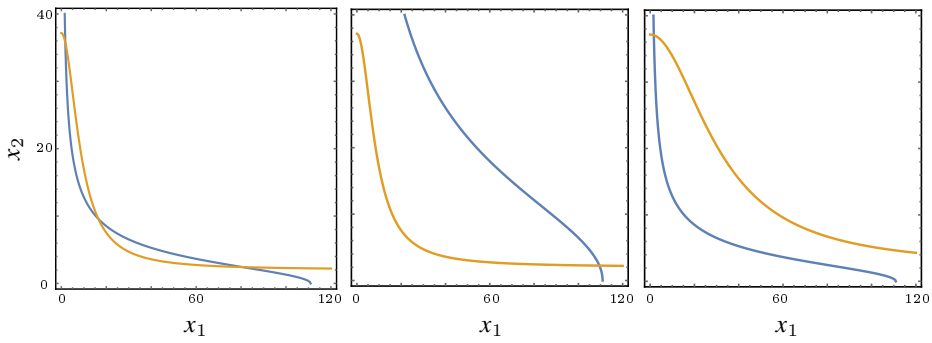

Figure 3.4: Nullclines of the system (3.7). Left panel: Bistability. Two stable and one unstable equilibrium points. Reference values $aTc = 20$ ng/ml, $IPTG = 0.25$mM. Central panel: Monostability. Unique high LacI / low TetR equilibrium point. Reference values $aTc = 50$ng/ml, $IPTG = 0.25$mM. Right panel: Monostability. Unique low LacI / high TetR equilibrium point. Reference values $aTc = 20$ng/ml, $IPTG = 0.50$mM.

this situation turns into the full steady-state expression of LacI (high x_1). Analogously, $d = 1$ corresponds to "no aTc / high IPTG" that yields to the full expression of the TetR (high x_2). So, the duty-cycle d can be used to regulate the ratio between the activation time of two monostable systems associated to the presence or absence of the two inducer molecules whose nullclines are shown in Figure 3.4.

Under Assumption 1 it follows that

$$\begin{aligned} w_1(t) &= w_1(aTc(t)) \\ &= w_1(\bar{u}_{\mathrm{aTc}} \cdot (1 - s_q(t/T))) \\ &= \bar{w}_1 + (1 - \bar{w}_1) \cdot s_q(t/T), \\ w_2(t) &= w_2(IPTG(t)) \\ &= w_2(\bar{u}_{\mathrm{IPTG}} \cdot s_q(t/T)) \\ &= \bar{w}_2 + (1 - \bar{w}_2) \cdot (1 - s_q(t/T)), \end{aligned} \tag{3.14}$$

where $\bar{w}_1 = w_1(\bar{u}_{\mathrm{aTc}})$ and $\bar{w}_2 = w_2(\bar{u}_{\mathrm{IPTG}})$.

By rescaling time setting $\tau = \frac{t'}{Tg^{\mathrm{p}}}$, system (3.7) can be recast as

$$\begin{aligned} \frac{dx_1}{d\tau} &= \varepsilon \left[k_1^0 + \frac{k_1}{1 + x_2^2 \cdot w_1(\tau T)} - x_1 \right] \\ \frac{dx_2}{d\tau} &= \varepsilon \left[k_2^0 + \frac{k_2}{1 + x_1^2 \cdot w_2(\tau T)} - x_2 \right] \end{aligned} \tag{3.15}$$

with $\varepsilon = Tg^{\mathrm{p}}$. The vector field in (3.15) is time-varying in τ with period 1.

The average vector field, say $f_{\text{av}}(x)$, can be obtained by integrating the vector field in (3.15) over a period and considering the forcing inputs (3.13), yielding

$$\begin{aligned} f_{\text{av},1}(x) &= \frac{1}{1}\int_0^1 \left(k_1^0 + \frac{k_1}{1+x_2^2\cdot w_1(\tau T)} - x_1\right) d\tau \\ &= k_1^0 + k_1\left(\int_0^d \frac{1}{1+x_2^2\cdot 1} d\tau + \int_d^1 \frac{1}{1+x_2^2\cdot \bar{w}_1} d\tau\right) - x_1 \\ &= k_1^0 + k_1\left(\frac{d}{1+x_2^2} + \frac{1-d}{1+x_2^2\cdot \bar{w}_1}\right) - x_1, \end{aligned}$$

and similarly,

$$\begin{aligned} f_{\text{av},2}(x) &= \frac{1}{1}\int_0^1 \left(k_2^0 + \frac{k_2}{1+x_1^2\cdot w_2(\tau T)} - x_2\right) d\tau \\ &= k_2^0 + k_2\left(\int_0^d \frac{1}{1+x_1^2\cdot \bar{w}_2} d\tau + \int_d^1 \frac{1}{1+x_1^2\cdot 1} d\tau\right) - x_2 \\ &= k_2^0 + k_2\left(\frac{d}{1+x_1^2\cdot \bar{w}_2} + \frac{1-d}{1+x_1^2}\right) - x_2. \end{aligned}$$

Therefore, the resulting *average system* is:

$$\begin{aligned} \frac{dx_1}{d\tau} &= \varepsilon\left[k_1^0 + k_1\left(\frac{d}{1+x_2^2} + \frac{1-d}{1+x_2^2\cdot w_1(\bar{u}_{\text{aTc}})}\right) - x_1\right] \\ \frac{dx_2}{d\tau} &= \varepsilon\left[k_2^0 + k_2\left(\frac{d}{1+x_1^2\cdot w_2(\bar{u}_{\text{IPTG}})} + \frac{1-d}{1+x_1^2}\right) - x_2\right] \end{aligned} \tag{3.16}$$

Let $x(\tau,\varepsilon)$ and $x_{\text{av}}(\varepsilon\tau)$ denote the solutions to (3.7) and (3.16), respectively. Assume $\bar{x}_{\text{av}}$ is an exponentially stable equilibrium point of the average system (3.16). Let Ω be a compact subset of its basin of attraction, and assume $x_{\text{av}}(0) \in \Omega$, and $x(0,\varepsilon) - x_{\text{av}}(0) = O(\varepsilon)$. Then, from [75, Theorem 10.4], there exists a positive parameter $\varepsilon^* = T^* g^{\text{p}}$ such that for all $0 < \varepsilon < \varepsilon^*$

$$x(\tau,\varepsilon) - x_{\text{av}}(\varepsilon\tau) = O(\varepsilon) \tag{3.17}$$

for all $\tau > 0$. That is, solutions $x(\tau,\varepsilon)$ to system (3.7) can be approximated by solutions $x_{\text{av}}(\varepsilon\tau)$ to (3.16) with an error that is proportional to ε. As a consequence, if $\bar{x}_{\text{av}}$ is the unique equilibrium point of system (3.16), then for all $0 < \varepsilon < \varepsilon^*$ system (3.7) has a unique, exponentially stable, periodic solution $\bar{x}(\tau,\varepsilon)$ in a $O(\varepsilon)$-neighborhood of $\bar{x}_{\text{av}}$.

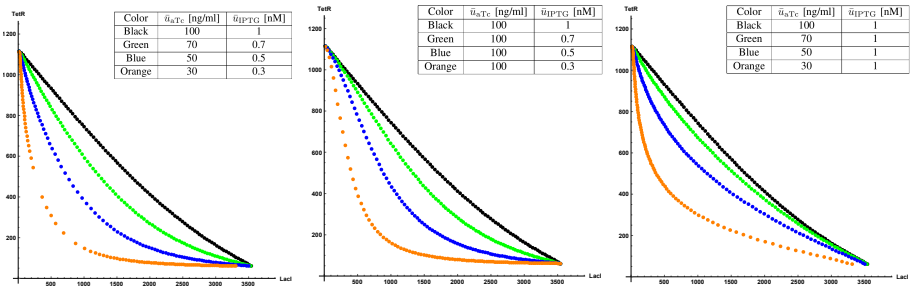

Figure 3.5: Equilibrium points $\bar{x}_{av}$ of (3.16) as a function of duty cycle d rescaled in arbitrary fluorescence units using (3.8). Each dot represents the location of the unique stable equilibrium point of system (3.16) evaluated for d taking values in the interval $[0; 1]$ with increments of 0.01. Left panel: equilibrium points for different values of $\bar{u}_{aTc}$ and $\bar{u}_{IPTG}$, as listed in the included table. Center panel: equilibrium points for $\bar{u}_{aTc} = 100$ng/ml and different values of $\bar{u}_{IPTG}$, as listed in the included table. Right panel: equilibrium points for $\bar{u}_{IPTG} = 1$mM and different values of $\bar{u}_{aTc}$, as listed in the included table.

Curves of equilibria of the average model

The number and position in state space of the equilibrium points $\bar{x}_{av} = [\bar{x}_1, \bar{x}_2]$ of the average vector field (3.16) depend on the specific choice of the amplitudes $\bar{u}_{aTc}$ and $\bar{u}_{IPTG}$ of the mutually exclusive pulsatile inputs, and on the value of the duty-cycle d. For example, for the reference values $\bar{u}_{aTc} = 50$ ng/ml and $\bar{u}_{IPTG} = 0.5$ mM, system (3.16) is monostable and the position of the equilibrium point $\bar{x}_{av}$ varies monotonically with d as reported in Figure 3.5 (left panel, blue dots). Hence, given certain values of $\bar{u}_{aTc}$ and $\bar{u}_{IPTG}$, it is possible to move the position of $\bar{x}_{av}$ on the corresponding curve $\Gamma_{\bar{u}_{aTc},\bar{u}_{IPTG}}$ by varying d, as reported in Figure 3.5 (center and right panels).

The phase portrait of the average system (3.16) together with a representative solution of the time-varying system (3.7) for d equal to 0.2 and 0.8 are depicted in Figure 3.6. The parameter ε has been set to 0.1 which corresponds to a forcing period $T = \varepsilon/g^p \approx 6$ min, and the system has been simulated for $t_f = \tau_f T \approx 50 \cdot 6 = 300$ min. It is possible to notice that, consistently with the curves of equilibria shown in Figure 3.5, the system (3.7) converges towards two different solutions; namely, it settles on a periodic solution "high x_1 / low x_2" for $d = 0.2$ and on a periodic solution "low x_1 / high x_2" for $d = 0.8$.

The phase portrait of the average system (3.16) together with a representative solution of the time-varying system (3.7) for d equal to 0.5 for different values of the parameter ε are reported in Figure 3.7. The parameter ε in the right panel has been set to 3 which corresponds to a forcing period $T = \varepsilon/g^p \approx 180$ min, and the system has been simulated for $t_f = \tau_f T \approx 50 \cdot 180 = 9000$ min.

Larger values of ε correspond to larger values of the forcing period T. In turn,

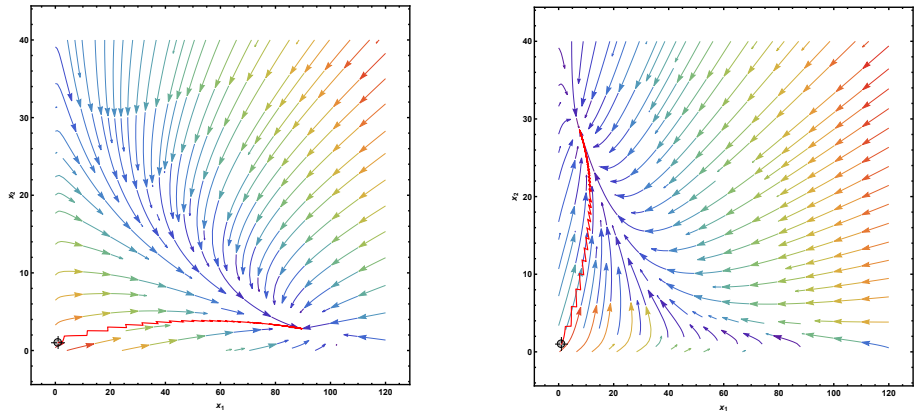

Figure 3.6: Background: phase portrait of the average system (3.16). Red line: the solution of the time-varying system (3.7) with $\bar{u}_{\mathrm{aTc}} = 50\,\mathrm{ng/ml}$ and $\bar{u}_{\mathrm{IPTG}} = 0.5\,\mathrm{mM}$ from initial condition $[1,1]^{\mathsf{T}}$. Left panel: $d = 0.2$, $T \approx 6\,\mathrm{min}$ ($\varepsilon = 0.1$). Right panel: $d = 0.8$, $T \approx 6\,\mathrm{min}$ ($\varepsilon = 0.1$).

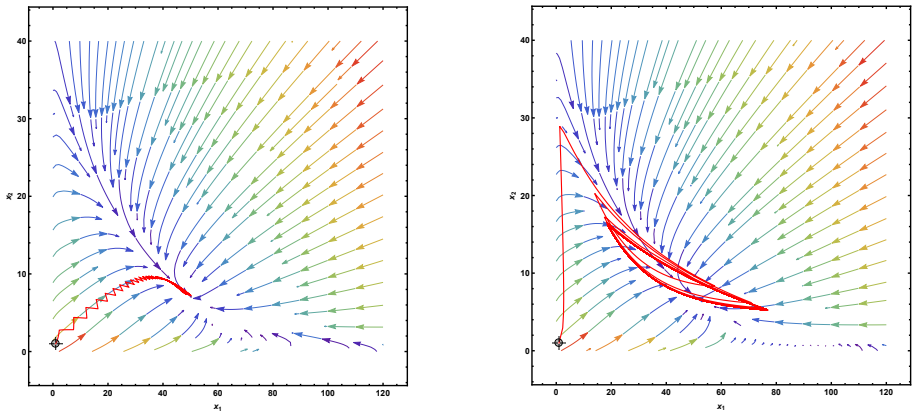

Figure 3.7: Background: phase portrait of the average system (3.16). Red line: the solution of the time-varying system (3.7) with $\bar{u}_{\mathrm{aTc}} = 50\,\mathrm{ng/ml}$ and $\bar{u}_{\mathrm{IPTG}} = 0.5\,\mathrm{mM}$ from initial condition $[1,1]^{\mathsf{T}}$. Left panel: $d = 0.5$, $T \approx 6\,\mathrm{min}$ ($\varepsilon = 0.1$). Right panel: $d = 0.5$, $T \approx 180\,\mathrm{min}$ ($\varepsilon = 3$).

from (3.17), this also implies that the solution $x(\tau, \varepsilon)$ of (3.7) will asymptotically converge to a periodic solution $\bar{x}(\tau, \varepsilon)$ contained in a larger set (Figure 3.7, right panel), and hence to a worse approximation.

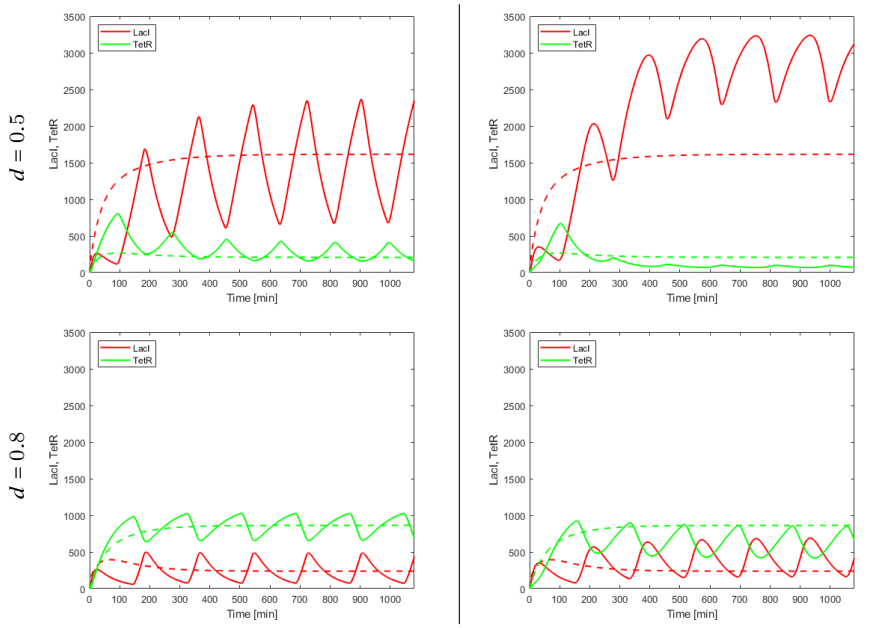

Figure 3.8: Effects of the membrane diffusion dynamics. Time evolution of the system (3.7) (in solid lines) and of the average system (3.16) (dashed lines) from initial conditions $[1,1]^\top$ with $\bar{u}_{\mathrm{aTc}} = 50$ ng/ml, $\bar{u}_{\mathrm{IPTG}} = 0.5$ mM, $T = 180$ min. Top panels: $d = 0.5$. Bottom panels: $d = 0.8$.

Diffusion effects

Dropping the Assumption 1, it is possible to take into account the low-pass filtering properties of the cell membrane. Therefore, $aTc(t)$ and $IPTG(t)$ will not any-more be ideal pulse waves but the filtered versions of $u_{\mathrm{aTc}}(t)$ and $u_{\mathrm{IPTG}}(t)$ through the membrane, as shown in Figure 3.3. In order for the average system (3.16) to continue being a good approximation of the actual cell response, the cut-off frequency of the two low-pass filters should be sufficiently higher that the fundamental frequency $1/T$ of the input waves.

However, due to the inevitable attenuation of high-frequency harmonics, there will always be a mismatch between the actual mean response of the cell and the value predicted by (3.16). The effects of the relaxation of the Assumption 1 can be observed in Figure 3.8.

The mean steady-state response of the complete system (3.1)-(3.4) with diffusion dynamics (3.5)-(3.6) and the corresponding equilibrium point $\bar{x}_{\mathrm{av}}(d)$ predicted by the autonomous two-dimensional system (3.16) are compared, for representative values of the PWM amplitudes and different values of d, in Figure

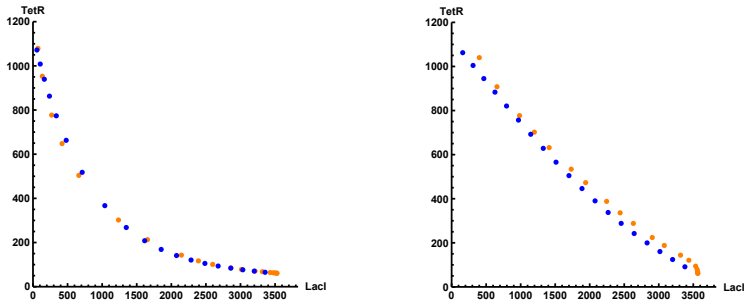

Figure 3.9: Effects of the membrane diffusion dynamics. Orange dots: mean-value, evaluated at regime, of the response of the system (3.1)-(3.4) with diffusion dynamics (3.5)-(3.6) to PWM inputs with $T = 240$ min and varying d from 0.05 to 0.95 with increments of 0.05. Blue dots: corresponding equilibrium point $\bar{x}_{\text{av}}(d)$ of system (3.16) rescaled in a.u. using (3.8). Left panel: Amplitude of pulse waves set to $\bar{u}_{\text{aTc}} = 50$ ng/ml and $\bar{u}_{\text{IPTG}} = 0.5$ mM. Right panel: Amplitude of pulse waves set to $\bar{u}_{\text{aTc}} = 100$ ng/ml and $\bar{u}_{\text{IPTG}} = 1$ mM.

3.9. Although, as expected, there is no perfect matching between the two, the observed behaviour is well captured by the average system. However, in regulation problems, this mismatch can be compensated by designing an adequate feedback action, as we will see in the next section.

When, on the other hand, the cut-off frequency of one of the filters is lower than the frequency $1/T$ of the input pulse waves, the input signal will be highly attenuated, resulting in the simple regulation of the toggle switch to either one of the stable equilibrium points, as noted in [93]. Similar phenomenon occurs when the duty cycle of the PWM inputs is close to 0 or 1.

In the rest of this Chapter, we will focus about the design of external control strategies to regulate the PWM inputs balancing the system (3.1)-(3.4) (with the diffusion dynamics (3.5)-(3.6)) in a region where none of the two exclusive proteins is fully expressed.

3.4 Proposed External Control Strategies

In this section we present a schematic that will be used to select the characteristics – amplitudes $\bar{u}_{\text{aTc}}$ and $\bar{u}_{\text{IPTG}}$ and duty-cycle d – of the mutually exclusive forcing input, with the aim of balancing a population of toggle switches in a given region of its phase space. The controller is based on the schematic proposed in Figure 3.10 and it is essentially composed by two control actions:

1. A *feed-forward* action, or Model Based Inversion algorithm, that pre-computes the value of the inputs amplitudes $\bar{u}_{\text{aTc}}$ and $\bar{u}_{\text{IPTG}}$ and duty-cycle d_{ref} required to achieve the control goal in the absence of perturbations and diffu-

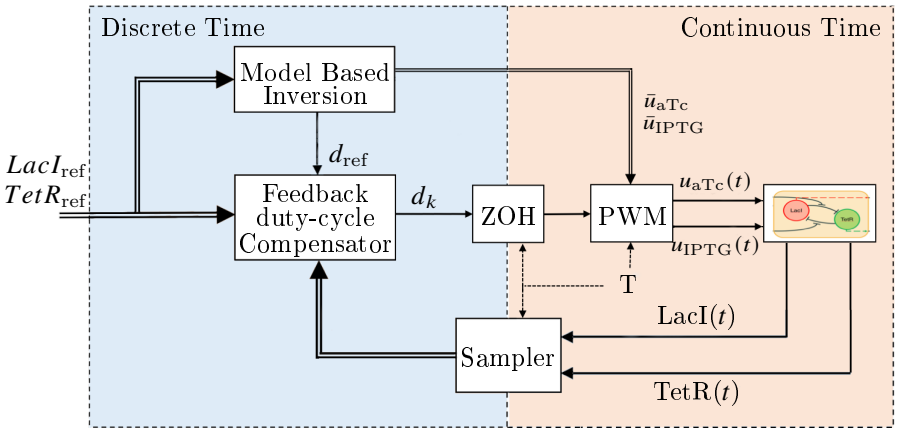

Figure 3.10: Block diagram of the proposed closed-loop hybrid control strategies. The population of cells, together with the PWM inputs, evolve in continuous-time. The controller is instead designed in discrete-time, computing the control input at each time period T. A feed-forward *Model Based Inversion* block evaluates the amplitudes $\bar{u}_{\mathrm{aTc}}$ and $\bar{u}_{\mathrm{IPTG}}$ of the pulse wave inputs, on the basis of the setpoint $[LacI_{\mathrm{ref}}, TetR_{\mathrm{ref}}]$. A *Feedback duty-cycle compensator* (implemented via either the PIPWM or the MPC strategies) evaluates and adapts in real time the duty-cycle of the inputs as a function of the desired setpoints and the (sampled) outputs of the system. The *Zero-Order Holder* (ZOH) keeps the duty-cycle, computed by the compensator at the beginning of each period, constant during the rest of the period T. The *Sampler* elaborates the continuous-time outputs of the system to provide the controller with the discrete time information it requires.

sion effects. This component operates by inverting the simplified, average non-linear model of the toggle switch (3.16).

2. A *feedback* action that adapts the duty-cycle d_k of the periodic inputs as a dynamic function of the current cell behaviour, measured via the fluorescence microscope. Specifically, this component has been implemented in two different strategies:
   - a proportional-integral (PIPWM) controller that drives a pulse width modulation block;
   - a Model Predictive Controller (MPC) that selects the input duty-cycle dynamically by optimizing a desired cost function.

By the mean of the model (3.16) we built a database of 60 curves of equilibria $\Gamma_{\bar{u}_{\mathrm{aTc}},\bar{u}_{\mathrm{IPTG}}}$. Each curve is associated to a couple of values $(\bar{u}_{\mathrm{aTc}}, \bar{u}_{\mathrm{IPTG}})$ and shows the position of $\bar{x}_{\mathrm{av}}(\bar{u}_{\mathrm{aTc}}, \bar{u}_{\mathrm{IPTG}}, d)$ varying d in the range $[0.05, 0.95]$ with a step of 0.05. In this sense, the *feed-forward* action, by choosing the amplitudes $\bar{u}_{\mathrm{aTc}}$ and $\bar{u}_{\mathrm{IPTG}}$, selects a curve of equilibria $\Gamma_{\bar{u}_{\mathrm{aTc}},\bar{u}_{\mathrm{IPTG}}}$ that, at steady-state, is the

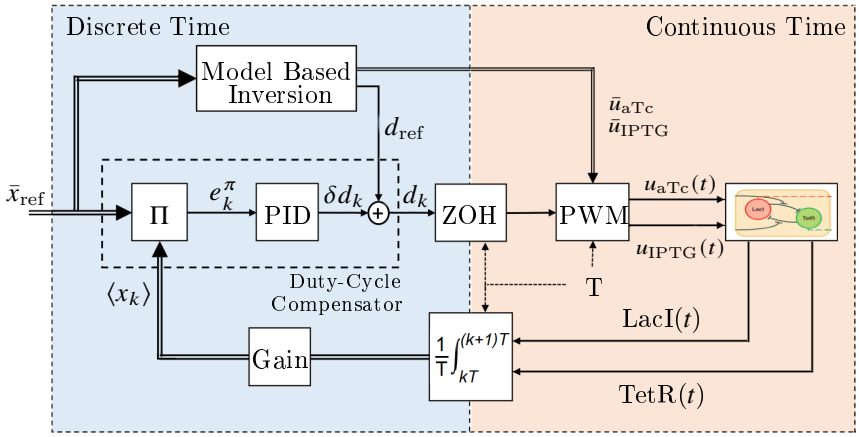

Figure 3.11: PIPWM control strategy. Given the setpoint for the average model $\bar{x}_{\text{ref}}$, two actions regulate the parameters of the PWM inputs that feed the system. The feedforward action is composed by the Model Based Inversion that evaluates the amplitudes $\bar{u}_{\text{aTc}}$ and $\bar{u}_{\text{IPTG}}$ and the nominal value of the duty-cycle d_{ref}. The nonlinear projector Π and a proportional-integral controller compose the feedback loop. At each time period $t_k = k\,T$, the nonlinear projector Π evaluates the projection error e_k^π that is minimized by a PI controller that evaluates the correction δd_k to be added to d_{ref}.

closest (in terms of Euclidean distance) to the mean state $\langle x \rangle$ of the system (3.7) over the period T.

Both the alternative implementations of the feedback component will be introduced in this Chapter. Their efficacy will be assessed via simulations and they will be compared by the mean of quantitative indexes.

3.4.1 Proportional-Integral Controller (PIPWM)

The basic idea behind the proportional integral PIPWM controller – depicted in Figure 3.11 – is that of evaluating, at every time instant $t_k = k\,T$, $k \in \mathbb{N}_{>0}$, the duty-cycle d_k by adding a correction δd_k to the reference value d_{ref} computed by the Model Based Inversion algorithm. This correction δd_k is necessary not only to compensate the effects of diffusion neglected in the average model (3.16) shown in Figure 3.8 but also to guarantee good performance and robustness properties of the control system towards noise and stochastic effects. The duty-cycle is evaluated online by the PI controller as

$$d_k = d_{\text{ref}} + \delta d_k,$$

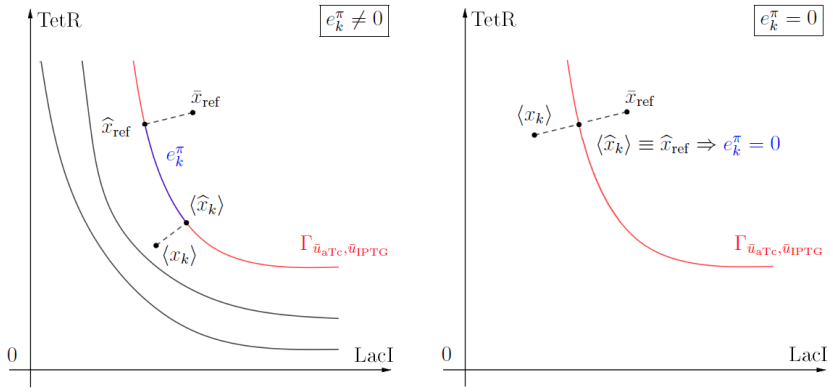

Figure 3.12: Working principle of the nonlinear projector block. Left panel: the red curve $\Gamma_{\bar{u}_{\text{aTc}},\bar{u}_{\text{IPTG}}}$ represents the closest one to the setpoint $\bar{x}_{\text{ref}}$ selected by the Model Based Inversion algorithm; black curves are other equilibrium curves that are farther from the setpoint. The setpoint $\bar{x}_{\text{ref}}$ and the mean value od the state in the k-th period $\langle x_k \rangle$ are projected onto the curve on the points $\widehat{x}_{\text{ref}}$ and $\langle \widehat{x} \rangle$, respectively. The length of the curve between $\hat{x}_{\text{ref}}$ and $\langle \widehat{x} \rangle$, highlighted in blue, is the *projection error* e_k^π at the time instant k. Right panel: even if the projected error e_k^π is zero, that is $||\langle \widehat{x} \rangle - \widehat{x}_{\text{ref}}|| = 0$, this does not necessarily imply zero regulation error, indeed in the case represented here $||\langle x \rangle - \bar{x}_{\text{ref}}|| \neq 0$.

$k \in \mathbb{N}_{>0}$, where δd_k is computed as:

$$\delta d_k = k_{\text{P}}\, e_k^\pi + k_{\text{I}} \sum_{j=0}^{k} e_j^\pi \tag{3.18}$$

with initial condition $d_0 = d_{\text{ref}}$, and where k_{P}, k_{I} are the gains of the PI controller and e_k^π is the *error* computed using a nonlinear projector Π.

The non-linear projector Π computes at the end of each k-th period T_k the error e_k^π as the length of the arc between $\widehat{x}_{\text{ref}}$ and $\langle \widehat{x} \rangle$ on a curve of equilibria $\Gamma_{\bar{u}_{\text{aTc}},\bar{u}_{\text{IPTG}}}$. The curve $\Gamma_{\bar{u}_{\text{aTc}},\bar{u}_{\text{IPTG}}}$ is (implicitly) selected by the Model Based Inversion algorithm by evaluating the amplitudes of the PWM inputs. The terms $\widehat{x}_{\text{ref}}$ and $\langle \widehat{x} \rangle$ are, respectively, the projections on $\Gamma_{\bar{u}_{\text{aTc}},\bar{u}_{\text{IPTG}}}$ of the setpoint $\bar{x}_{\text{ref}}$ and the mean value of the state in the k-th period $\langle x_k \rangle$, see Figure 3.12. The current measured mean value over a time period T computed as

$$\langle x_k \rangle = \frac{1}{T} \int_{kT}^{(k+1)T} x(\tau)\, d\tau.$$

Note that the projected error e_k^π being equal to 0 (i.e. $\|\langle \widehat{x}_k \rangle - \widehat{x}_{\text{ref}}\| = 0$) does not necessarily correspond to zero regulation error of the mean state value $\langle x_k \rangle$ onto $\bar{x}_{\text{ref}}$, that is $\|\langle x_k \rangle - \bar{x}_{\text{ref}}\| = 0$. Indeed, at steady-state the line connecting

these two points is orthogonal to the curve $\Gamma_{\bar{u}_{\mathrm{aTc}},\bar{u}_{\mathrm{IPTG}}}$ but its length may not be zero (see Figure 3.12, right panel). This residual error at steady-state can be made smaller by computing more curves $\Gamma_{\bar{u}_{\mathrm{aTc}},\bar{u}_{\mathrm{IPTG}}}$ in the database.

Because of the highly nonlinear and uncertain nature of the model, the tuning of the PI gains in the (3.18) was carried heuristically via extensive numerical simulations in MATLAB. Specifically, the closed loop system was simulated for 50 periods for 40'000 pairs of gain values k_{P} and k_{I} selected uniformly in the ranges $k_{\mathrm{P}} \in [10^{-4}, 1]$ and $k_{\mathrm{I}} \in [10^{-5}, 0.1]$; both intervals were divided in 200 uniformly distributed samples. Figure 3.13 shows the value of the settling time of the duty-cycle d_k and the norm of steady-state projected error e_π^∞ for each pair of gain values. The values of $k_{\mathrm{P}} = 0.0101$ and $k_{\mathrm{I}} = 0.0401$ were selected as those giving the best compromise between speed of the transient and residual steady-state error.

In-Silico experiments

Deterministic simulations were conducted in MATLAB using the model (3.1)-(3.4). The numerical integration of the model was carried out by implementing an event-driven algorithm. Each event is associated with the change of the inputs given to the system; therefore, an event is determined by the duty-cycle d_k and the period T of the PWM inputs which is set to 240 min. The solver `ode45` generates 100 non uniformly distributed time samples in each time period of the inputs T, leading to 1800 time samples in a total simulation time of 18 periods, corresponding to 72 hours. The results of the deterministic simulation of the PIPWM control strategy is reported in Figure 3.14.

Stochastic simulations were also performed in MATLAB using the Gillespie's Stochastic Simulation Algorithm. The solver is set at a fixed time step of 5 minutes. Using this setup, we obtain 48 time samples in each period T, leading to 864 samples in a total simulation time of 18 periods. Stochastic simulations of multiple cells were carried out in parallel, using the MATLAB Parallel toolbox to speed up the computation. The PIPWM controller closes a feedback control loop over a single target cell and evaluates the duty-cycle d_k of the PIPWM inputs. The inputs are fed to a population of 16 different switches. The results of the stochastic simulation of the PIPWM control strategy is reported in Figure 3.15.

The simulations showed in Figure 3.14 and in Figure 3.15 prove the effectiveness of the PIPWM control strategy. In the deterministic simulation of a single cell it is possible to notice that there is a residual steady-state error between the setpoint and the mean value of the state over the period T, especially on the *LacI*-RFP. This is due to the situation depicted in Figure 3.12 (right panel). In the stochastic case, the mean trajectory of the population of 16 cells over the period T is effectively kept away from the two stable equilibria, even if severe oscillations around the setpoint are present.

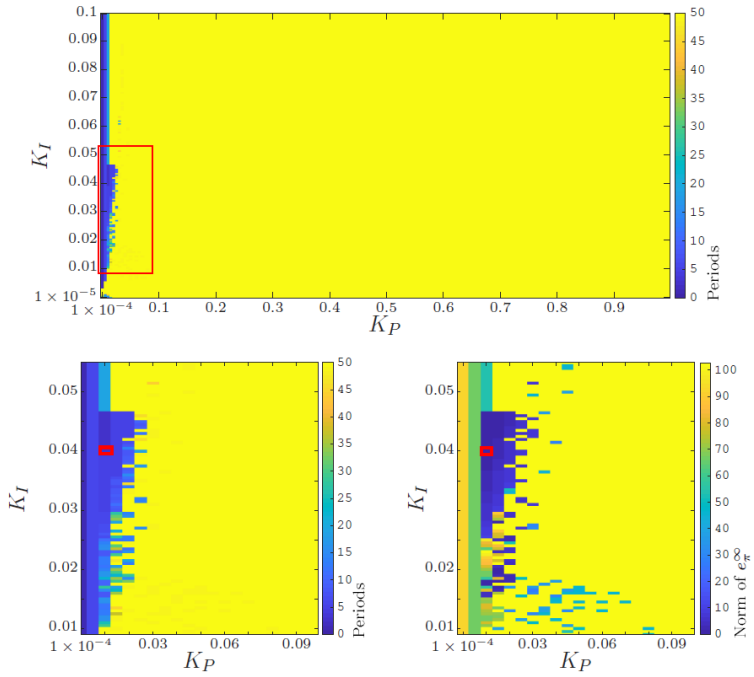

Figure 3.13: Tuning of the PI controller. Top panel: Settling time of the duty-cycle at the 10% of its final value, computed as a number of periods, for all pairs $(k_{\mathrm{P}}, k_{\mathrm{I}}) \in [10^{-4}, 1] \times [10^{-5}, 0.1]$. Note that the performance was evaluated over a simulation time of 50 periods and yellow coloured squares denote values of settling time ≥ 50 periods. Bottom left panel: Zoom of the most significant parameter region in top panel (highlighted within the red box); Bottom right panel: Norm of the steady-state projected error e_π^∞ for the same range of values of control gains as in bottom left panel. The red box in bottom panels indicates the values of PI gains that were selected and used for all *in-silico* control experiments.

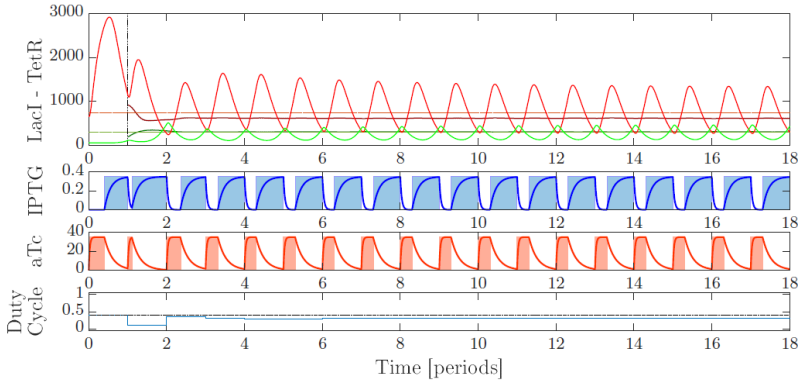

Figure 3.14: Deterministic *in-silico* experiments. Response of the toggle switch controlled by using the PIPWM strategy. PI gains were set to $k_P = 0.0101$ and $k_I = 0.0401$. Top panel: dashed red and green lines represent the setpoint of the experiment, respectively $LacI_{ref} = 750$ and $TetR_{ref} = 300$. Amplitudes of the inputs are $\bar{u}_{aTc} = 35$ ng/ml and $\bar{u}_{IPTG} = 0.35$ mM. Solid lines show the evolution of promoter proteins for *LacI* (red) and *TetR* (green). Dark solid lines, starting from $t = T$, are the mean values of the state in the time period, evaluated with a moving window of period T. Middle panels: shaded areas represent the evolution of the concentrations of the inducer molecules, $u_{IPTG}(t)$ and $u_{aTc}(t)$, applied outside of the cells' membranes by the controller, while solid lines represent the corresponding concentrations of the inducers, IPTG and aTc, inside the cells. Bottom panel: solid blue line represents the evolution of the duty-cycle over time and dot-dashed black line represents d_{ref}.

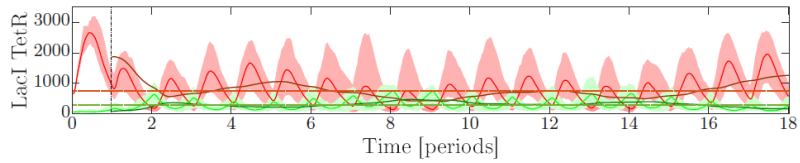

Figure 3.15: Stochastic *in-silico* experiments. Response of a population of 16 toggle switches controlled by using the PIPWM strategy. The setup is the same as the deterministic case. Dashed lines are the setpoint of the experiment, for $LacI_{ref}$ (red) and $TetR_{ref}$ (green). Solid red and green lines are the average evolution of *LacI* and *TetR* over the population. Darker solid lines represent the evolution of the mean trajectory in the period, evaluated with a moving window as in the deterministic case. Shaded areas represent the values of the standard deviation from the means, at each time instant.

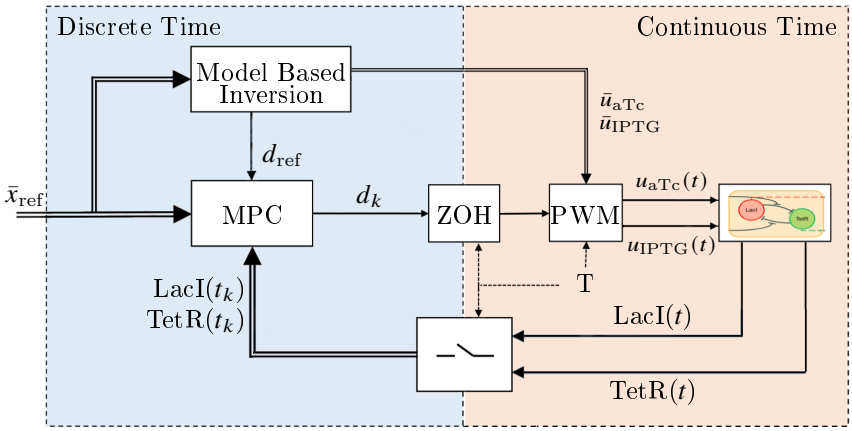

Figure 3.16: MPC control strategy. At each discrete time step k, the MPC finds the sequence of duty-cycles $\{d_0, d_1, \ldots, d_{N-1}\}$ that minimizes the cost function J_k over the prediction horizon $T_{\mathrm{p}} = NT$. Then, only the first element is selected ($d_k = d_0$) and the corresponding pulsatile control signals are applied to the biological system in the time interval $[t_k, t_k + T]$.

3.4.2 Model Predictive Control (MPC)

As alternative to the PIPWM control strategy, we propose a Model Predictive Controller, depicted in Figure 3.16. This kind of strategy have been widely applied in the field of synthetic biology [67], demonstrating their effectiveness also for *in-vivo* experiments [47]. Differently from the PIPWM controller, the MPC directly chooses, at each sampling time $t_k = kT$, the duty-cycle d_k to be applied in the next control cycle (of duration T). This is done by solving an online optimization problem on a finite prediction horizon interval of length $T_{\mathrm{p}} = NT$, with $N \in \mathbb{N}$.

Specifically, at each k-th iteration, the algorithm finds the sequence of duty-cycles $\{d_k, d_{k+1}, \ldots, d_{k+N-1}\}$ of length N that minimize the cost function J_k, defined as

$$J_k(\{d_0, d_1, \ldots, d_{N-1}\}) = \sum_{i=0}^{N-1} \int_{(k+i)T}^{(k+1+i)T} e(t, d_i)\, dt, \tag{3.19}$$

where $e(t, d)$ is the weighted relative squared error defined as

$$e(t, d_i) = K_{\mathrm{LacI}} \left(\frac{LacI(t,d_i) - LacI_{\mathrm{ref}}}{LacI_{\mathrm{ref}}} \right)^2 + K_{\mathrm{TetR}} \left(\frac{TetR(t,d_i) - TetR_{\mathrm{ref}}}{TetR_{\mathrm{ref}}} \right)^2,$$

in which $LacI(t, d_i)$ and $TetR(t, d_i)$ are the solution of the *deterministic* dynamical model (3.1)-(3.4) (complemented with diffusion dynamics across cell membrane (3.5)-(3.6)) when PWM pulsatile signals with duty-cycle d_i are applied

as inputs to the system. In order to make the control action robust to uncertainties and noise, only the first element d_0 of the sequence is used by the controller, so $d_k = d_0$. The remaining part of the sequence of duty-cycles, that is $\{d_1, d_2, \ldots, d_{N-1}\}$ is discarded.

The optimization problem is solved at each step by using the *genetic algorithms*[54] toolbox available in MATLAB, which also generates the sequences of duty-cycles $\{d_0, d_1, \ldots, d_{N-1}\}$, such that $d_i \in [0, 1]$.

After an extensive numerical search in MATLAB, the control parameters K_{LacI} and K_{TetR} in the cost function (3.19) were selected heuristically to $K_{\mathrm{LacI}} = 1$ and $K_{\mathrm{TetR}} = 4$, so as to minimize its final steady-state value. Specifically, the control evolution was simulated for 18 periods fixing $K_{\mathrm{LacI}} = 1$ and varying K_{TetR} over 37 values chosen uniformly in the interval $[0.01, 100]$, so as to vary the ratio between the two gains.

In-Silico experiments

As anticipated, *genetic algorithms* were used to numerically find the (sub)optimal control solution at each step. We adopted the MATLAB genetic algorithm toolbox by setting the initial population to 50 individuals randomly chosen in the interval $[0, d_{\mathrm{ref}}]$. The maximum number of generations was set to 150, while the maximum number of stall generations was set to 30. All the other parameters were kept to their default values, setting $T_p = 720$ minutes, that is, $N = 3$. Parallelization of the genetic algorithm optimization routine guarantee a significant reduction of the time required to compute the solution.

As in the case of the PIPWM controller, we carried out both deterministic and stochastic simulations, using the same algorithmic setup. Details about the simulation routines can be found in the previous Section.

The simulations showed in Figure 3.17 and in Figure 3.18 prove the effectiveness of the MPC control strategy. In the deterministic simulation of a single cell it is possible to notice that there is a residual steady-state error is lower (and almost negligible), compared to the previous case of the PIPWM strategy shown in Figure 3.14. In the stochastic case, the mean trajectory of the population of 16 cells over the period T is effectively regulated on the setpoint values, qualitatively showing better performances compared to the previous strategy.

3.5 Validation of the Control Strategies in BSim

Even though the stochastic simulations performed in MATLAB using the Gillespie algorithm are a good test-bench to test the behaviour of the control strategy in presence of uncertainties, there is the need to take into account several phenomena that are neglected in those kind of simulations. With a view towards the *in vivo* implementation of these controllers, it is important to test the strategies in a multi-physics scenario. To this aim, we conducted *in silico* experiments using

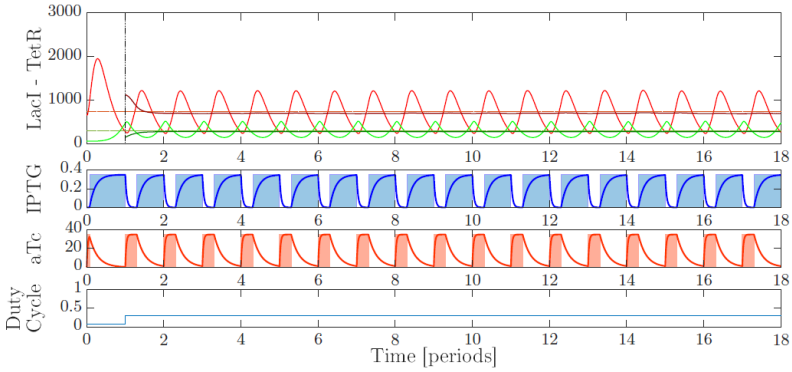

Figure 3.17: Deterministic *in-silico* experiments. Response of the toggle switch controlled by using the MPC strategy. Cost function weights were set to $K_{\mathrm{LacI}} = 1$ and $K_{\mathrm{TetR}} = 4$. Top panel: dashed red and green lines represent the setpoint of the experiment, respectively $LacI_{\mathrm{ref}} = 750$ and $TetR_{\mathrm{ref}} = 300$. Amplitudes of the inputs are $\bar{u}_{\mathrm{aTc}} = 35$ ng/ml and $\bar{u}_{\mathrm{IPTG}} = 0.35$ mM. Solid lines show the evolution of promoter proteins for *LacI* (red) and *TetR* (green). Dark solid lines, starting from $t = T$, are the mean values of the state in the time period, evaluated with a moving window of period T. Middle panels: shaded areas represent the evolution of the concentrations of the inducer molecules, $u_{\mathrm{IPTG}}(t)$ and $u_{\mathrm{aTc}}(t)$, applied outside of the cells' membranes by the controller, while solid lines represent the corresponding concentrations of the inducers, IPTG and aTc, inside the cells. Bottom panel: solid blue line represents the evolution of the duty-cycle over time.

BSim 2.0, an advanced bacteria simulator developed in Java [55, 105]. This simulator takes into account the living dynamics of the cell, with their reproduction and their death. Moreover, it also allows for the study the spacial diffusion of the inducers in the hosting chamber.

Inspired by the so-called *mother machine* [141] in microfluidics, we designed a $1 \times 30 \times 1$ μm rectangular chamber that hosts a single layer cell population where cells are lined up. The chamber is open on the top (short side), from where the inducers diffuses and cells are flushed out due to their own growth and medium flow. The simulations start with a single *E. coli* cell located at the bottom of the chamber; as the cell grows and duplicates, it pushes outside of the chamber new cells exceeding the maximum capacity of about 10 cells.

The solver adopted in the simulations is based on the *Euler-Maruyama* [63] method and generates samples at a fixed time step of 5 minutes, leading to 48 samples per period and 864 samples in the total simulation time of 18 periods.

We tested in BSim the two strategies proposed in this Chapter, the results are shown in Figure 3.19. Videos of the experiments can be found in [57] - Supplementary Material. Qualitatively comparing the two strategies, it is possible

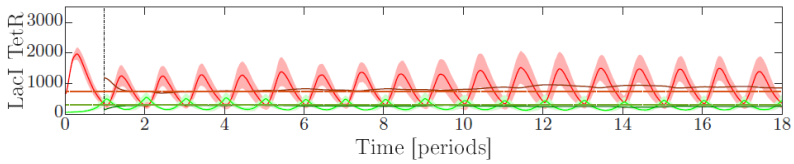

Figure 3.18: Stochastic *in-silico* experiments. Response of a population of 16 toggle switches controlled by using the MPC strategy. The setup is the same as the deterministic case. Dashed lines are the setpoint of the experiment, for $LacI_{\text{ref}}$ (red) and $TetR_{\text{ref}}$ (green). Solid red and green lines are the average evolution of $LacI$ and $TetR$ over the population. Darker solid lines represent the evolution of the mean trajectory in the period, evaluated with a moving window as in the deterministic case. Shaded areas represent the values of the standard deviation from the means, at each time instant.

to notice that both of them are capable of regulating the population of toggle switches on the given setpoint. However, as it possible to expect considering the additional knowledge on the dynamics of the system acquired by predicting its evolution, the dynamical performances of the MPC are better than the PIPWM both in terms of settling time and amplitude of the oscillations.

3.6 Quantitative Comparison of the Strategies

A quantitative analysis of the PIPWM and the MPC strategies is reported in Table 3.2. As a benchmark for comparison, the Open-Loop case, where PWM is driven with duty-cycle $d = d_{\text{ref}}$, is reported.

The strategies are compared according to three different performance indexes [47] based on the following definition of *error*:

$$\bar{e}(t) = \left\| \left[\frac{\overline{LacI}(t) - LacI_{\text{ref}}}{LacI_{\text{ref}}} ; \frac{\overline{TetR}(t) - TetR_{\text{ref}}}{TetR_{\text{ref}}} \right] \right\|_2, \tag{3.20}$$

where $\overline{LacI}(t)$ and $\overline{TetR}(t)$ are the moving averages of $LacI(t)$ and $TetR(t)$ respectively evaluated over a window of width T, that is

$$\overline{LacI}(t) = \frac{1}{T} \int_{t-T}^{t} LacI(\tau)\, d\tau,$$
$$\overline{TetR}(t) = \frac{1}{T} \int_{t-T}^{t} TetR(\tau)\, d\tau.$$

Specifically, we used the following control metrics:

1. *Integral Square Error* (ISE), defined as

$$ISE = \int_{t_0}^{t_f} \bar{e}(\tau)^2\, d\tau,$$

where $t_0 = T$ and t_f is the time instant at the end of the *in-silico* experiments. By integrating the square error over time, ISE penalizes large errors much more than smaller ones. Thus, this index can be used to compare performance during transients, in which the presence of the overshoot or a long settling time could give rise to significant errors. Small errors, even if persistent, do not significantly affect this metric.

2. *Integral Absolute Error* (IAE), defined as

$$IAE = \int_{t_0}^{t_f} |\bar{e}(\tau)| \, d\tau.$$

IAE integrates the absolute error, hence it penalizes small and large errors equally.

3. *Integral Time-weighted Absolute Error* (ITAE), defined as

$$ITAE = \int_{t_0}^{t_f} \tau|\bar{e}(\tau)| \, d\tau.$$

By integrating the absolute error multiplied by the time, ITAE tends to penalize more small persistent errors that occur at steady-state than large errors at the beginning of the experiment. For this reason, it is the best index to evaluate the performance of a controller for regulation tasks.

As further validation of the performance, in addition to the simulations previously shown – where parameters were kept to their nominal values reported in Table 3.1 – we carried out robustness tests introducing cell-to-cell variability in the parameters. Specifically, the parameters of each cell in the population were independently drawn from Gaussian distributions centred on their nominal values with a standard deviation of 5% and 10%, respectively.

Summing up the results, shown in Table 3.2, the MPC is, globally a better control strategy compared to the PIPWM. Interestingly, moving from the deterministic case to the stochastic case and introducing variations of the parameters, MPC performances worsen much more than PIPWM ones; this becomes very significant in the case of stochastic simulation with 5% parameter variations, where PIPWM shows better performances in all the three indexes. This situation is explainable considering that PIPWM does not require exact knowledge of the model and of its parameters, whereas MPC does.

The quantitative analysis of the agent based simulations in BSim does not significantly affect the overall performance of the two control strategies. Therefore, the MPC controller has to be considered the one that guarantees better regulation of a population of toggle switches, with the PIPWM being still way more effective than an Open-Loop forcing.

Deterministic simulations				
Strategy	Var.	ISE	IAE	ITAE
PIPWM	no	(876.71)	(1304.32)	(2.068673) E06
MPC	no	(47.58)	(382.04)	(0.811109) E06
Stochastic simulations				
Strategy	Var.	ISE	IAE	ITAE
Open-Loop	no	(13456.03)	(7413.06)	(16.822305) E06
PIPWM	no	469.90 (830.52)	998.20 (1472.87)	2.903351 (3.218139) E06
MPC	no	150.14 (178.50)	616.05 (724.72)	1.904908 (1.975185) E06
Stochastic simulations with parametric variations				
Strategy	Var.	ISE	IAE	ITAE
Open-Loop	5%	(15613.06)	(7985.07)	(18.091973 E06)
PIPWM	5%	687.30 (1605.77)	1224.34 (2056.69)	3.605903 (4.162760) E06
	10%	4369.72 (6061.33)	3094.09 (4317.68)	9.014108 (9.968271) E06
MPC	5%	1116.21 (1459.63)	1532.02 (2109.08)	4.193415 (4.716253) E06
	10%	2185.18 (2751.82)	2164.75 (2870.43)	6.153388 (6.791182) E06
Agent-based simulations with parametric variations				
Strategy	Var.	ISE	IAE	ITAE
Open-Loop	no	11161.13 (15543.92)	5661.29 (7923.19)	16.271114 (18.281741) E06
PIPWM	no	1483.72 (3671.39)	1510.72 (2939.98)	3.452511 (4.458611) E06
	10%	1781.40 (3508.97)	1826.95 (2975.92)	4.477333 (5.217549) E06
MPC	no	173.12 (277.18)	562.83 (836.80)	1.677061 (1.947358) E06
	10%	283.49 (481.36)	732.75 (1201.13)	2.097497 (2.451896) E06

Table 3.2: Quantitative assessment of the proposed control strategies. The performance metrics we considered are *Integral Square Error* (ISE), *Integral Absolute Error* (IAE) and *Integral Time-weighted Absolute Error* (ITAE) of the error signal $\bar{e}(t)$. The metrics were computed over both the last 12 periods (13 for the agent-based simulations) and the entire simulation time of 18 periods (reported in brackets). Cell-to-cell variability in the population was taken into account by independently drawing the parameters of each cell from Gaussian distributions centred on their nominal values with standard deviation of 5% and 10%; the values reported for these cases have been obtained by averaging three simulations each obtained using different sets of value of the parameters.

3.7 Discussion

In this Chapter we presented a model of the genetic toggle switch that describes its complete dynamics, including the non-symmetrical effects of the cell membrane. We conducted an open loop analysis of the time-average behaviour of the model when subject to mutually exclusive pulse wave inputs, deriving an average model that is capable of approximating its mean state. By exploiting this average model, we presented a set of feedback control strategies that can be used to change and adapt the duty-cycle of the inputs in real-time and select their amplitudes to achieve robust stabilization of the population even in the presence of noise and other unavoidable effects which render previous open-loop approaches unviable.

Stochastic and more realistic agent-based simulations proved the effectiveness of the two control strategies, suggesting that the MPC is to be preferred to the PIPWM for regulation performance. This is essentially due to the diametrically opposite ways in which the two algorithms evaluate the control inputs; the PIPWM by using approximations on the dynamics of the biological system and relatively light-weight numerical computations, the MPC by using complete knowledge of the model but extensive use of numerical optimization routines.

Specifically, the PIPWM relies on an ensemble of analytical approximations [44] hindering its performance. Firstly, the curves of equilibria $\Gamma_{\bar{u}_{\mathrm{aTc}},\bar{u}_{\mathrm{IPTG}}}$ of the average model used by the projector Π are computed by assuming quasi-steady state of the transcription dynamics of mRNAs and instantaneous diffusion of inducer molecules through the cell membrane. Secondly, the equilibrium point $\bar{x}_{\mathrm{av}}$ of the average model is an approximation of the mean value of the oscillations of LacI and TetR. This accuracy depends on the parameter $\varepsilon = T\,g^{\mathrm{p}}$ in the average model equations, where T is the period of the forcing inputs, and we fixed its value to 240 min that represented a good trade-off between the time scales of the toggle switch itself and diffusion effects of the cell membrane. Moreover, the desired setpoint $\bar{x}_{\mathrm{ref}} = [LacI_{\mathrm{ref}}/\theta_{\mathrm{LacI}}, TetR_{\mathrm{ref}}/\theta_{\mathrm{TetR}}]$, to which we want regulate the measured mean value $\langle x_k \rangle$ of the toggle switch response, does not exactly lie on the curve $\Gamma_{\bar{u}_{\mathrm{aTc}},\bar{u}_{\mathrm{IPTG}}}$ returned by the Model Based Inversion algorithm and employed to compute the error signal e_k^{π} for the PI (see Figure 3.12). Therefore, the curve represents an additional constraint to the performance of the control system.

In contrast, the MPC strategy does not require any approximation of the available deterministic model of the biological system under control and computes its control action to *directly* minimize the error between the desired setpoint and the measured mean value of the cell behaviour. The model is also used to predict the future evolution of the system and get better performance in the transient response (this property, typical of the derivative action of classical PID controllers, is missing in the PIPWM strategy).

However, the main limitation of the MPC with respect to the PIPWM is the higher computational cost required to solve the optimization problem at the

beginning of each control cycle requiring availability of an experimental platform with adequate computing power for its *in-vivo* implementation.

The strategies presented in this Chapter can be of practical relevance to "reset" other bistable, or multi-stable, cellular systems by balancing them in an unstable region corresponding to some undifferentiated state of interest. This is important, for example, in control experiments [120] where it has been proposed that mono-strain populations can be differentiated into multiple subpopulations by flipping the state of a synthetic toggle switch associated to different functions, or in stem cell applications where dedifferentiation [20, 111] aims precisely at "resetting" a differentiated cell.

From a theoretical viewpoint, we wish also to highlight that nonlinear average models for approximating the behaviour of biological systems under external pulsing stimuli could be useful for the design of feedback control strategies for future applications in synthetic biology.

We move next to the design and control of a turbidostat that was carried out independently from Chi.Bio [132] during the course of the PhD.

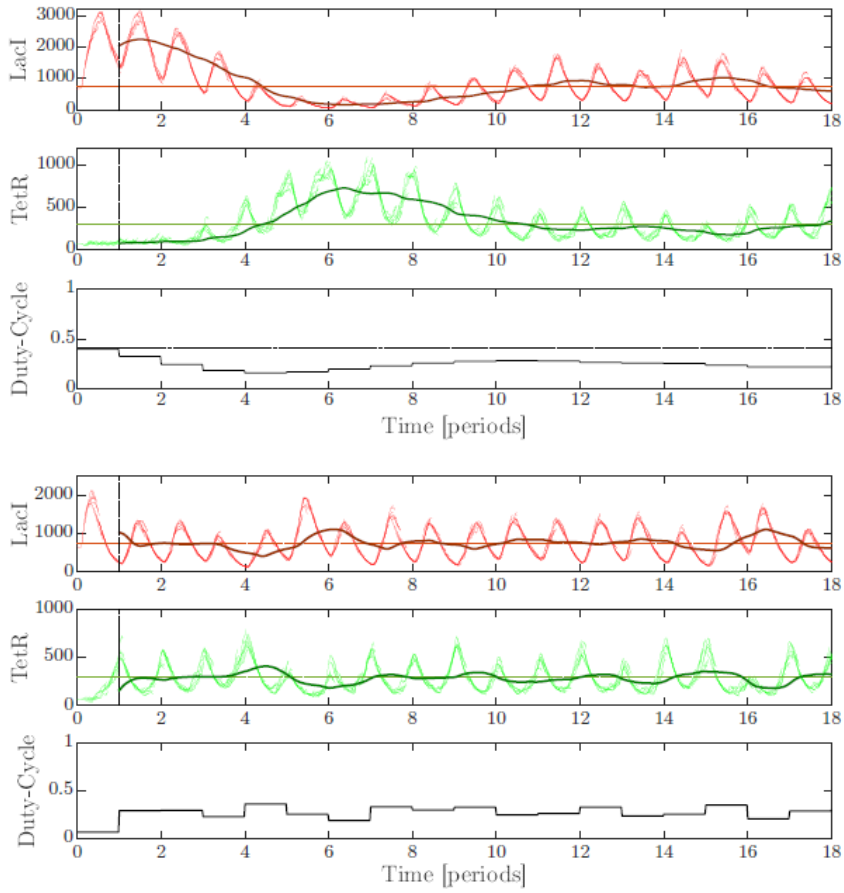

Figure 3.19: Agent-based simulation in BSim 2.0. The total simulation time is 72 hours with $T = 240$ min. The reference values provided by the Model Based Inversion algorithm and used in both simulations are $\bar{u}_{\mathrm{aTc}} = 35$, $\bar{u}_{\mathrm{IPTG}} = 0.35$, and $d_{\mathrm{ref}} = 0.4$. Top Figure: Response of the cells controlled by using the PIPWM strategy. PI gains were set to $k_{\mathrm{P}} = 0.0101$ and $k_{\mathrm{I}} = 0.0401$. Top panel: evolution over time of $LacI$; the dashed line representing the setpoint $LacI_{\mathrm{ref}} = 750$, while lighter lines the evolution of the state for each cell in the simulation, and the darker solid line the mean trajectory computed over the population, evaluated through a moving window of period T. Middle panel: evolution over time of $TetR$; the dashed line representing the setpoint $TetR_{\mathrm{ref}} = 300$, lighter lines are the evolution of the state for each cell in the simulation, while the dark solid line represents the evolution of the mean trajectory across the population in the period, evaluated using a moving window of period T. Bottom panel: evolution of the duty-cycle over time. Bottom Figure: Response of the cells controlled by using the MPC strategy. MPC cost function parameters were set to $K_{\mathrm{LacI}} = 1$, $K_{\mathrm{TetR}} = 4$, while the prediction horizon is $N = 3$.

4 Design and Control of a Turbidostat

4.1 Introduction

Biological advances over recent years have enabled the synthetic design and implementation of engineered bacterial populations to increase at a fast pace, see for example the control strategies designed in the previous Chapter. However, characterisation of the dynamic behaviour of these systems still proves difficult, creating a bottleneck for further advances [107]. The study and the characterization of synthetic bacterial systems have been conducted traditionally, due to ease of propagation and scalability, with batch culture techniques. However, it is now widely accepted that such techniques are no longer reliable. This is due to continually changing chemical environments caused by cell growth, nutrient depletion, waste production and cell death [106], which can lead to mischaracterisation of the output of synthetic systems in response to an input. Several continuous culture platforms have been commercially developed [119, 139, 91] in order to mitigate problems arising from batch culture. These systems add fresh media to the culture to dilute accumulated cells and waste products and they are generally operated as chemostats or turbidostats [31].

Chemostats maintain bacterial cultures at steady state by performing dilution of growth media containing fresh nutrients at a fixed rate. Turbidostats use a feedback control loop on the cell density of a culture, adding fresh growth media with the purpose of regulating the optical density (OD) of the culture [143]. Turbidostats are generally preferred to chemostats [96] when the cells need to be maintained at their maximum growth rate, as in experiments of characterisation of synthetic systems [131]. However, commercially available turbidostat systems are expensive, proprietary and often lack any flexibility in design. This lack of flexibility makes them difficult to adapt to changing experimental needs. As a result many research groups have begun to develop their own designs [65].

In this Chapter we present the design and implementation of a low-cost turbidostat, made up of modular components, which is inspired by the design of Takahashi and co-workers [134]. This modularity allows for customisable experi-

ment set up. Our design approach has the potential to be adapted and expanded for multicellular control experiments [46], for which currently there are very limited options both commercially and otherwise. Our design consists primarily of 3D printed parts which can be produced using commercially available, widely used 3D printers with a total cost of less than $200.

The results shown in this paper were presented in [58] and were carried out independently from [132] .

4.2 State of the Art

Several low-cost turbidostat designs have been designed and developed entirely by different research groups in academia. The first key milestone design, in this sense, was proposed by the Klavins laboratory in 2015 [134]. An open-source multiplexed turbidostat system capable of running up to eight parallel culture chambers was designed. Turbidity was measured via a 650 nm laser diode optically coupled with photosensors placed either side of each culture chamber. Each turbidostat chamber houses its own electronics allowing each to take individual turbidity measurements. By utilising a multiplexed syringe pump system, the need for eight syringe pumps is scaled down to just a single pump, whilst still enabling individual chambers to be supplied with fresh media when required. The total cost of building this open-source design is under $2000.

In 2016, researchers from the Khammash laboratory proposed a different turbidostat design [102] inspired by that of the Klavins lab. They added additional optogenetic features to enable the regulation of GFP production in *Escherichia coli*. In their experiments, GFP production from *Escherichia coli*, which depends on the ratio of green to red light, was controlled by integral feedback. This was accomplished by adding an automated sampling system to connect the turbidostat chamber to a FACS machine. Real-time FACS analysis enabled quantification of cell fluorescence profiles. This information was then sent to the controller, which determined the ratios of green to red light to supply to the culture chamber. This design used a 950 nm laser diode to prevent overlap in the wavelengths absorbed by the photosensitive proteins within *Escherichia coli*. Key differences between this design and the Klavins design in [134] are the use of peristaltic pumps for the dilution of culture media, automated sampling and the use of optogenetic control.

A different, more complex, turbidostat design was presented in [61]. In this design, the optical density is calculated by comparing light absorption from the culture flask to a second flask that contains only growth media, acting as a blank solution. This method allows for online calibration of the OD measurements; however, it complicates the overall design, increasing implementation costs.

Another turbidostat implementation was recently presented in [100], where a flexible machine was designed. Their solution requires minimal 3D printed structure and electronics that can be implemented on commercial boards based on ATMEL processors.

A full experimental platform, known as eVOLVER [146], has been developed to control the conditions for high-throughput growth of yeast and bacteria. The device manages up to 16 40mL culture vessels at the same time, regulating their temperature, OD, and stir rate. The complete solution leverages several commercial microcontrollers and a `Python` based framework and is commercialized at the price of $9950

Finally, a new open-source design, known as Chi.Bio [130, 132], were recently released. This device is composed by several modules that are controlled by a microcomputer that is capable to manage up to 8 reactors simultaneously. The main reactor hosts a standard 30mL flat-bottom tube and LEDs with different wavelengths to perform optogenetics experiments; a driver module for peristaltic pumps is connected to each chamber, feeding them with the media and the inducers required by the experiment. Potentially, the modularity of the design allows this platform be applied to a wide range of use cases [131] .

4.3 Problem Formulation

The aim of the turbidostat design presented in this Chapter is to assemble a *low-cost*, modular and flexible machine that can be easily adapted to a different range of experiments. Our design can also be extended into more complex set-ups such as those required for the implementation of multicellular control experiments, which will be discussed in the next Chapter. In comparison to other available designs, our machine has the following advantages:

1. It is based on an open-source Arduino-based [1] hardware and software code, increasing its flexibility to be used for different types of experiments;
2. It allows, through some mechanical improvements, the housing of the optical density apparatus to slide, allowing the height to be adjusted to compensate for the volume inside the culture chamber;
3. It contains an Input/Output user interface to run the machine without the need for a computer connection, being effectively a stand-alone machine.

4.3.1 Design Principles

From a control engineering viewpoint, our turbidostat schematic can be summarised as reported in Figure 4.1. Here, the culture chamber hosting the population of bacteria is the system to control or “plant". Its output of interest (optical density) is sensed via a light sensor and fed to the controller, which, given the reference, evaluates the control input and drives the pump (actuator).

In the design and in the assembly of our turbidostat, we were inspired by the following principles:

- Flexibility: both hardware and software must be flexible enough to accommodate different experimental specifications.

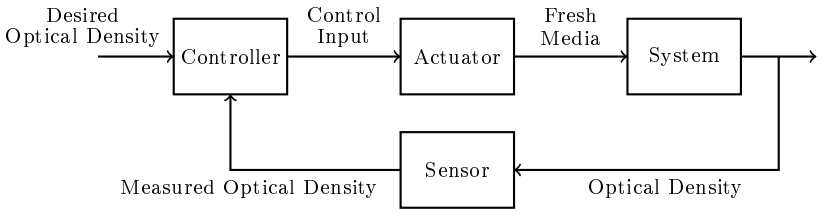

Figure 4.1: Control Engineering schematic of the Turbidostat control loop.

- Modularity: the bioreactor must be made up by independent modules that can be added or removed whenever needed.
- Adaptability to the experiment: components of the machine must not interfere with the experiment it hosts, i.e. the Optical Density regulation must not have impact on the experiment.
- Autonomy: the machine can be operated in a stand-alone mode, without the need for a connection to a computer.

A schematic of our implementation is reported in Figure 4.2. The following items are needed:

- An *incubator*, which encases the culture chamber and the media tank. It keeps the temperature of the machine to 37°C in order to maximize the growth rate of the bacteria involved in the experiment.
- A *media tank* that stores the reservoir of culture media and a controlled pump that injects it into the experiment chamber.
- An *air pump*, which supplies air to the culture chamber to guarantee bacteria aeration. Moreover, in our design, the air pump increases the pressure inside the chamber creating a pressure gap with the outside. This mechanism is used to push the exceeding solution to the outlet channel.
- A *motor* that continuously stirs the solution avoiding bacterial aggregation and creating a homogeneous solution. This motor is placed under the chamber and it moves a magnetically connected element placed within the culture chamber.
- An *outlet channel* that acts both as sample collecting line and as waste outlet. Driving a pinch valve, it is possible to select the path of the removed solution, choosing a path to the sample collector or to the waste bottle.

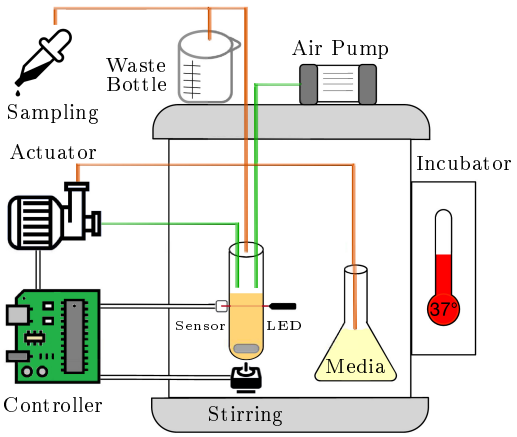

Figure 4.2: Schematic Representation of the Turbidostat. The test tube that hosts the population of bacteria is magnetically connected to a motor that stirs the solution. The bacteria and the fresh media are placed inside an incubator to keep the temperature at 37°C, to maximize bacteria's growth rate. The air pump pushes out exceeding solution when new fresh media is injected in the chamber. The removed solution ends in the sample collector or in the waste bottle

4.4 Design

In the following section, we give an essential description of all the parts included in the design of our turbidostat. First, we describe all the mechanical parts involved in the design, from the housing to the actuators. Then, we focus on the design of the electronics, introducing the main controllers and all the modules that compose the machine. Finally, we introduce the control algorithm embedded into the device. More details and the complete list of all parts can be found in the Appendix A.

4.4.1 Mechanical Parts

Being focused on low cost and reproducibility, we designed all the mechanical parts of the machine so that they can be easily 3D printed. They were designed using a parametric CAD software, to guarantee the maximum adaptability of the device to chambers with different culture volumes. List of the 3D printable parts can be found in the Appendix A.

The chamber support, shown in Figure 4.3, is inspired by the one designed in [134] by Klavin's Laboratory. In our design, the stirrer slot has been adapted to host a DC motor, in place of the stepper motor used therein yielding a simpler speed control strategy of the motor. In this way, ad-hoc drivers are not needed for DC motors, simplifying the entire connection schematic.

A sliding support for the sensing circuit also allows us to regulate the height at which the measure of OD is taken. In so doing, it is possible to adapt the machine for the use of different culture volumes and test tubes. Moreover, sliding supports can be useful to achieve redundancy: it is, indeed, possible to place more than a single sensing circuit on the test tube. The additional circuit can be used as a backup in case of a failure of the principal one, or to enhance a better reading of the optical density of the solution via sensor fusion algorithms.

For the actuation, we tested two different devices, both realised by 3D printing. The first solution, see Figure 4.4, is to use a peristaltic pump driven by a stepper motor. This pump is easy to drive and responds quickly but it is not robust to pressure variations that might result in a backward flow. The pump has been designed on the basis of a parametric CAD design available online [83] ; more details can be found in the Appendix A.

The second solution that was adopted is the combination of an actuated syringe pump, shown in Figure 4.5, and a two-way 3D printed pinch valve. Its driving requires the coordinated work of two servo motors, leading to longer actuation times but better robustness to pressure changes. The syringe pump is the same as that proposed by Klavins Lab, while the two-way pinch valve has been designed from scratch; see details in the Appendix A.

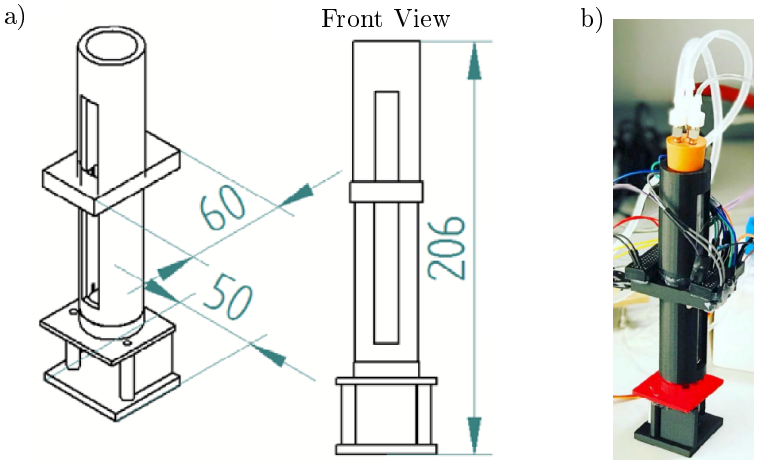

Figure 4.3: 3D printed Chamber support. **a)** CAD model of the chamber support. Size (reported in mm) is optimised for PYREX Rimless 25x200mm test tubes. **b)** Assembled chamber support, with the stirrer motor mounted at the bottom, prototype of the optical density circuit and tube connections at the top. In this first prototype, for testing purposes, the prototypal optical board has been glued onto the camber support loosing its sliding properties.

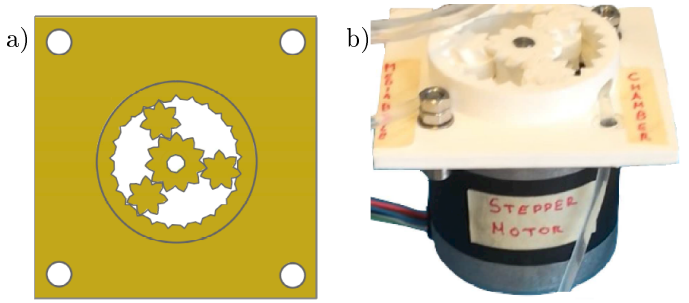

Figure 4.4: Actuation System: Presitaltic Pump. a) 3D model of the Peristaltic Pump; top view. b) Peristaltic pump driven by a stepper motor: A 4mm diameter tube passes inside the rack and it is pressed on the structure by the moving gears. During the rotation of the gears, they create a gap of pressure inside the plastic tube, moving the pressure point, and creating a flow in the same direction of rotation.

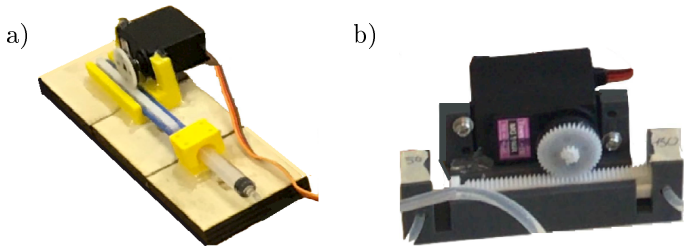

Figure 4.5: Actuation System: Syringe Pump. a) 3D printed syringe pump. The syringe is pushed and pulled via a gear-pinion mechanism driven by a servo motor. b) Mutually exclusive 2-ways 3D printed pinch valve. A gear-pinion mechanism is moved with a servo motor. In the configuration shown in this panel, the way on the left is open while the one on the right is closed.

4.4.2 Components: Electronics and Communication

The core of our machine is an Arduino Mega 2560 board equipped with several modules that will be discussed below. The choice of the main board was to provide the best trade-off between computing power, memory, device management compatibility and costs.

The main board is interfaced with external modules in different ways: analogically, digitally or using a particular protocol of communication (i.e. I2C), see Appendix A for more details.

Optical Density circuit

Optical density is measured using a photodiode in a reverse biased configuration [142], see Figure 4.6. In this working condition, the diode behaves as a light-controlled current source that delivers a current that is related to the Optical Density of the solution. In particular, the higher the optical density, the lower the amount of light transmitted by the solution and sensed by the photodiode. This results in a lower current and thus, a reduction in the sensed voltage. Therefore an inverse relationship between the optical density and the voltage is established. The Optical Density circuit is analogically connected with the main board that reads analogically the voltage V_{out}. In the design of the circuit in Figure 4.6, the resistor R_1 has been tuned to 220Ω in order to feed the LED with an adequate amount of current. The resistor R_2, is a tunable 10$k\Omega$ resistor, that is used to regulate the calibration of the machine. At the beginning of the experiment, a calibration phase is required where the user is asked to place a blank sample of fresh media and regulate the resistor R_2 until the OD reading is 0. More Details about the calibration of this optical board can be found in the Appendix A. In order to enhance robustness against variations of light in the environment, both the LED and the photodiode have been chosen to work with the 950nm wavelength. In particular, the photodiode can be equipped with a pin filter

tuned onto the correct wavelength so as to attenuate the disturbances of light at the other frequencies. As the 950nm light is invisible to the human eye it is mandatory to use of ad-hoc alignment tools like the 3D printed one, shown in Figure 4.6.

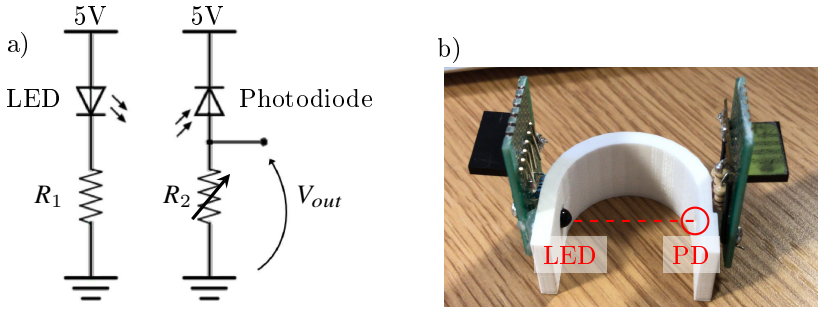

Figure 4.6: Optical density measure circuit. a) On the left, a LED diode is connected to a 5V source through the resistor R1. On the right, a photodiode is connected in a reverse bias configuration; it behaves as a light controlled current source. The output measure V_{out} is the voltage at the ends of the tunable resistor R_2. b) Prototype of optical density measure circuit hosted in a 3D printed support. The red dashed line represents the light ray, starting from the LED (OSRAM SHF 4544), that hits the photodiode PD (Vishay Semi-conductors BP104).

Motors' Drivers

Independently from the particular choice of the actuators, there will be motors that must be driven. In the previous section, however, we distinguished the stepper motor that drives the peristaltic pump from the servo motors that control the syringe pump. Beside the actuation, a DC motor for the stirring must always be driven. A common and handy way to manage different kinds of motors is to use a motor shield. A motor shield is a board that is connected to the main one and integrates all the components needed to drive motors of interest.

In our design, we adopted the Adafruit Motor Shield v2 [49]. This shield can drive three different types of motors – DC motors, stepper motors and servos – being perfectly apt for our purpose. The module comes with a very useful I2C based library that simplifies the coding of the control algorithm.

Other Interface Modules

With the aim of having a stand-alone turbidostat, we installed an interactive LCD character display to show real-time messages on the status of the machine to the operator. The display works with the I2C communication protocol. The experiment can be set up via inputs collected with a simple digital membrane keypad, useful to choose the setpoint and to start the experiment.

The device is, also, equipped with an SD card reader and a Real-Time clock module. With the operation of these two components, it is possible to continuously acquire a complete log of the experiments. The log is saved into a comma separated value (.csv) file, easily readable with any PC. Both components communicate with the main board via a set of digital pins.

4.4.3 Control Algorithm

The control code of the main Arduino board is divided into an initialization and a routine part. During the first phase, all the modules are set up, the OD reference is set via calibration and the set-point is chosen. The second phase, that is a looping one, is divided in five parts, as follows:

1. *Measure*: The voltage V_{out} (see Figure 4.6) is read. Multiple measures (usually 20) are collected and averaged in order to mitigate possible reading errors. The average voltage is, then converted into the OD via an estimated conversion formula (see Appendix A for further details). During this measure process, the stirring is stopped in order to mitigate the effects of possible whirlpools.
2. *Control*: The measured OD is subtracted from the reference value to calculate the control error. The error is then sent to an empirically tuned PI controller that evaluates the control action in terms of mL of solution that needs to be added into the chamber.
3. *Actuation*: The control action is converted into a driving signal for the particular actuator of choice. When the driving is operated via a peristaltic pump, this is driven at a fixed velocity for the amount of time needed to deliver the control action. If a syringe pump is adopted instead, it is possible to drive the servo to an angular position proportional to the desired control action. After this conversion phase, the actuator is driven.
4. *Log*: At the end of the actuation, the data about the control cycle is written down in the log file saved on the SD card. In particular, we log information about the time, the measured OD, the control error and the control input.
5. *Waiting*: the algorithms wait for the next control period, to guarantee equally time spaced control cycles. The usual control period in our experiments is $T_s = 60s$. The algorithm, then waits for $T_s - T_c$ seconds, where T_c is the effective computation time counted by the real time clock module starting from the beginning of the last control period.

This part of code is routinely executed until the experiment is terminated by

the user via the keypad or when the programmed duration of the experiment is reached.

4.5 Experimental Regulation of the Optical Density

In order to test and validate our design, we conducted a 3 hour long closed-loop optical density regulation experiment. The results of the last experiment are reported in Figure 4.7. The goal is to regulate the OD of a *Escherichia Coli* (strain MG1655) bacterial culture. The starting OD600nm is 0.04 and the desired OD600nm value is set to 0.10. During the first phase, approximately 35 minutes, the controller allows the optical density to grow until the setpoint, without any dilution of the solution. Then the regulation phase begins and an amount of fresh media is supplied to the solution. This correcting amount is evaluated by a PI control law and is a function of the difference (and its integral) between the measured and the desired OD value. For the entire duration of this phase, the optical density falls within the acceptable range [0.09, 0.11], with an observed peak of 0.12, possibly the result of measurement noise.

Samples of the solution have been taken at the beginning and at the end of the experiment. Their OD has been measured with a commercial spectophotometer (WPA CO 8000 Cell Density Meter) with the initial reading of 0.04 and the final reading of 0.10.

4.6 Discussion and Possible Upgrades

In this Chapter we presented a low-cost turbidostat design inspired by that of [134] that was developed to maximise flexibility and ease of implementation. All the parts needed to assemble the turbidostat can be easily 3D printed and assembled following the instructions in the Appendix A.

Using an Arduino micro-controller, a peristaltic or syringe pump, and a photodiode in a reverse bias configuration, the design we presented is self-contained and can be easily driven by a provided user interface equipped with a display and a keyboard. Closed-loop control of the OD is achieved via a PI controller tuned heuristically. Calibration and control experiments were performed confirming the effectiveness of our design.

The design is simple and modular enough to be adapted and extended for use in different control set-ups. For example, optogenetics, which requires the use of LEDs with fixed wavelength (red 650nm, green 535nm), does not interfere with the optical density sensing circuit, that works using 950nm wavelength.

In the next Chapter, the problem will be addressed of designing a multi-chamber turbidostat architecture to host multiple species of bacteria, guaranteeing their coexistence and regulating their relative concentration ratio, as this will become increasingly crucial for the validation of multicellular control strategies as described in Chapter 3.

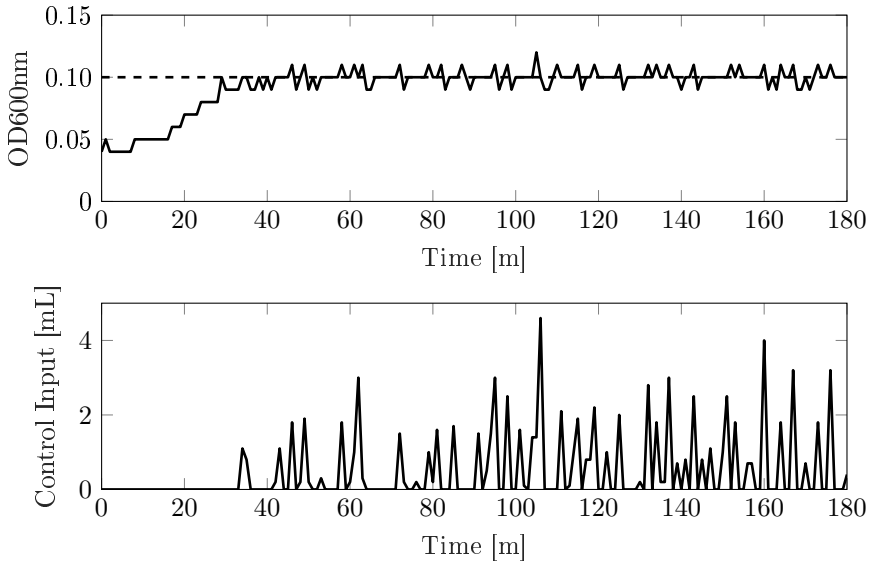

Figure 4.7: OD regulation Control experiment. *Escherichia coli* strain MG1655 was grown in LB medium. Duration of the experiment: 3 hours. The setpoint of the experiment was 0.10; initial value of the OD was 0.05. During the first 30 minutes, the solution was left growing until it reached the setpoint; then the regulation phase began. The PI controller gains are $K_p = 30$ and $K_i = 1$. Sampling Time $T_s = 1$ min.

5 Towards a bioreactor for Multicellular Control Experiments

5.1 Introduction

In vivo experiments with coexistence of different species of bacteria are of utmost importance for the development of synthetic biology. One of the motivations is that embedding complex gene regulatory networks in a single living cell is hard due the excessive metabolic burden [108]. Therefore, the key to achieving new functionalities is to decompose the complex system in elementary pieces, distributing them across different populations specialized in simple tasks [16, 46, 97]. However, this paradigm assumes that different bacterial species can coexist at the same time, a situation that is not easy to realize in practice. Due to unavoidable differences in their genetic loads, all cell populations in the consortium will grow at different rates resulting in undesired dynamics, such as oscillations or even leading to extinction [118]. To conduct *in vivo* experiments where different species of bacteria coexist, a host device, or bioreactor, must be designed to compensate these dynamics and guarantee coexistence.

Moreover, in industrial applications where high production efficiency is required, external control strategies should be preferred to embedded solutions, because additional genetic circuits can cause further metabolic burden to the cells and hence lower production rates of the desired metabolic end products.

Microfluidics devices are now available and ideal to allow spatial separation of two different microbial species inside adjacent micro-chambers, guaranteeing the exchange of metabolites via connecting nanochannels [18]. Other studies also show that microfluidics traps are effective to guarantee the coexistence of different bacterial strains, while they exchange signaling proteins [4].

Many results have been presented in the literature, both in microfluidics and in continuous culture devices; however, very few results are available for multiple-strains, cultures or microbial consortia besides the above mentioned solutions. This is due essentially to classical optical-based regulation methods being inef-

fective to regulate more than one bacterial population at the time. However, examples of bioreactors that guarantee coexistence of multiple species exist, but they require very complex control mechanisms [77].

Continuous reactors are machines where the reactant – that is the substrate in the biological case – is continuously fed into the reactor. Compared to batch reactors, where the tank is sufficiently large to handle the entire batch cycle, they show several advantages such as their greater flexibility and their smaller dimension.

In this Chapter we address the problem of designing control schemes for continuous bioreactors to carry out experiments with two coexisting species of bacteria. Firstly, we present control strategies for a simple 1-chamber layout, with two cell populations mixed together; we analyse the conditions under which coexistence is assured, we design two different control strategies and we discuss their closed loop dynamics via *in-silico* experiments. Then, with the aim of overcoming some limitations that undermine the effectiveness of the simple 1-chamber layout, we propose a new 3-chamber layout, with two growth chambers and a mixing one, formulating its mathematical model and designing an effective control strategy.

State of the art on the dynamics of multiple competing species

The study of the dynamics of two species cocoultured in the same bioreactor has been addressed multiple times in the literature, from different points of view. The first important result, in this sense, is the study of the competition between different species that live in the same vessel [68]; this may be a deliberate culture of mixed populations or may arise as the result of contamination or mutation of the strains being cultured. By using a general deterministic model for one substrate and n competing species – with Michaelis-Menten growth functions [70] – the authors of [68] state that the species with the smallest Michaelis-Menten constant wins the competition at steady-state. However, it has been proved that, relaxing the concept of coexistence, it is possible to have the survival of multiple species. For example, considering biological Lotka-Volterra models and moving from coexistence at steady state (with fixed densities) to cyclic trajectories [10], it is possible to have coexistence when the feeding source is biotic (governed by a differential equation) and abiotic (result of an algebraic relationship). Then, extensive work has been conducted to study coexistence in the presence of periodic dynamics of the limiting feeding source. Recently, it has been proved that coexistence is possible even in the presence of random fluctuations in the inlet flow of continuous bioreactors. Modelling the control input as an Ornstein-Uhlenbeck process, it is possible to find conditions under which the coexistence of species is assured [22].

Also, state feedback control of the dilution rate (i.e. the ratio between the inlet flow and the total working volume) can be used to ensure different species coexist in a chemostat [33]. The resulting closed loop system shows a stable equilibrium point in the positive orthant to which all solutions converge. However, work in [33] does not consider any other design requirement on the state of the system.

Despite this previous research, there are still many phenomena that arise when multiple species coexist that are not fully understood. As an example, let us consider *overyielding*, that is the capacity of certain ecosystems to exhibit better growth performances compared to when their composing species are cultivated alone. Models that describe this phenomenon are rare in the literature, especially in the case of continuous bioreactors [38]. However, recent work in [60] showed how several biological mechanisms could produce overyielding in microbial ecosystems, using models of growth in batch cultures.

The presence of multiple species in the same environment could be the unwanted result of contaminations or mutations [115]. When this happens, if the invading species have better growth properties compared to the resident one, the continuous bioreactor must be controlled so as to mitigate the effects of the invader. In recent work in [135], the authors analyse the dynamics of the competition and design a geometrically-based hybrid control strategy to guarantee resilience against species invasion in a chemostat. The control strategy does not require precise knowledge of the growth characteristics of the invader and is able to create a periodic solution in which the survival of the resident species is assured.

Complex control architectures that drive *Multiple Input Multiple Output* (MIMO) systems can robustly stabilize different species in the same vessel of a bioreactor. In recent work [34], a control strategy that varies the concentration of the limiting substrate in the inlet flow and its resulting dilution rate via Sliding Mode Controllers is able to stabilize the concentrations of two species to some given desired value. The result is of clear importance; however, there are strict limitations that undermine its applicability as recognised by the authors themselves. It is indeed possible to stabilize only one of the two competing species while guaranteeing the other does not become extinct but the implementation of the control law on a continuous bioreactor is limited by the chattering showed by the Sliding Mode Controller in the regulation of the concentration of the limiting substrate.

5.2 The Single Chamber Bioreactor with a Single Species

The following model, proposed for the first time in [13] and widely adopted in the literature [32, 135], describes the dynamics of a continuous bioreactor:

$$\begin{cases} \dot{x} = (\mu(x, s, \mathbf{q}) - D(t))x \\ \dot{s} = -\frac{1}{Y}\mu(x, s, \mathbf{q})x + D(t)(s_{in} - s) \\ \dot{\mathbf{q}} = \mathbf{Q}(x, s, \mathbf{q}, D(t)) \end{cases} \tag{5.1}$$

In the above model, the term $x \in \mathbb{R}_+$ represents the concentration of biomass [mg/mL] of a bacterial species; $s \in \mathbb{R}_+$ is the concentration of the substrate [mmol/mL] feeding source; the vector $\mathbf{q} \in \mathbb{R}_+^p$ is a vector representative of time-varying dynamical parameters that affect the growth dynamics of the biomass. The parameter $s_{in} \in \mathbb{R}_+$ is the substrate concentration in the inlet flow and

$D(t) \in \mathbb{R}_+$ is the dilution rate [1/h], defined as the ratio between the inlet flow [mL/h] and the working volume [mL]. The parameter Y is the substrate-biomass conversion rate [mmol/mg]. In this study, the parameter s_{in} is assumed to be constant, therefore the unique control input of the system is $D(t)$.

Model (5.1) does note take into account any kind of cell death phenomena; in this mathematical description, the concentration of biomass can be reduced only by dilution.

The function $\mu(s, x, \mathbf{q})$ is the so-called growth function [1/h] that satisfies the following assumptions:

A1. $\mu(x, 0, \mathbf{q}) = 0$;
A2. $\mu(x, s, \mathbf{q}) > 0, \ \forall s > 0$;
A3. $\mu(x, s, \mathbf{q}) \leq \mu_{\max}, \ \forall x, s, \mathbf{q} > 0$;
A4. $\mu(x, s, \mathbf{q}) \in C^1$.

The state vector $\mathbf{q}$ is the aggregation of some physical quantities that affect the reaction – such as temperature, pH, oxygen saturation, et cetera – with complex and partially unknown dynamics, being in some cases difficult to measure in real time. The level of detail reached by this kind of description goes far beyond the scope of this study; therefore we assume that $\mathbf{q}$ is a vector of constant parameters $\bar{\mathbf{q}}$, and their dynamics is thus neglected. Under this assumption, the growth function can be approximated as $\mu(x, s, \mathbf{q}) \simeq \mu(x, s, \bar{\mathbf{q}}) = \mu(x, s)$. Also, without loss of generality, it is possible to set $Y = 1$ normalizing the biomass unit. These manipulations yield the following simplified model that describes the growth of biomass inside the bioreactor vessel:

$$\begin{cases} \dot{x} = (\mu(x, s) - D(t))x \\ \dot{s} = -\mu(x, s)x + D(t)(s_{in} - s). \end{cases} \tag{5.2}$$

Open-Loop Analysis

To better understand what the physical implications of the model are, we first compute the equilibria of system (5.2). Suppose that the input is constant, that is $D(t) = D \geq 0$, then the equilibrium points can be obtained by solving:

$$\begin{bmatrix} (\mu(x, s) - D)x \\ -\mu(x, s)x + D(s_{in} - s) \end{bmatrix} = \begin{bmatrix} 0 \\ 0 \end{bmatrix}.$$

If $D \neq 0$, the system has two possible equilibrium points:

- An equilibrium point in $[0, s_{in}]^\top$;
- An equilibrium point $[\bar{x}, \bar{s}]^\top$, with $\bar{x} > 0, 0 < \bar{s} < s_{in}$, corresponding to the condition such that the growth rate and the dilution rate are equal, that is, $\mu(x, s) = D$.

Without performing a proper bifurcation analysis for system (5.2), it is important to notice that for $D > \mu_{\max}$ (from assumption A3) the system has a single globally attractive equilibrium point in $[0, s_{in}]^\top$; this equilibrium point is a node.

Assume system (5.2) is forced by an input $D(t)$ such that

$$\int_0^{+\infty} D(\tau)d\tau = +\infty, \tag{5.3}$$

it is possible to prove that, no matter what the initial conditions of the system,

$$\exists\ \bar{t}\ :\ s(t) \in (0, s_{in}]\ \forall t > \bar{t}.$$

This means that, there exists a time value $\bar{t}$ after which the substrate is always bounded in the range $(0, s_{in}]$. The reader can have an intuition on why this is true considering the case of forcing the system (5.2) with a constant positive input $D(t) = D > 0$ from the initial state $\mathbf{x_0} = [0, s_0]^\top$. Three possible cases can occur:

1. $0 \leq s_0 < s_{in}$: the product $D \cdot (s_{in} - s_0)$ is positive and the system will converge to the equilibrium in $[0, s_{in}]^\top$;
2. $s_0 = s_{in}$: the product $D \cdot (s_{in} - s_0) = 0$ and the system has an equilibrium in the point $\mathbf{x_0}$.
3. $s_0 > s_{in}$: the product $D \cdot (s_{in} - s_0)$ is negative and $s(t) < s(0) = s_0, \forall t > 0$. As in the first case, the system will converge to the equilibrium in $[0, s_{in}]^\top$.

The result still holds even in the case of non-zero biomass concentrations, i.e. $x(0) = x_0 > 0$. In this case, for $D < \mu_{\max}$ the dynamics converge towards $[\bar{x}, \bar{s}]^\top$, whereas for $D > \mu_{\max}$ they converge towards $[0, s_{in}]^\top$.

The limitation on the possible values that the substrate concentration can assume, together with the assumption of unitary yield factor Y, leads to limitations on the biomass value x in the same range of values; in addition, the biomass can also assume the null value. Thus, it is possible to state that

$$\exists\ \bar{t}'\ :\ x(t) \in [0, s_{in}]\ \forall t > \bar{t}'.$$

That is, similarly to the case of the substrate, there exists a time value $\bar{t}'$ after which the biomass is always bounded in the range $[0, s_{in}]$.
Therefore, the subset $\mathcal{A} = \{(x, s) \in [0, s_{in}] \times (0, s_{in}]\}$ (depicted in Figure 5.1) is attractive and forward invariant for the system (5.2).

Oppositely, when the dilution rate $D(t)$ is vanishing

$$\int_0^{+\infty} D(\tau)d\tau < +\infty,$$

(for example, if it is a bounded energy signal such that $D(t) = 0, \forall t > \bar{t}$ or when $lim_{t\to\infty} D(t) = 0$) the system settles to an equilibrium point $[\bar{x}, \bar{s}]^\top$ such that either $\bar{x}$ or $\bar{s}$ vanish. These are trivial and uninteresting cases that correspond to the following physical conditions:

- when $D(t) > \bar{D}$ for a given interval of time, the system converges towards $[0, s_{in}]^\top$ and the machine is in the wash-out condition; this happens when the initial non-null biomass in the chamber is completely flushed out by a high value of the dilution rate.

- when $D = 0$ the system settles onto an equilibrium point where $\bar{x} \neq 0, \bar{s} = 0$. In this case, the surviving biomass has no substrate to sustain its own life; thus, the model loses its physical sense.

Moreover, in the absence of forcing (i.e., $D(t) = 0, \forall t > 0$) and starting from a state (x_0, s_0) with both $x_0, s_0 > 0$, the system will converge to $(x_0 + s_0, 0)$. This statement finds explanation recalling the assumption A1 on the growth function. The biomass will increase until the substrate concentration will be positive, stopping its growth only when $s = 0$; being the yield factor unitary, the increase of the biomass is equal to the decrease of the substrate.

Existence of an Attractive and Invariant Domain

It is possible to prove that the surface $\Sigma := \{(x, s) : s_{in} - x - s = 0\}$ is attractive and invariant for any trajectory of the system (5.2), when forced with a positive constant input $D(t) = D$. The proof can be conducted considering a state function $\sigma(x, s) = s_{in} - x - s$ and showing that $V = \frac{1}{2}\sigma^2(x, s)$ is a Lyapunov function for the system trajectories. With this aim, we show that $\dot{V} = \sigma\dot{\sigma} < 0$. By denoting $\mathbf{x} = [x, s]^\top$, the proof of attractiveness follows from the fact that:

$$\begin{aligned}\dot{V} = \sigma\dot{\sigma} = \sigma \frac{d\sigma}{d\mathbf{x}} \frac{d\mathbf{x}}{dt} = (s_{in} - x - s)[-1 - 1] \begin{bmatrix} (\mu(x, s) - D)x \\ -\mu(x, s)x + D(s_{in} - s) \end{bmatrix} = \\ = (s_{in} - x - s)(-\mu(x, s)x + Dx + \mu(x, s)x - D(s_{in} - s)) = \\ = -D(s_{in} - x - s)^2 < 0,\end{aligned}$$

with $D > 0$ by assumption. The fact that Σ is attractive is easily proved by considering that:

$$\dot{\sigma}|_{\sigma=0} = -D(\sigma)|_{\sigma=0} = 0.$$

As noted before, the unitary yield factor Y leads to an increase of the biomass equal to the decrease of the substrate; this means that their sum is constant when

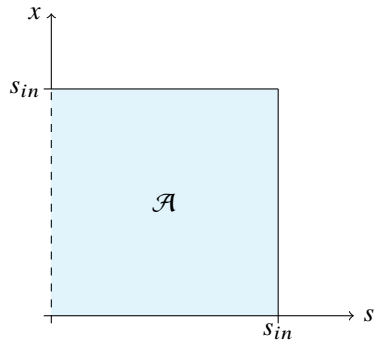

Figure 5.1: Subset $\mathcal{A}$ for the system (5.2).

$D(t) = 0$. Therefore, it is trivial to conclude that the result holds also in the case when $D(t) = 0$ in some intervals, as long as these intervals are limited.

Finally, we can conclude that the existence of the attractive and invariant surface Σ implies that

$$\lim_{t\to\infty} [s_{in} - x(t) - s(t)] = 0.$$

5.3 The Single Chamber Bioreactor with Two Species

The single species model (5.2) can be extended to the case of two biomass species x_1 and x_2 competing for a single substrate feeding source s [135]. The system is characterized by an additional equation that describes the evolution of the second species biomass x_2 and its relative consumption term in the substrate equation. Thus, the model is given by:

$$\begin{cases} \dot{x}_1 = (\mu_1(x_1, s) - D(t))x_1 \\ \dot{x}_2 = (\mu_2(x_2, s) - D(t))x_2 \\ \dot{s} = -\mu_1(x_1, s)x_1 - \mu_2(x_2, s)x_2 + D(t)(s_{in} - s). \end{cases} \tag{5.4}$$

with the obvious extensions of all the notation, symbols and assumptions on the growth functions. Moreover, without loss of generality, it is convenient to assume that both the two species have unitary yield factor, $Y_1 = Y_2 = 1$. Being the two species hosted in the same reaction chamber, the input $D(t)$ is common to the three equations that compose the model; thus, assuming the *well-mixed* hypothesis, the removal rates of the species are identical.

The results on convergence of trajectories of the system (5.2) – when forced with a non-vanishing $D(t)$ – in the subdomain $\mathcal{A}$ of Figure 5.1 can be extended with ease, for model (5.4), to the three dimensional space. In this case, the limitation on the substrate and the identical yield factors of the two species lead the trajectories of the system to evolve in the attractive and invariant domain

$$\mathcal{D} = \{(x_1, x_2, s) \in [0, s_{in}] \times [0, s_{in}] \times (0, s_{in}]\}.$$

A representation of the domain $\mathcal{D}$ is shown in Figure 5.2.

Competitive Exclusion Principle and Species Survival

An important result on the coexistence of two species competing for the same feeding source, known as the Competitive Exclusion Principle, states that *at most one species survives at steady-state* in the system (5.4), when forced with a constant and positive dilution rate D. *This result holds when the growth functions are monotonically increasing and they intersect in a single point*; typically, when two species are present, one wins the competition for low concentration of the substrate, the other for high concentration of the substrate [135, 125, 68]. Since

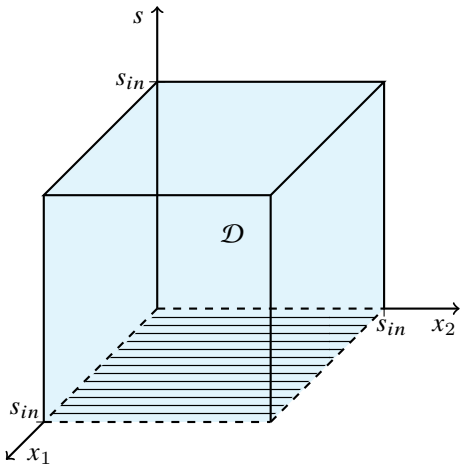

Figure 5.2: Geometrical representation of the domain $\mathcal{D}$ for the system (5.4).

$\mu \in C^1$, this scenario is captured assuming that there exists some $\tilde{s} \in [0, s_{in}]$ such that

$$(\mu_1(s) - \mu_2(s))(s - \tilde{s}) > 0, \;\; s \in [0, s_{in}], s \neq \tilde{s}. \tag{5.5}$$

That is, for $s < \tilde{s}$ it holds $\mu_2(s) > \mu_1(s)$, while for $s > \tilde{s}$ it holds $\mu_1(s) > \mu_2(s)$.

Existence of an attractive and invariant domain

It is possible to extend the result on the attractiveness and invariance of the surface Σ proved for the single species model (5.2) to the case of the two species model (5.4).

In the three dimensional case, indeed, we can prove that there exists an attractive and invariant subset of $\mathbb{R}^3$ defined as:

$$\mathcal{S}_a = \{(x_1, x_2, s) : \; x_1 + x_2 + s = s_{in}\}.$$

The proof of existence can be easily conducted by extending the definition of the state function $\sigma(x, s)$ to the case of $\sigma(x_1, x_2, s)$.

The geometrical interpretation of the subset $\mathcal{S}_a$ is a plane whose intersection with the domain $\mathcal{D}$ can be depicted as shown in Figure 5.3.

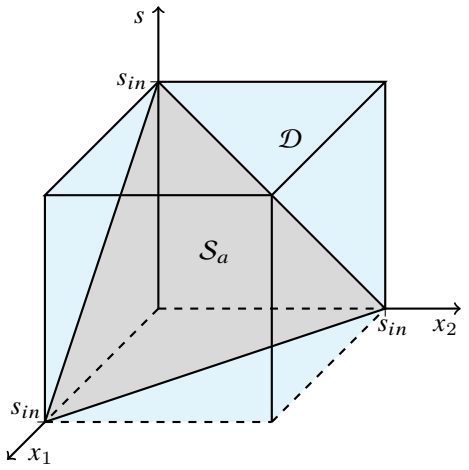

Figure 5.3: Geometrical representation of the domain $\mathcal{S}_a$

Reduced Order Model

Assuming that the evolution of system (5.4) belongs to subset $\mathcal{S}_a$, it is possible to reduce its dynamics to that of a planar system, considering satisfied the constraint $x_1 + x_2 + s = s_{in}$, yielding:

$$\begin{cases} \dot{x}_1 = (\mu_1(x_1, x_2) - D(t))x_1 \\ \dot{x}_2 = (\mu_2(x_1, x_2) - D(t))x_2 \end{cases} . \tag{5.6}$$

System (5.6) is defined in a planar region that is the intersection of the first quadrant of the plane (x_1, x_2) and the region where the constraint $x_1 + x_2 \leq s_{in}$ is satisfied. The domain of definition of system (5.6) is reported in Figure 5.4.

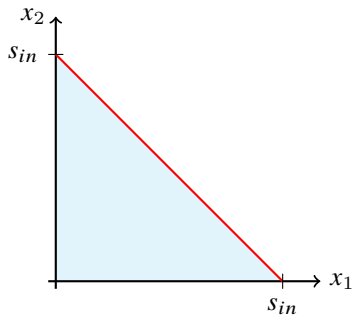

Figure 5.4: Domain of definition of the system (5.6) (cyan region). The red line is described by $x_1 + x_2 = s_{in}$.

5.3.1 Open-Loop Analysis

The growth function

The following section deals with the study of the dynamics of the planar system (5.6) when the growth functions are supposed to be in the Monod form [13], that is

$$\mu_i(x_i, s) = \mu_i(s) = \frac{\mu_i^* s}{k_i + s}, \quad i = 1, 2. \tag{5.7}$$

In the reduced system (5.6), the growth functions $\mu_i(s)$ depend only on the concentrations of both species, due to the constraint $s = s_{in} - x_1 - x_2$. Thus, their expressions become:

$$\mu_i(s) = \mu_i(x_1, x_2) = \frac{\mu_i^*(s_{in} - x_1 - x_2)}{k_i + s_{in} - x_1 - x_2}, \quad i = 1, 2.$$

Recalling equation (5.5), we assume that the two growth functions $\mu_i(x_1, x_2)$ intersect each other in a single point $\tilde{s}$. Or equivalently,

$$\exists!\ \tilde{s} : \ \mu_1(\tilde{s}) = \mu_2(\tilde{s}).$$

This situation is represented in Figure 5.5, where regions of the plane in which one species grows more than the other are depicted. Without this last assumption, considering monotonically increasing growth functions as in (5.7), there would be a dominance of one growth function onto the other. If this is the case, one species will always win the competition onto the other and coexistence will not be possible.

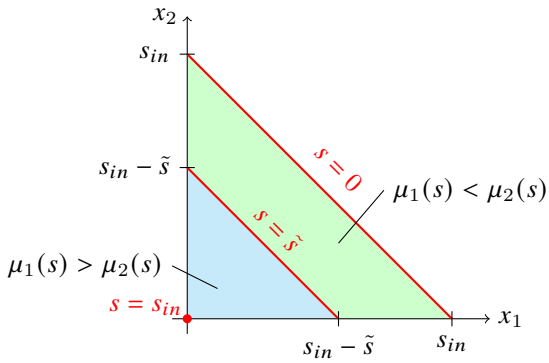

Figure 5.5: Growth functions of the reduced order model. The domain of definition of the model (5.6) is divided in two zones: in the cyan zone, biomass x_1 grows faster than biomass x_2; in the green one, the opposite.

Nullclines of the system

It is possible to compute the nullclines of system (5.6) in closed form. By looking at the equations, each component of the vector field has two possible nullclines: one is independent from the parameters of the model, the other one depends on the species growth function and on the input $D(t)$. The two invariant nullclines associated to the two dynamics are

$$x_1^{(1)} = \{x_1 = 0\}, \quad x_2^{(1)} = \{x_2 = 0\}.$$

These two invariant nullclines always intersect in the origin of the phase plane of model (5.6), giving birth to a persistent equilibrium $(\bar{x}_1, \bar{x}_2) = (0, 0)$ – note that here, the word "persistent" refers to an equilibrium that is fixed and always present, whatever the parameters of the model are. So, the equilibrium point in the origin can only change its stability properties. The other two nullclines depend on the parameters of growth functions – namely μ_i^* and k_i – and on the value of the dilution rate $D(t)$. Moreover, they share the same form, being lines with slope equal to -1 on the plane (x_1, x_2). They can be computed as:

$$x_i^{(2)} = \{x_2 = -x_1 + s_{in} - \tilde{s}_i\}, \quad \tilde{s}_i = \frac{k_i D(t)}{\mu_i^* - D(t)}, \quad i = 1, 2. \tag{5.8}$$

Obviously, $x_1^{(1)}$ always intersects $x_2^{(2)}$ and $x_1^{(2)}$ intersects $x_2^{(1)}$. However, here only intersections of nullclines having physical sense – and so belonging to the domain of definition of system (5.6) reported in Figure 5.4 – are considered.

Position of the equilibria

In this section, a numerical investigation about the position of the equilibria of the system is conducted. First of all, for the sake of simplicity, the parameters of the growth functions are set to be as in [135]:

$$\mu_1^* = 0.5, \quad k_1 = 5, \quad \mu_2^* = 0.16, \quad k_2 = 0.13.$$

These choices make the two growth functions $\mu_1(s)$ and $\mu_2(s)$ of the model (5.4) (depicted in Figure 5.6) intersect at a specific value

$$\tilde{s}_1 = \tilde{s}_2 = \tilde{s} \simeq 2.2$$

where $\tilde{s}$ is defined in the equation (5.8).
Recalling that the intersection of the nullclines are always onto one of the two axes of the phase plane so that the equilibria always have at least one of the components equal to zero, we can plot how the non-zero coordinates of the equilibria vary as a function of the constant input $D(t) = D$, see Figure 5.7.

The graph in the top panel of Figure 5.7 can be divided into three zones (red, blue, green), according to the number of equilibrium points that the system shows in each one of them. In the red zone, three equilibria exists: a saddle and

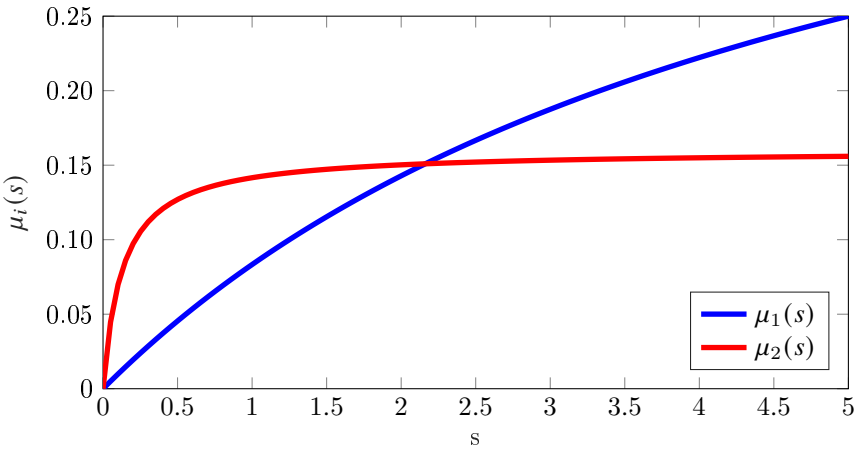

Figure 5.6: Growth functions of the system, μ_1 (in blue) and μ_2(in red) as function of s.

a stable node on the two axes and an unstable node in the origin. The blue zone is characterized by two equilibria: a saddle in the origin and a stable node on the x_1 axis. The green zone corresponds to the flush-out condition, where the only equilibrium is the origin of the phase plane that is a stable node.

The transition from a zone to another is caused by a transcritical bifurcation that occurs at one of the two axes of the plane, with an equilibrium point that leaves the domain of definition of the reduced model (5.6). In the transition between the red and the blue zone, a saddle point on the x_2 axis collapses on the unstable node in the origin; the two equilibria swap their stability characteristics with the equilibria on the x_2 axis (that became an unstable node) leaving the domain of the system (5.6). A similar case is seen in the transition between the blue and the green zone, with a stable node on the x_1 axis hitting the saddle in the origin, becoming a saddle itself and going out of the admissible domain leaving a single globally attractive stable node at the origin.

Equilibrium set and species coexistence

The red zone, the details of which are reported for the sake of readability in the bottom panel of Figure 5.7, is the part of the graph that shows the most complex dynamics. Here, for two values of the input, in particular $D = 0$ and $D = D_{eq}$, where

$$D_{eq} := D = \mu_1(\tilde{s}) = \mu_2(\tilde{s}) \tag{5.9}$$

there exists – beside the unstable node at the origin – a stable equilibrium set $\mathcal{E}$. In the case of $D = 0$, the equilibrium set is the line $x_1 + x_2 = s_{in}$; in the other case, it is the line

$$\mathcal{E} := \; x_1 + x_2 = s_{in} - \tilde{s}, \tag{5.10}$$

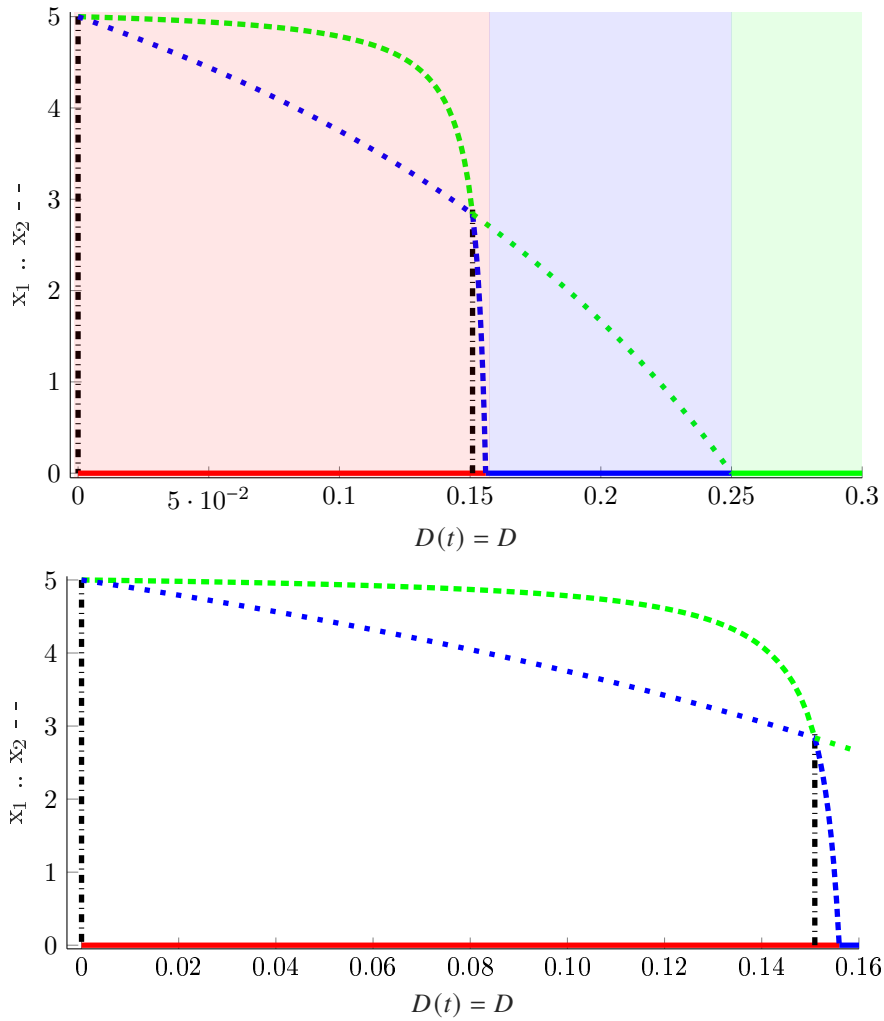

Figure 5.7: Top panel: non zero coordinate of the equilibria of the system (5.6) varying $D(t)$. A variation of the colour of a line represents a change of stability characteristics of an equilibrium. In particular, a red branch represents an unstable node, a green branch a stable node, a blue branch a saddle. Black dot-dashed lines are stable equilibrium sets. The dotted line represents the non null coordinate of the equilibrium on the x_1 axis. The dashed line represents the non null coordinate of the equilibrium on the x_2 axis. The solid line represents the equilibrium in the origin. Bottom panel: Details of the red zone.

where $\tilde{s} : \mu_1(\tilde{s}) = \mu_2(\tilde{s})$. These two cases are reported as dark green dash-dotted lines in Figure 5.7. These two values, $D = 0$ and $D = D_{eq}$, are the only two constant values of $D(t)$ that lead to the stable coexistence of both species. In particular, for these values of the input there exist infinite equilibrium points that are not located on the axes of the phase plane. Note that for the case $D = 0$, the equilibria correspond to the condition $s = 0$, which is not of particular interest; indeed, a null concentration of substrate would lead to extinction of both species, that always physically require a baseline substrate to survive.

When $D = D_{eq}$ a degenerate transcritical bifurcation occurs: the saddle on the x_1 axis collides with the stable node on the x_2 axis through the creation of the equilibrium set $\mathcal{E}$. The result is that, for $D > D_{eq}$ they swapped their stability properties, where the saddle belongs to the x_2 axis and the stable node to the x_1 axis. The equilibrium set $\mathcal{E}$ arises because the two nullclines of the system (5.6) are completely overlapping, leading to the appearance of a continuum of equilibrium points.

A complete representation of the equilibria in the plane is shown in Figure 5.8. Here, the third dimension is the bifurcation parameter D. Each section orthogonal to the D axis shows the number, the position and the stability properties of the equilibria in the phase plane of system (5.6).

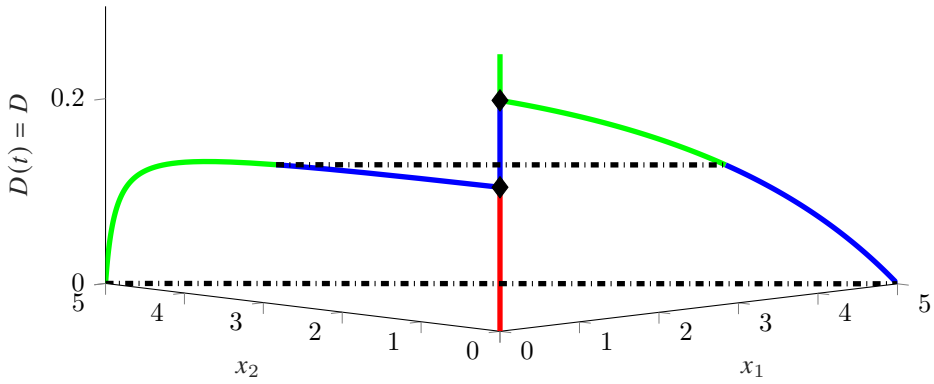

Figure 5.8: Equilibria of the system (5.6) varying $D(t)$. A red branch represents an unstable node, a green branch a stable node, a blue branch a saddle. Black dot-dashed lines are stable equilibrium sets. Black diamonds are bifurcation points.

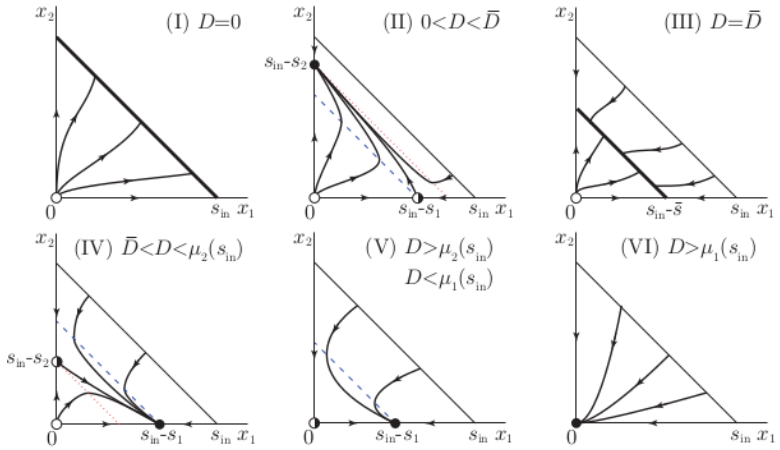

Figure 5.9: Possible state portraits of system (5.6) for different values of constant dilution rate D. Blue dashed and red dotted lines correspond to the two nullclines of the system reported in (5.11) for $i = 1$ and $i = 2$, respectively. Full, empty, and half-filled dots represent stable, unstable and saddle equilibria, respectively.

Phase Plane Analysis

Summing up the results of the phase plane analysis, we can identify the following six cases, corresponding to different positions of the two nullclines

$$x_2 = -x_1 + s_{in} - s_i, \quad s_i = \frac{k_i D}{\mu_i^* - D} \tag{5.11}$$

in the domain of system (5.6) (shown in Figure 5.4), that are depicted in Figure 5.9):

(I) $D = 0$: when $s_1 = s_2 = 0$ the nullclines (5.11) overlap and all solutions asymptotically converge to the stable equilibrium set $\mathcal{E}_0 := \{(x_1, x_2) \in \mathcal{S}_r : x_1 + x_2 = s_{\text{in}}\}$, while the origin is locally unstable. This case corresponds to an undesired working condition in which no new substrate is added to the reactor and the biomass is in starvation. However, this situation can never occur in continuous culture as it is always assumed that $D(t) > 0$, $\forall t > 0$.

(II) $0 < D < \bar{D}$: there are two equilibrium points, each one on an axis, corresponding to their intersection with the nullclines (5.11). Specifically, $x_2^* := (0, s_{\text{in}} - s_2)$ is a stable node and $x_1^* := (s_{\text{in}} - s_1, 0)$ is a saddle, where s_i is as in (5.11), while the origin is locally unstable. This case corresponds to a low concentration of the substrate at steady state due to its consumption and low dilution rate. This results in species 2 prevailing over species 1.

(III) $D = \bar{D}$: the nullclines (5.11) again overlap and all solutions asymptotically converge to the stable equilibrium set (5.10) while the origin is locally

unstable. These equilibrium points correspond to a condition of stable coexistence between the two species.

(IV) $\bar{D} < D < \mu_2(s_{\text{in}})$: this case is similar to case (II) but with opposite stability properties of the equilibrium points, that is, x_1^* is a stable node and x_2^* is a saddle, while the origin is still locally unstable. In this case species 1 prevails at steady state because of the high concentration of substrate.

(V) $\mu_2(s_{\text{in}}) < D < \mu_1(s_{\text{in}})$: there is only one intersection in the domain $\mathcal{S}_{\text{r}}$ between the nullclines (5.11) and the axes at the point x_1^*, which is stable, while in this case the origin is a saddle. At steady state species 2 is flushed-out from the chemostat due to the dilution rate D being greater than its maximum growth rate $\mu_2(s_{\text{in}})$.

(VI) $\mu_1(s_{\text{in}}) < D < D_{\max}$: there is a unique stable equilibrium point in the origin to which all solutions converge. In this case, D being greater than the maximum value of both growth rates causes the flush-out of both species, that is, the cells are removed from the chemostat faster than they can grow.

The transitions between the dynamical behaviors described above are due to bifurcations of the equilibrium points of the system. In particular, in cases (I) and (III) the system undergoes a *degenerate transcritical bifurcation* [81], in which the equilibrium sets $\mathcal{E}_0$ and $\mathcal{E}$ appear, respectively, as the two nullclines (5.11) overlap. These two sets are not structurally stable, since they suddenly disappear for any small perturbation of the bifurcation parameter D from the bifurcation points $D = 0$ and $D = \bar{D}$. On the other hand, for $D = \mu_2(s_{\text{in}})$ ($D = \mu_1(s_{\text{in}})$) the equilibrium points undergo a regular transcritical bifurcation, in which the equilibrium point x_2^* (x_1^*) collides with the one in the origin, exchanges stability and exits the domain $\mathcal{S}_{\text{r}}$.

5.4 Control Problem Formulation

The mathematical model (5.1) is derived under the assumption that cell death is neglected. This assumption is likely true only when a cells have enough substrate to avoid starvation. When running *in-vivo* experiments, a baseline substrate is required to support the viability of the cells. This situation can be taken into account considering the following constraint:

$$s(t) > s_{\min}, \ \forall t > 0. \tag{5.12}$$

Note that this requirement is different from imposing $D(t) > 0$. Indeed, there could be a high concentration of substrate and low concentrations of biomasses; in this case, the constraint (5.12) causes the system to be forced with $D(t) = 0$, that is the best choice to let the biomass grow consuming substrate. Oppositely, considering $D(t) > 0$, there will be a removal of biomass concentration – because of the dilution – that would slow down its dynamics.

Also, the same model completely disregards several phenomena (i.e., a species invasion or another effect that lowers the growth rate of the species, the case in which stirring is not optimal and the concentration of biomass is spatially located near the outlet line) that might cause the extinction of a species inside the vessel, especially when its concentration is very low. Obviously, this scenario will definitely terminate the multi-cellular experiment. Thus, lower bounds must be considered for the concentrations of the two species in the control problem of the bioreactor. This does not guarantee the absence of extinctions or flush-out events but reduces their probabilities. Therefore, we consider the following additional constraints:

$$\begin{matrix} x_1(t) > x_{1,\min}, \\ x_2(t) > x_{2,\min}, \end{matrix} \quad \forall t > 0. \tag{5.13}$$

In view of the above, constraints (5.12) and (5.13) limit the domain of system (5.4) to the admissible subset

$$\mathcal{D}_s \subset \mathbb{R}^3 := \{x_i(t) : x_{i,\min} < x(t) \leq s_{in}, i = 1, 2, 3\}$$

where $x_3(t) = s(t)$. Geometrically, a sketch of the situation in the space is shown in Figure 5.10.

The stabilization of system (5.4) at a generic point $(x_1, x_2, s) \in \mathcal{D}_s$ is not reasonable. Indeed, in general, the solutions of the system converge towards the invariant and attractive subset $\mathcal{S}_a$. So, starting from any initial point belonging to the subset $\mathcal{D}_s$, the solution of system (5.4) will converge to the subset $\mathcal{D}_{S,a} := \mathcal{D}_s \cap \mathcal{S}_a$, depicted in dark in Figure 5.11. The set $\mathcal{S}_a$ intersects only three edges of the domain $\mathcal{D}_s$: this can be understood by considering the fact that the surface $\mathcal{S}_a$ - in the first octant of the space - touches the plane $s = s_{in}$ only at the point $(0, 0, s_{in})$, which does not belong to the top boundary surface of the domain $\mathcal{D}_s$.

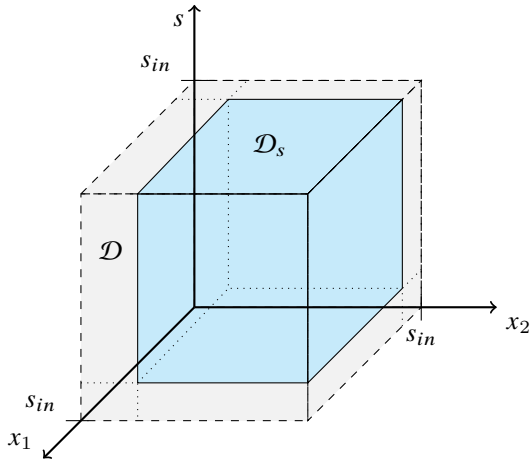

Figure 5.10: Geometrical representation of the domain $\mathcal{D}_s$ (cyan) nested in the domain $\mathcal{D}$ (gray)

5.4.1 Problem Statement

The control problem can then be stated as follows:

Design a feedback control law $D(x(t)) : \mathbb{R}^3 \to \mathbb{R}_0^+$ such that the domain $\mathcal{D}_{S,a} := \mathcal{D}_s \cap \mathcal{S}_a$ becomes forward invariant for system (5.4) and

$$\lim_{t\to\infty} \frac{x_1(t)}{x_2(t)} = r_d. \tag{5.14}$$

The last statement defines a foliation of planes that contains the line $(0, 0, s)$; when fixing r_d, we select a plane of the foliation. Figure 5.12 shows the intersection of a plane belonging to the foliation with the domain $\mathcal{D}_s$. However, the evolution of the system will converge to the subset $\mathcal{D}_{S,a}$, that can be depicted as a plane itself. The intersection of the last specification (red plane) and the subset $\mathcal{D}_{S,a}$ is our target region, that is a line as shown in Figure 5.13.

Taking into account the additional constraints (5.12)-(5.13), it is possible to notice that the intersection between the region $\mathcal{D}_s$ and the constraint on the ratio (red plane, see Figure 5.12) exists if and only if

$$\frac{x_{1,\min}}{s_{in} - x_{1,\min} - s_{\min}} < r_d < \frac{s_{in} - x_{2,\min} - s_{\min}}{x_{2,\min}} \tag{5.15}$$

In other words, this means that it is possible to regulate the ratio only within a certain range, that is bounded by some quantities that depend on the minimum values of the biomasses.

Considering that the constraints of the reduced order model (5.6) are satisfied, the control problem formulation can be represented as its phase plane showed in

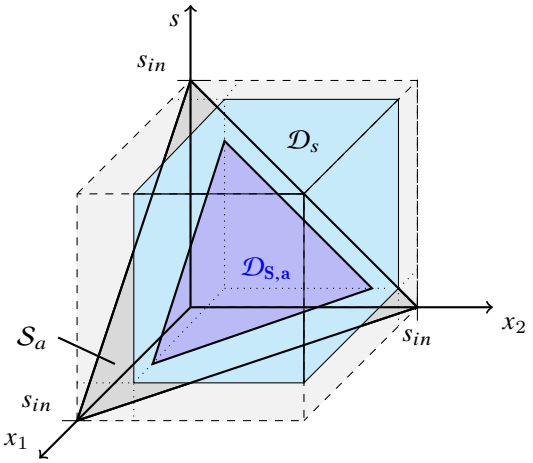

Figure 5.11: Geometrical representation of the domain $\mathcal{D}_{s,a}$ (dark blue) that is given by the intersection of the attractive and invariant subset $\mathcal{S}_a$ (dark grey) and the domain $\mathcal{D}_s$ (light blue) of the other specifications.

Figure 5.14. Specifically, the closed-loop planar system must be stabilized onto points that belong to the segment shown in green in Figure 5.14.

We further assume that the concentrations x_1 and x_2 are either directly or indirectly measurable, for example by means of fluorescent reporter proteins produced by one or both species.

5.4.2 Positions of the Closed Loop System Equilibria

Notice that the previous control problem corresponds to requiring that all the solutions of system (5.6) are stabilized at the point of intersection between the equilibrium set $\mathcal{E}$ given by (5.10), where coexistence is possible, and the line defined by (5.14); see Figure 5.15. The intersection point can be computed as:

$$x_d = [x_{d,1}, x_{d,2}]^\top = \left[\frac{s_{in} - \bar{s}}{1 + r_d}, r_d \frac{s_{in} - \bar{s}}{1 + r_d} \right]^\top . \tag{5.16}$$

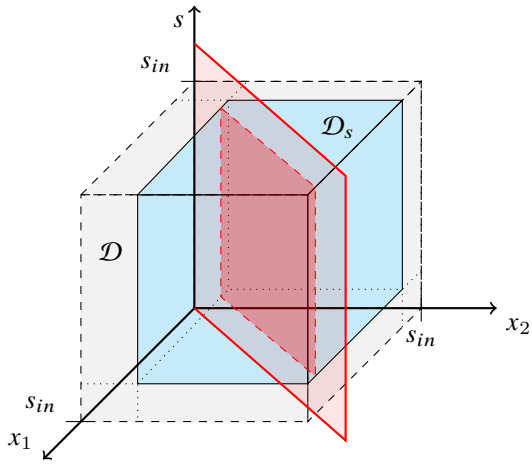

Figure 5.12: Intersection of the requirement about the ratio (red plane) and the domain of the specifications $\mathcal{D}_s$.

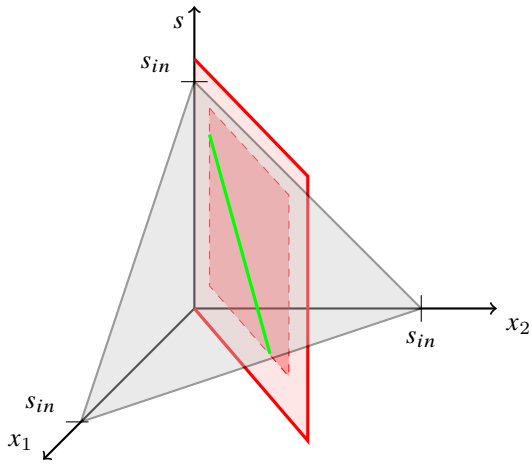

Figure 5.13: Intersection between the specification on the ratio between x_1 and x_2 (in red) and the domain of attraction $\mathcal{S}_a$ (in gray) results into a line (green).

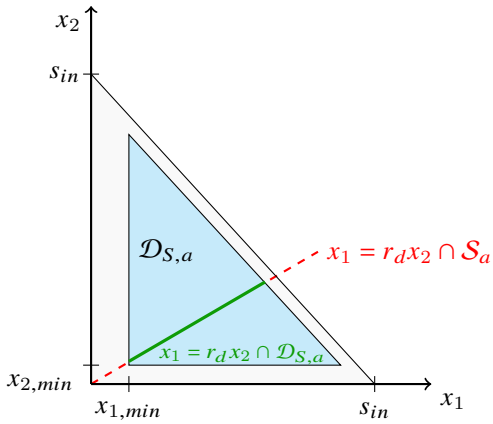

Figure 5.14: Phase plane of the system (5.6). The projection of the domain of the specification $\mathcal{D}_{S,a}$ (cyan) is contained in the projection of the domain of the system $\{(x_1, x_2, s) : x_1 + x_2 + s = s_{in}\}$ (grey). The specification on the ratio between $x_1(t)$ and $x_2(t)$ is a line (red) on the plane, with the goal region being the segment (green) that results from the intersection of the regions defined by the specification.

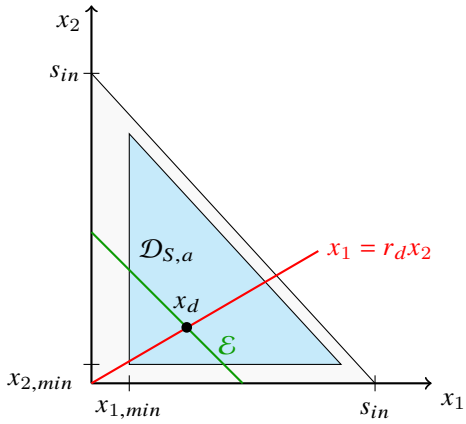

Figure 5.15: Position of the point x_d. The red line represents the points that satisfy the equation (5.14). The dark green line represents the point that belong to the equilibrium set $\mathcal{E}$ (5.10). The two lines intersect at the black dot that is the point x_d. The point x_d belongs to the domain $\mathcal{D}_{S,a}$ if the ratio r_d satisfies the inequalities (5.15).

5.5 Control Synthesis

In this section we propose two different control approaches to solve the control problem we formulated. Firstly, we design a *Gain Scheduling controller* that exploits the linearised model of system (5.6) to adapt the feedback gains of a *state feedback controller*. Secondly, we propose a *hybrid controller* that controls the system (5.6) with discontinuous inputs. Then, the two strategies are compared and their resulting dynamics discussed.

5.5.1 Linearised Model

The control problem formulated in the previous section can be addressed via a Gain Scheduling technique [86, 8]. The motivation is that of adapting the closed-loop feedback gains of a state feedback controller placing the closed-loop system's poles in a desired position. This technique eventually guarantees convergence towards the desired equilibrium $x^* = [x_1^*, x_2^*]$, whatever its position on the line defined in (5.10).

The design of a state feedback controller requires a linearised model of system (5.6) about some equilibrium $x^* = x_d$, $u^* = D_{eq}$ (where x_d is defined in (5.16) and D_{eq} in (5.9)), which is described by the following set of equations:

$$\begin{cases} \delta\dot{x} = A\delta x + B\delta u \\ \delta y = C\delta x \end{cases} \tag{5.17}$$

where δx is a variation, caused by the input δu from the equilibrium state x^*, which exists when the input u^* is applied to the system. δy is the variation of the output from y^* that is the output that the system shows when at the equilibrium x^*. The matrix A is the Jacobian J of system (5.6) evaluated at the equilibrium x^* and forced by $u^* = D_{eq}$, that is:

$$A = \begin{bmatrix} x_1 \frac{\partial \mu_1(x_1,x_2)}{\partial x_1} + \mu_1(x_1,x_2) - D_{eq} & x_1 \frac{\partial \mu_1(x_1,x_2)}{\partial x_2} \\ x_2 \frac{\partial \mu_2(x_1,x_2)}{\partial x_1} & x_2 \frac{\partial \mu_2(x_1,x_2)}{\partial x_2} + \mu_2(x_1,x_2) - D_{eq} \end{bmatrix} \Bigg|_{\substack{x_1 = x_{d,1} \\ x_2 = x_{d,2}}}$$

where

$$\begin{aligned} \frac{\partial \mu_1(x_1,x_2)}{\partial x_1} &= \frac{(\mu_1^* - 1)(s_{in} - x_1 - x_2) + k_{m,1}}{(k_{m,1} + s_{in} - x_1 - x_2)^2} \\ \frac{\partial \mu_1(x_1,x_2)}{\partial x_2} &= \frac{(\mu_1^* - 1)(s_{in} - x_1 - x_2) + k_{m,1}}{(k_{m,1} + s_{in} - x_1 - x_2)^2} \\ \frac{\partial \mu_2(x_1,x_2)}{\partial x_1} &= \frac{(\mu_2^* - 1)(s_{in} - x_1 - x_2) + k_{m,2}}{(k_{m,2} + s_{in} - x_1 - x_2)^2} \\ \frac{\partial \mu_2(x_1,x_2)}{\partial x_2} &= \frac{(\mu_2^* - 1)(s_{in} - x_1 - x_2) + k_{m,2}}{(k_{m,2} + s_{in} - x_1 - x_2)^2}. \end{aligned}$$

Using equation (5.10) matrix A becomes

$$A = \begin{bmatrix} x_1 \frac{\partial \mu_1(x_1)}{\partial x_1} + \mu_1(x_1) - D_{eq} & x_1 \frac{\partial \mu_1(x_1)}{\partial x_1} \\ (s_{in} - \tilde{s} - x_1) \frac{\partial \mu_2(x_1)}{\partial x_1} & (s_{in} - \tilde{s} - x_1) \frac{\partial \mu_2(x_1)}{\partial x_1} + \mu_2(x_1) - D_{eq} \end{bmatrix} \Bigg|_{\substack{x_1 = x_{d,1} \\ x_2 = x_{d,2}}}$$

with the partial derivatives of the growth functions being:

$$\frac{\partial \mu_1(x_1)}{\partial x_1} = \frac{(\mu_1^* - 1)\tilde{s} + k_{m,1}}{(k_{m,1} + \tilde{s})^2}$$

$$\frac{\partial \mu_2(x_1)}{\partial x_1} = \frac{(\mu_2^* - 1)\tilde{s} + k_{m,2}}{(k_{m,2} + \tilde{s})^2}.$$

The matrix B is given by:

$$B = \begin{bmatrix} \frac{\partial f_1}{\partial u} \\ \frac{\partial f_2}{\partial u} \end{bmatrix} \Bigg|_{\substack{x_1 = x_{d,1} \\ x_2 = x_{d,2}}} = \begin{bmatrix} -x_1 \\ -x_2 \end{bmatrix} \Bigg|_{\substack{x_1 = x_{d,1} \\ x_2 = x_{d,2}}}$$

Being the output of interest the state of the linearised system, matrix C is the 2×2 identity matrix.

5.5.2 Gain Scheduling

The Gain Scheduling Algorithm requires a scheduling variable that, in this case, is set equal to the desired ratio r_d. Feedback gains of a *state feedback controller* are computed as functions of this scheduling variable to guarantee that, whatever r_d is, the closed loop eigenvalues remain the same, assuring the convergence on the same timescale. The complete feedback control law is chosen as:

$$u(x_1, x_2, r_d) = D_{eq} + [K_1(r_d), K_2(r_d)] \cdot [x_{d,1} - x_1, x_{d,2} - x_2]^\top \tag{5.18}$$

where $x_d = [x_{d,1}, x_{d,2}]^\top$ is defined in (5.16).

To meet possible settling time requirements in the order of $6 \sim 7$ hours, compatible with the growth properties of the bacteria, the closed loop eigenvalues λ_1 and λ_2 are set to be in the positions $[-1, -1]$.

Even thought the problem of designing the feedback gains could be tackled analytically, the length and the complexity of the expressions makes it cumbersome; thus, the problem will be solved numerically. The first step is to design the adaptive feedback gains that solve the pole placement problem for each value of r_d in a given range. This provides values of the feedback gains K_1 and K_2 that will be interpolated later. To compute these values, it is necessary to linearise system (5.6) on the trim points belonging to the line (5.10) that satisfy the desired ratio r_d. Once this is done, via standard control techniques (Ackerman's

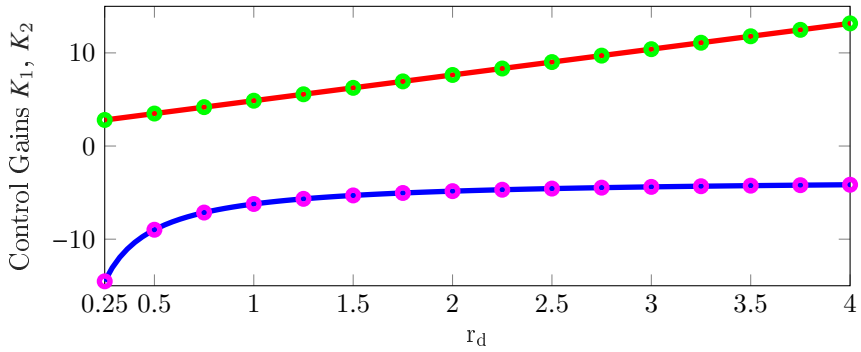

Figure 5.16: Relationship between the closed loop gains K_1 (red) and K_2 (blue) and the scheduling variable r_d. Green dots represent the evaluated values of K_1, whereas magenta dots represent the evaluated values of K_2.

formula) one can find the values of K_1 and K_2 such that the closed loop poles are in the desired position.

A possible range of values of the scheduling variable is, for example, $r_d \in [0.25, 4]$ and the corresponding values of the gains K_1 and K_2 obtained are reported as dots in Figure 5.16. Concerning the interpolation functions, a good estimation of $K_1(r_d)$ is given by the following liner approximation:

$$K_1(r_d) = a * r_d + b, \quad a = 2.7659, b = 2.1015.$$

On the other hand, the gain $K_2(r_d)$ can be approximated by the following function:

$$K_2(r_d) = b_0 + \frac{b_1}{r_d + b_2}, \quad b_0 = -3.4673, b_1 = -2.7533, b_2 = -0.0010.$$

The functions $K_1(r_d)$ and $K_2(r_d)$ are depicted in Figure 5.16.

By numerical analysis, the closed-loop dynamics was found to have four equilibrium points: a stable node in x_d, an unstable node in the origin, and two saddle points on each of the axes. Therefore, under the action of the feedback control input (5.18), all solutions converge to x_d for any initial condition $x_0 \in \mathcal{D}_{S,a}$.

Control validation

To assess the performances of the Gain Scheduling strategy, a `MATLAB` script was developed. The simulation algorithm is based on variable step integration carried-out by the `ode45` routine. We ran two simulations based on the following initial setup:

- initial condition $\mathbf{x_0} = [0.6, 0.4]^\top$;
- $D(t) \in [0.05, 2]$;

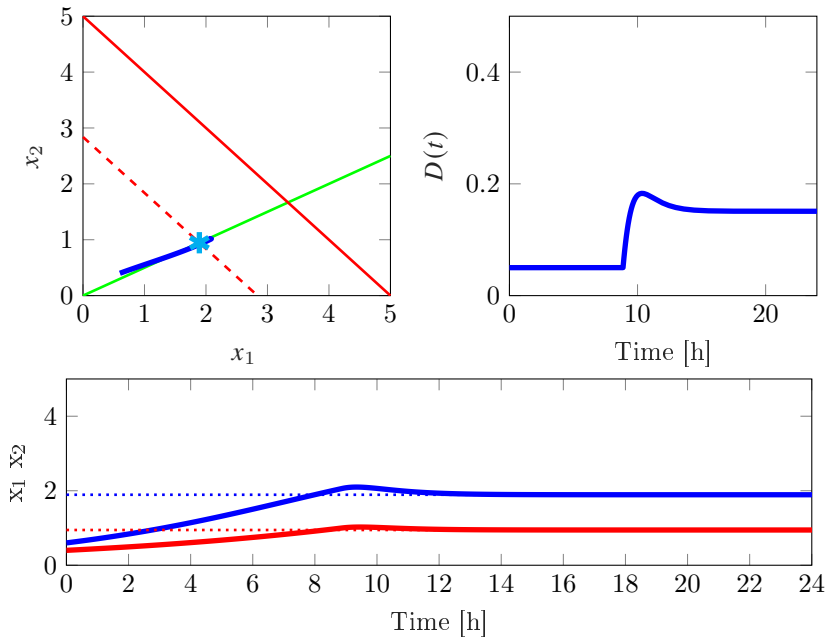

Figure 5.17: Closed loop evolution driven by the Gain Scheduling controller with setpoint $r_d = 2$ and $x_d = [1.8922, 0.9461]$. Top left: trajectories in the phase plane; the dashed red line represents the position of the equilibrium set $\mathcal{E}$ (5.10), when exists; the green line is the line that is defined by the desired ratio r_d; the cyan star is the equilibrium where the system settles. Top right: evolution of the control input $D(t)$. Bottom: Evolution of the state (x_1 in blue, x_2 in red) over time and setpoint (dotted).

- desired ratio $r_d = 2$ with a total simulation time of 24 hours;
- desired ratio $r_d = 0.5$ with a total simulation time of 48 hours.

The simulations of the closed loop evolutions are reported in Figure 5.17 and in Figure 5.18

In both cases, regulation is successfully achieved. However, for the most of the simulation, the controller waits for the biomass to grow: this results in a long initial transient, where the system is forced with a static value of the input equal to $D(t) = D_{\min} = 0.05$. Once trajectories reach a point close to the desired ratio line, the controller then starts diluting the chamber, ensuring the system converges the desired setpoint.

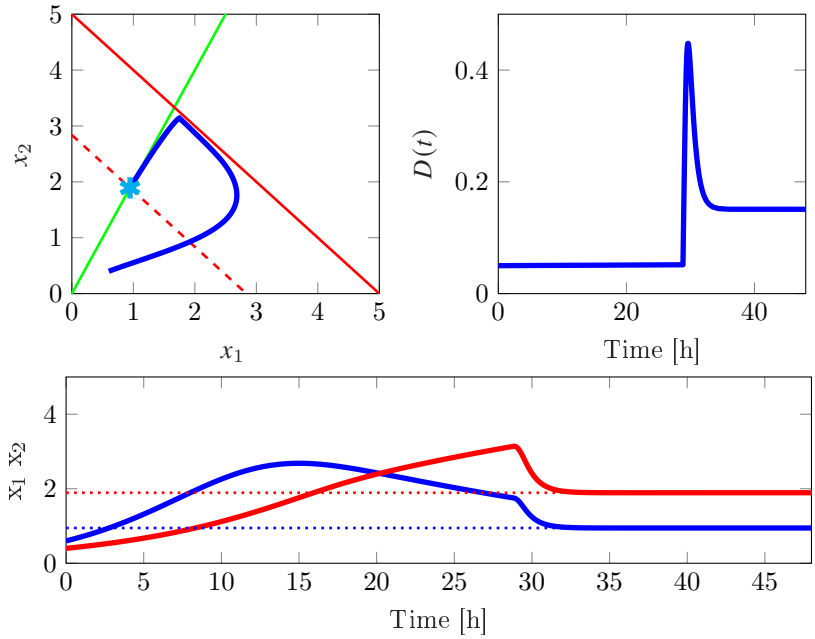

Figure 5.18: Closed loop evolution driven by the Gain Scheduling controller with setpoint $r_d = 0.5$ and $x_d = [0.9461, 1.8922]$. Top left: trajectories in the phase plane; the dashed red line represents the position of the equilibrium set $\mathcal{E}$ (5.10), when exists; the green line is the line that is defined by the desired ratio r_d; the cyan star is the equilibrium where the system settles. Top right: evolution of the control input $D(t)$. Bottom: Evolution of the state (x_1 in blue, x_2 in red) over time and setpoint (dotted).

Robustness towards parametric variation

To assess the robustness of the controller, parameter variations are introduced. In particular, as a representative example we considered a variation of 20% of the parameters of the function $\mu_1(s)$, by setting in (5.4) the new parameter values:

$$\mu_1^* = 0.6, \quad k_{m,1} = 6.$$

We tested the same scenarios presented in the previous section with the results showed in Figure 5.19 for $r_d = 2$. As it is possible to appreciate from the bottom panel, the trajectory of the system does not settle down to the setpoint. The system instead settles at a point in the equilibrium set that is at a different quota, compared to the nominal one. This results in a steady state error that has a norm equal to 0.1195 and gives a final ratio of 2.0146.

As far as the second scenario is concerned, the results of the simulations are reported in Figure 5.20. In this case, the steady state error norm is 0.1152 and

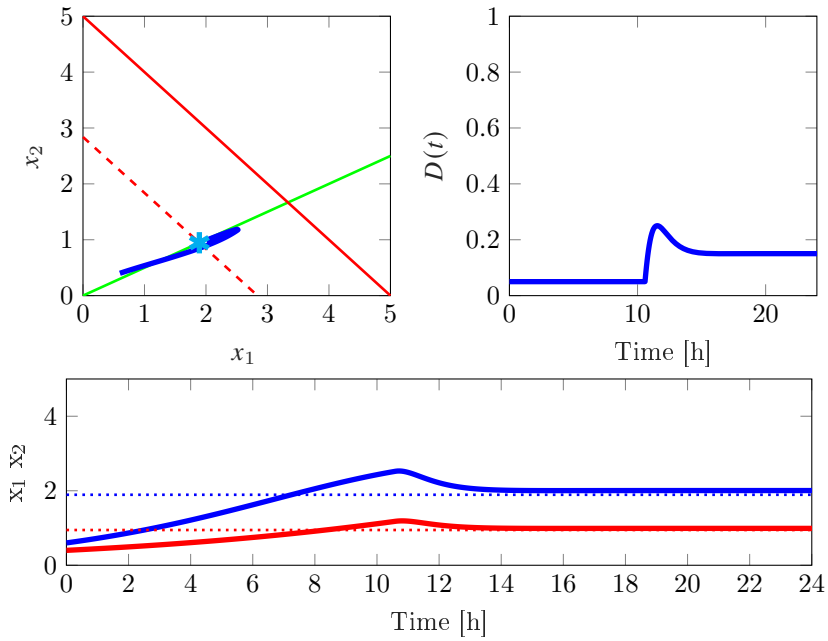

Figure 5.19: Closed loop evolution driven by the Gain Scheduling controller in presence of parametric uncertainty and setpoint $r_d = 2$. Top left: trajectories in the phase plane; the dashed red line represents the position of the equilibrium set $\mathcal{E}$ (5.10), when exists; the green line is the line that is defined by the desired ratio r_d; the cyan star is the equilibrium where the system settles. Top right: evolution of the control input $D(t)$. Bottom: Evolution of the state (x_1 in blue, x_2 in red) over time and setpoint (dotted).

the final ratio is 0.5037.

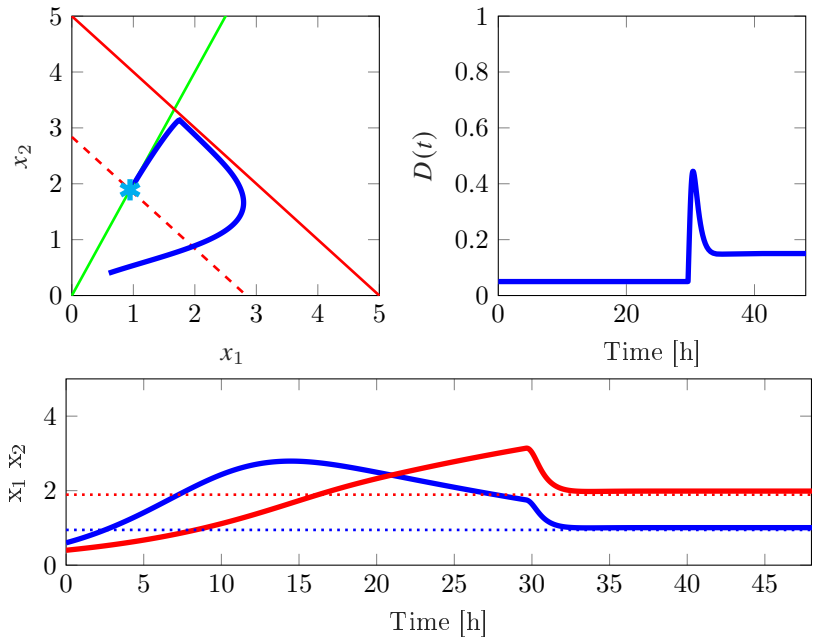

Figure 5.20: Closed loop evolution driven by the Gain Scheduling controller in presence of parametric uncertainty and setpoint $r_d = 0.5$. Top left: trajectories in the phase plane; the dashed red line represents the position of the equilibrium set $\mathcal{E}$ (5.10), when exists; the green line is the line that is defined by the desired ratio r_d; the cyan star is the equilibrium where the system settles. Top right: evolution of the control input $D(t)$. Bottom: Evolution of the state (x_1 in blue, x_2 in red) over time and setpoint (dotted).

5.5.3 Hybrid Control

In this section we move from the design of continuous control inputs to discontinuous ones. In particular, we design a hybrid control strategy.

Before moving into the design phase we first show that a switched control action can steer system (5.6) to the equilibrium set $\mathcal{E}$ (5.10) and, specifically, to the desired point x_d defined in (5.16).
Consider system (5.6) forced by the discontinuous control input:

$$D(t) = \begin{cases} d_1 & \text{if } \sigma(x_1, x_2) > 0 \\ d_2 & \text{if } \sigma(x_1, x_2) < 0 \end{cases}$$

where σ is a scalar function of the state defined as:

$$\sigma(x_1, x_2) = \alpha x_1 + x_2 - \gamma,$$

where α and γ are constants. The resulting closed loop system is described by the following vector field:

$$F(x_1, x_2) := \begin{cases} F_1(x_1, x_2) & \text{if } \sigma(x_1, x_2) > 0 \\ F_2(x_1, x_2) & \text{if } \sigma(x_1, x_2) < 0 \end{cases}$$

where the two vector fields F_1 and F_2 are expressions of model (5.6) being respectively forced by the two constant inputs d_1 and d_2. So:

$$F_1(x_1, x_2) := \begin{bmatrix} (\mu_1(x_1, x_2) - d_1)x_1 \\ (\mu_2(x_1, x_2) - d_1)x_2 \end{bmatrix}, \qquad F_2(x_1, x_2) := \begin{bmatrix} (\mu_1(x_1, x_2) - d_2)x_1 \\ (\mu_2(x_1, x_2) - d_2)x_2 \end{bmatrix},$$

having $d_1, d_2 > 0$. The smooth fields F_1 and F_2 are separated by a switching surface Σ, defined as the zero-set of the scalar function σ.
The existence of sliding motion onto the surface Σ can be verified checking the Lie derivatives of the function σ with respect to F_1 and F_2. In particular, it must be $L_{F_1}(\sigma)|_{\sigma=0} < 0$ and $L_{F_2}(\sigma)|_{\sigma=0} > 0$. So, recalling that, when $\sigma = 0$, $x_2 = \gamma - \alpha x_1$, we obtain the following conditions:

$$\begin{gathered} L_{F_1}(\sigma)|_{\sigma=0} = [\nabla\sigma \cdot F_1]\,|_{\sigma=0} = \\ = [\alpha(\mu_1(x_1, x_2) - d_1)x_1 + (\mu_2(x_1, x_2) - d_1)x_2]\,|_{\sigma=0} < 0 \Rightarrow \\ \Rightarrow \gamma d_1 > \alpha\mu_1(x_1, x_2)x_1 + \mu_2(x_1, x_2)x_2 = \alpha(\mu_1(x_1, \alpha, \gamma) - \mu_2(x_1, \alpha, \gamma))x_1 + \gamma\mu_2(x_1, \alpha, \gamma) \end{gathered}$$

$$\begin{gathered} L_{F_2}(\sigma)|_{\sigma=0} = [\nabla\sigma \cdot F_2]\,|_{\sigma=0} = \\ = [\alpha(\mu_1(x_1, x_2) - d_2)x_1 + (\mu_2(x_1, x_2) - d_2)x_2]\,|_{\sigma=0} > 0 \Rightarrow \\ \Rightarrow \gamma d_2 < \alpha\mu_1(x_1, x_2)x_1 + \mu_2(x_1, x_2)x_2 = \alpha(\mu_1(x_1, \alpha, \gamma) - \mu_2(x_1, \alpha, \gamma))x_1 + \gamma\mu_2(x_1, \alpha, \gamma) \end{gathered} \tag{5.19}$$

Introducing the following quantity

$$d_s(x_1, \alpha, \gamma) := \alpha(\mu_1(x_1, \alpha, \gamma) - \mu_2(x_1, \alpha, \gamma))x_1 + \gamma\mu_2(x_1, \alpha, \gamma),$$

the following condition must be satisfied to have sliding on the switching surface:

$$\gamma d_2 < d_s(x_1, \alpha, \gamma) < \gamma d_1. \tag{5.20}$$

The sliding dynamics will be governed by the sliding vector field F_s. Let us compute this field with the aim of studying its equilibria. Consider the following vector field as difference of F_1 and F_2

$$F_2 - F_1 = \begin{bmatrix} (d_1 - d_2)x_1 \\ (d_1 - d_2)x_2 \end{bmatrix}$$

and the Lie derivative of σ with respect to it on the surface Σ, that is

$$L_{F_2-F_1}(\sigma)|_{\sigma=0} = \alpha(d_1 - d_2)x_1 + (d_1 - d_2)(\gamma - \alpha x_1) = (d_1 - d_2)\gamma.$$

The sliding vector field F_s can be computed as

$$F_s = F_2|_{\sigma=0} + \lambda(F_2 - F_1)|_{\sigma=0}, \qquad \lambda = -\frac{L_{F_2}(\sigma)}{L_{F_2-F_1}(\sigma)}, \lambda \in [-1, 0]$$

$$\lambda = -\frac{\alpha(\mu_1(x_1, \alpha, \gamma) - \mu_2(x_1, \alpha, \gamma))x_1 + \gamma(\mu_2(x_1, x_2) - d_2)}{\gamma(d_1 - d_2)} = -\frac{d_s(x_1, \alpha, \gamma) - \gamma d_2}{\gamma(d_1 - d_2)}$$

$$\Rightarrow F_s = \begin{bmatrix} (\mu_1(x_1, x_2) - d_2)x_1 \\ (\mu_2(x_1, x_2) - d_2)x_2 \end{bmatrix}\Bigg|_{\sigma=0} + \lambda \begin{bmatrix} (d_1 - d_2)x_1 \\ (d_1 - d_2)x_2 \end{bmatrix}\Bigg|_{\sigma=0}$$

Finally, the sliding vector field F_s is given by:

$$F_s = \begin{bmatrix} (\mu_1(x_1, \alpha, \gamma) - d_s(x_1, \alpha, \gamma)\gamma^{-1})x_1 \\ (\mu_2(x_1, \alpha, \gamma) - d_s(x_1, \alpha, \gamma)\gamma^{-1})(\gamma - \alpha x_1) \end{bmatrix}$$

This system has four equilibrium points, namely:

1. an unstable node in $(0, 0)$,
2. an equilibrium in $(0, \gamma)$,
3. an equilibrium in $(-\gamma/\alpha, 0)$,
4. an equilibrium at the point of intersection of Σ and $\mathcal{E}$ (5.16) when $d_s(x_1, \alpha, \gamma)/\gamma = \mu_1(x_1, \alpha, \gamma) = \mu_2(x_1, \alpha, \gamma) = D_{eq}$.

Therefore, using (5.20) we have a necessary condition for x_d to be a pseudo-equilibrium point of F_s, that is

$$\gamma d_2 < \gamma D_{eq} < \gamma d_1. \tag{5.21}$$

Thus, the desired point is a pseudo-equilibrium of the sliding dynamics only if $\gamma > 0$.

By analysing the vector field F_s in the neighbourhood of the equilibrium $(0, \gamma)$ it is possible to classify the point as a stable node for $\gamma > s_{in} - \tilde{s}$ and a saddle

in the complementary case $\gamma > s_{in} - \tilde{s}$. The same analysis holds for $(-\gamma/\alpha, 0)$. Therefore, it follows that the equilibrium point x_d is stable if

$$0 < \gamma < s_{in} - \tilde{s}.$$

The point x_d loses its stability when $\gamma = s_{in} - \tilde{s}$ via a *degenerate transcritical bifurcation.*

□

Note that, since the sliding vector field vanishes only on $\mathcal{E}$, setting a desired ratio r_d between the two species links the parameters α and γ defining the sliding region via the expression:

$$\alpha = r_d - \gamma/x_{1,d},$$

where $x_{d,1}$ is the abscissa of x_d as defined in (5.16).

Control Validation

To assess the performances of this hybrid controller, a simulation algorithm in `Stateflow` was developed. Consider the following initial setup of the simulation:

- initial condition $\mathbf{x_0} = [0.6, 0.4]^\top$;
- total simulation time 108 hours;
- $D(t)$ can continuously vary in the range $[0.05, 2]$, saturating to the minimum or to the maximum value;
- desired ratio $r_d = 2$ and $r_d = 0.5$.

In the simulations, γ was chosen in order to intersect the equilibrium set $\mathcal{E}$ in the desired equilibrium x_d defined in (5.16).

The performance of the hybrid control strategy are reported in Figure 5.21 and in Figure 5.22 for two different values of r_d.

Robustness to parameter variation

As before, we consider a variation of 20% of the parameters of the function $\mu_1(s)$ in model (5.4). Specifically, we set:

$$\mu_1^* = 0.6, \quad k_{m,1} = 6$$

and repeated same scenario presented earlier, obtaining the dynamics shown in Figure 5.23 for the ratio $r_d = 2$. As it is possible to appreciate from the bottom panel, the trajectory of the system does not settle down to the setpoint. The system settles onto a point of an equilibrium set that is at a different quota, compared to the nominal one. This results into a steady state error that, in norm, is equal to 0.1174, with a final ratio of 2.0011 that guarantees a slight regulation improvement with respect to the Gain Scheduling technique.

For the second scenario, the results of the simulations are reported in Figure 5.24. In this case, the steady state error norm is 0.1171 with a final ratio of 0.5001.

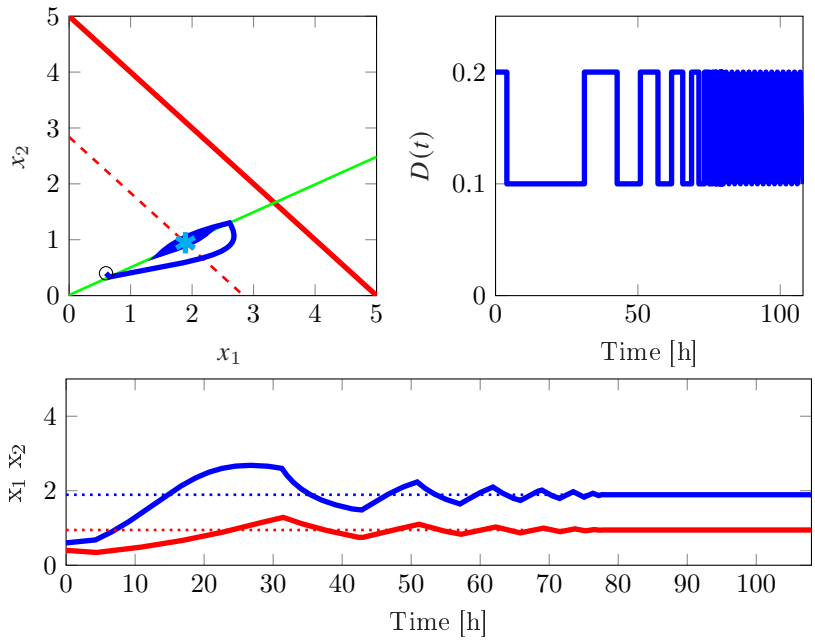

Figure 5.21: Closed loop evolution of the system driven by the hybrid controller when $r_d = 2$, $x_d = [1.8922, 0.9461]$, $\alpha = -0.5053$, and $\gamma = -0.10$. Top left: trajectories in the phase plane; the dashed red line represents the position of the equilibrium set $\mathcal{E}$ (5.10), when exists; the green line is the line that is defined by the ratio; the cyan star is the equilibrium where the system settles. Top right: evolution of the control input $D(t)$. Bottom: Evolution of the state (x_1 in blue, x_2 in red) over time and setpoint (dotted).

5.5.4 Advantages and Limitations

Despite the effectiveness of the above presented control strategies, the single chamber bioreactor shows several limitations. It is indeed possible to regulate the ratio only onto points of line given by (5.10), which is problematic when the ratio is very small or very large. Indeed, in these situations, the closed loop equilibrium will correspond to a small value of one of the two biomass concentrations and will not be robust towards possible flush-out events. Moreover, the regulation experiments require a timescale that is quite long for a standard *in vivo* experiment; over these long time periods, mutations are likely to occur leading to the failure of the experiment. Last but not least, uncertainties of the parameters and the growth functions – or other stochastic effects on the growth properties of the living bacteria – lead to steady state errors that cannot be compensated for, by any of the proposed control strategies.

Therefore, there is the need of alternative bioreactor layouts to overcome these

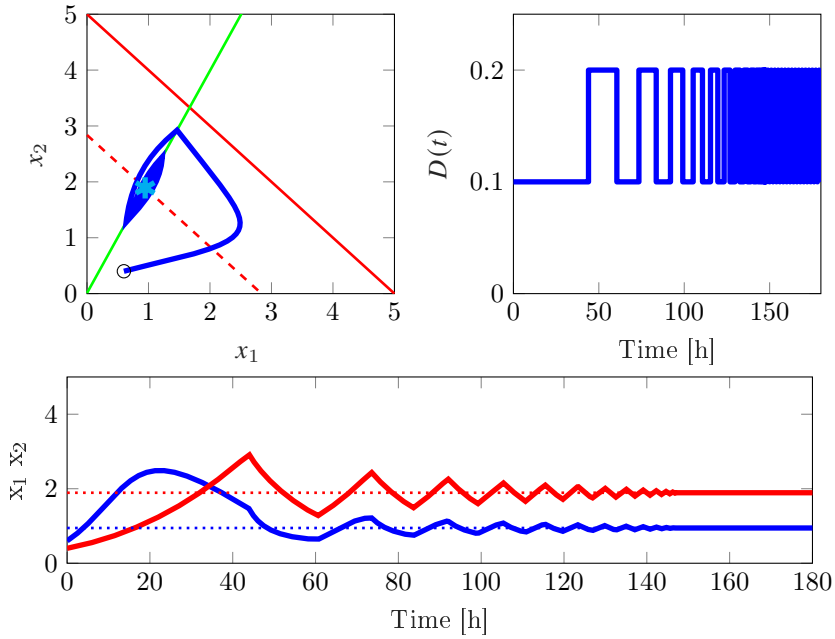

Figure 5.22: Closed loop evolution of the system driven by the Hybrid controller when $r_d = 0.5$, $x_d = 0.9461, 1.8992$, $\alpha = -2.0106$, and $\gamma = -0.01$. Top left: trajectories in the phase plane; the dashed red line represents the position of the equilibrium set $\mathcal{E}$ (5.10), when exists; the green line is the line that is defined by the ratio; the cyan star is the equilibrium where the system settles. Top right: evolution of the control input $D(t)$. Bottom: Evolution of the state (x_1 in blue, x_2 in red) over time and setpoint (dotted).

limitations, allowing fast and robust regulation of the different biomasses.

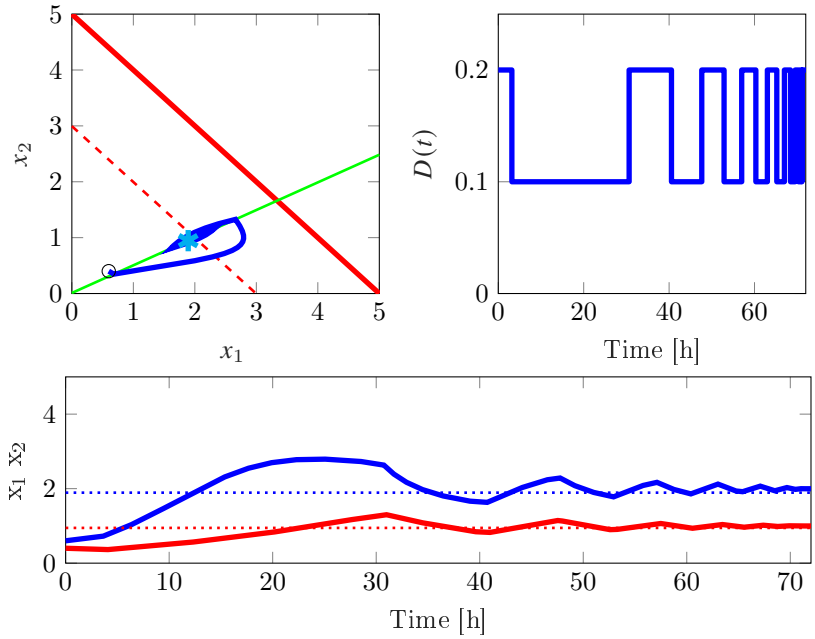

Figure 5.23: Closed loop evolution of the system driven by the Hybrid controller when $r_d = 2$, $x_d = [1.8922, 0.9461]$, $\alpha = -0.5053$, and $\gamma = -0.10$, in presence of parametric variations. Top left: trajectories in the phase plane; the dashed red line represents the position of the equilibrium set $\mathcal{E}$ (5.10), when exists; the green line is the line that is defined by the ratio; the cyan star is the equilibrium where the system settles. Top right: evolution of the control input $D(t)$. Bottom: Evolution of the state (x_1 in blue, x_2 in red) over time and setpoint (dotted).

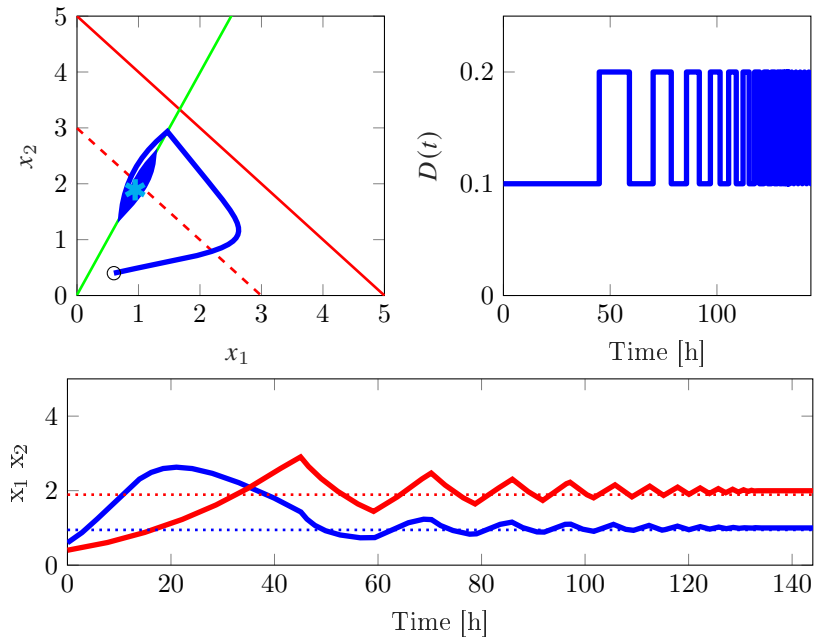

Figure 5.24: Closed loop evolution of the system driven by the Hybrid controller when $r_d = 0.5$, $x_d = 0.9461, 1.8992$, $\alpha = -2.0106$, and $\gamma = -0.01$, in presence of parametric variations. Top left: trajectories in the phase plane; the dashed red line represents the position of the equilibrium set $\mathcal{E}$ (5.10), when exists; the green line is the line that is defined by the ratio; the cyan star is the equilibrium where the system settles. Top right: evolution of the control input $D(t)$. Bottom: Evolution of the state (x_1 in blue, x_2 in red) over time and setpoint (dotted).

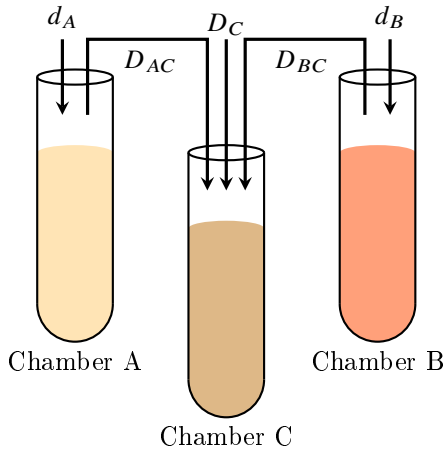

Figure 5.25: Sketch of the design of a bioreactor with three chambers. Chambers A and Chamber B are "growth chambers" with a single population on the inside. Chamber C is a mixing chambers.

5.6 Preliminary Results on a Three Chamber Bioreactor

In the remainder of this Chapter, we propose a 3-chamber bioreactor design, together with its mathematical model and a control strategy that guarantees coexistence of two competing bacterial species overcoming the limitations shown by the single chamber bioreactor in the previous section. We will test the effectiveness of the new layout and of the control strategy via *in-silico* experiments.

5.6.1 Mathematical Model

Consider the three chamber design depicted in Figure 5.25. The mathematical model of this machine can be described by the following set of equations:

$$\begin{cases} \dot{x}_A = (\mu_A(x_A, s_A) - d_A(t) - D_{AC}(t))x_A \\ \dot{s}_A = -\mu_A(x_A, s_A)x_A + (d_A(t) + D_{AC}(t))(s_{in,A} - s_A) - D_{AC}(t)s_A \\ \dot{x}_B = (\mu_B(x_B, s_B) - d_B(t) - D_{BC}(t))x_B \\ \dot{s}_B = -\mu_B(x_B, s_B)x_B + (d_B(t) + D_{BC}(t))(s_{in,B} - s_B) - D_{BC}(t)s_B \\ \dot{x}_{AC} = (\mu_A(x_{AC}, s_C) - D_{tot}(t))x_{AC} + D_{AC}(t)x_A \\ \dot{x}_{BC} = (\mu_B(x_{BC}, s_C) - D_{tot}(t))x_{BC} + D_{BC}(t)x_B \\ \dot{s}_C = -\mu_A(x_{AC}, s_C)x_{AC} - \mu_B(x_{BC}, s_C)x_{BC} + \Delta(t) \end{cases} \tag{5.22}$$

where

$$D_{tot}(t) = D_C(t) + D_{AC}(t) + D_{BC}(t)$$

and

$$\Delta(t) = D_C(t)(s_{in,C} - s_C) + D_{AC}(t)(s_A - s_C) + D_{BC}(t)(s_B - s_C)$$

In the above equations, x_A, s_A are respectively the concentrations of biomass and substrate in the growth chamber A; analogously x_B, s_B are biomass and substrate concentration in the growth chamber B. x_{AC}, x_{BC}, s_C are the concentrations of bio-masses (of the species A and B) and the substrate concentration in the mixed chamber C, where the experiment takes place. The generic growth rate function $\mu(\cdot)$ depends on biomass and substrate values. The terms $s_{in,A}$, $s_{in,B}$ and $s_{in,C}$ represent the concentrations of substrate in the bottles that feed respectively the chambers A, B and C. The term $d_A(t) + D_{AC}(t)$ is the growth chamber A dilution rate, while $d_B(t) + D_{BC}(t)$ is the analogous for the chamber B; $D_C(t)$ is the dilution rate of the mixed chamber, coming from a bottle of substrate with no biomass; $D_{AC}(t)$ and $D_{BC}(t)$ are the ratios between flows coming from the growth chambers A and B and the total volume of the mixed chamber. In the derivation of the model, the following assumptions have been made:

A1. Well Stirred Reactors - The content of each chamber is assumed to be in a completely mixed condition: the composition of the medium is homogeneous in the reactor. Spatial effects of diffusion are neglected. The Reactor is assumed to work under continuous substrate feeding and constant working volume.

A2. The dynamical behaviour of the growth of one population of microorganisms depends on a single limiting substrate in a stirred tank reactor.

A3. The biomass growth and the substrate consumption terms relative to a certain species are proportional to the biomass concentrations x_i $(i = A, B, AC, BC)$ of the same species.

A4. The decay term of the biomass is neglected. Death occurs when cells are flushed out because of dilution.

A5. The growth rates μ. depend on the species concentration and the substrate in the same chamber. Other factors that may influence the growth are neglected.

A6. The three chambers have the same working volume, so that the proportionality factor between the dilution rates is 1.

A7. The three chambers are fed by the same bottle of media, so that the concentration of substrate coming from it is the same. In particular, $s_{in,A} = s_{in,B} = s_{in,C} = s_{in}$.

A8. The total dilution rate of the mixed chamber is the sum of three terms, as in the above equation. D_C is referred to a flow coming from a bottle of media with no biomass and substrate concentration s_{in}; D_{AC} is referred to the flow coming from the growth chamber A, having concentration of biomass equal to x_A and concentration of substrate equal to s_A; D_{BC} is referred to the flow coming from the growth chamber B, having concentration of biomass equal to x_B and concentration of substrate equal to s_B.

A9. The outflow that goes from the growth chambers to the mixed one is replaced by fresh media, to keep the volume constant. So there is an additional term of substrate addition $D(s_{in} - s_i)$, $i = \{A, B\}$ in the growth chambers equations.

5.6.2 Control Problem

Analogously to the Single-Chamber design, it is possible to define a subdomain $\mathcal{B}$ as a domain where the same robustness constraints are solved. Therefore, since the experiment happens in the chamber C,

$$\mathcal{B} := \{\chi_i : \ \chi_{i,min} < \chi_i < \chi_{i,max}, \ \chi_i = \{x_{AC}, x_{BC}, s_C\}\}.$$

Given the vector of inputs $D(t) = [d_A(t), d_B(t), D_{AC}(t), D_{BC}(t), D_C(t)]$, design a feedback control law $D(x(t)) : \mathbb{R}^7_+ \to \mathbb{R}^5_+$ such that the domain $\mathcal{B}$ is forward invariant for the system (5.22) and

$$\lim_{t\to\infty} \frac{x_{AC}(t)}{x_{BC}(t)} = r_d.$$

Control Design

To deal with the problem formulated above, we designed a controller made up of different actions. Here we define the error on the ratio as

$$e_r(t) = r_d - \frac{x_{AC}(t)}{x_{BC}(t)}.$$

To regulate the ratio in the mixed chamber, we tuned two PI controllers to regulate the inputs D_{AC} and D_{BC} as:

$$\begin{cases} D_{AC}(t) = k_{P,AC} e_r(t) + k_{I,AC} \int_0^t e_r(\tau) d\tau \\ D_{BC}(t) = k_{P,BC} e_r(t) + k_{I,BC} \int_0^t e_r(\tau) d\tau. \end{cases} \tag{5.23}$$

To avoid low values of the substrate in the mixed chamber, we regulated the other input, D_C, as

$$D_C(t) = k_s(\bar{s}_m - s_m(t)), \tag{5.24}$$

where $\bar{s}_m$ is a threshold value and the input $D_C \in [0,\ D_{C,\max}]$.
Two PI controllers regulate the additional dilution rates d_A and d_B as:

$$\begin{cases} d_A(t) = k_{P,A}(s_A(t) - \bar{s}_A) + k_{I,A} \int_0^t (s_A(\tau) - \bar{s}_A) d\tau \\ d_B(t) = k_{P,B}(s_B(t) - \bar{s}_B) + k_{I,B} \int_0^t (s_B(\tau) - \bar{s}_B) d\tau, \end{cases} \tag{5.25}$$

where $\bar{s}_A$ and $\bar{s}_B$ are two fixed values of the substrate in the growth chamber. This is done to guarantee a sufficiently high growth rates of the two species, minimizing the risk of biomass flush-out from the growth chambers.

5.6.3 In-Silico Experiments

We conducted *in-silico* experiments to assess the performance of the proposed control strategy. The initial conditions of the system were as follows:

- $x_A = 3$, $s_A = 2$,
- $x_B = 3$, $s_B = 2$,
- $x_{AC} = 1$, $x_{BC} = 3$, $s_C = 1$.

In the following experiments, we empirically tuned the controllers gains to be:

- The PI gains for the inputs D_{AC} and D_{BC} in equation (5.23) are $k_{P,AC} = 3$, $k_{I,AC} = 0.1$, $k_{P,BC} = -3$, $k_{I,BC} = -0.1$;
- The gain chamber C substrate controller defined in (5.24) is $k_s = 0.5$, with $\bar{s}_m = 1$ and the saturation value $D_{C,\max} = 1$;
- The PI gains for the inputs d_A and d_B in equation (5.25) are $k_{P,A} = 1$, $k_{I,A} = 0.01$, $k_{P,B} = 1$, $k_{I,B} = 0.01$, with $\bar{s}_A = \bar{s}_B = 2$.

The duration of the control experiments have been set to 24 hours. In the first experiment, the desired ratio in the mixed chamber is $r_d = 2$. Numerical results

are shown in Figure 5.26. In this case, the ratio becomes equal to the setpoint after approximately 3 hours.

The second experiment sets the desired ratio in the mixed chamber to $r_d = 0.5$. Numerical results are shown in Figure 5.27. Also in this case, the ratio becomes equal to the setpoint after approximately 4 hours.

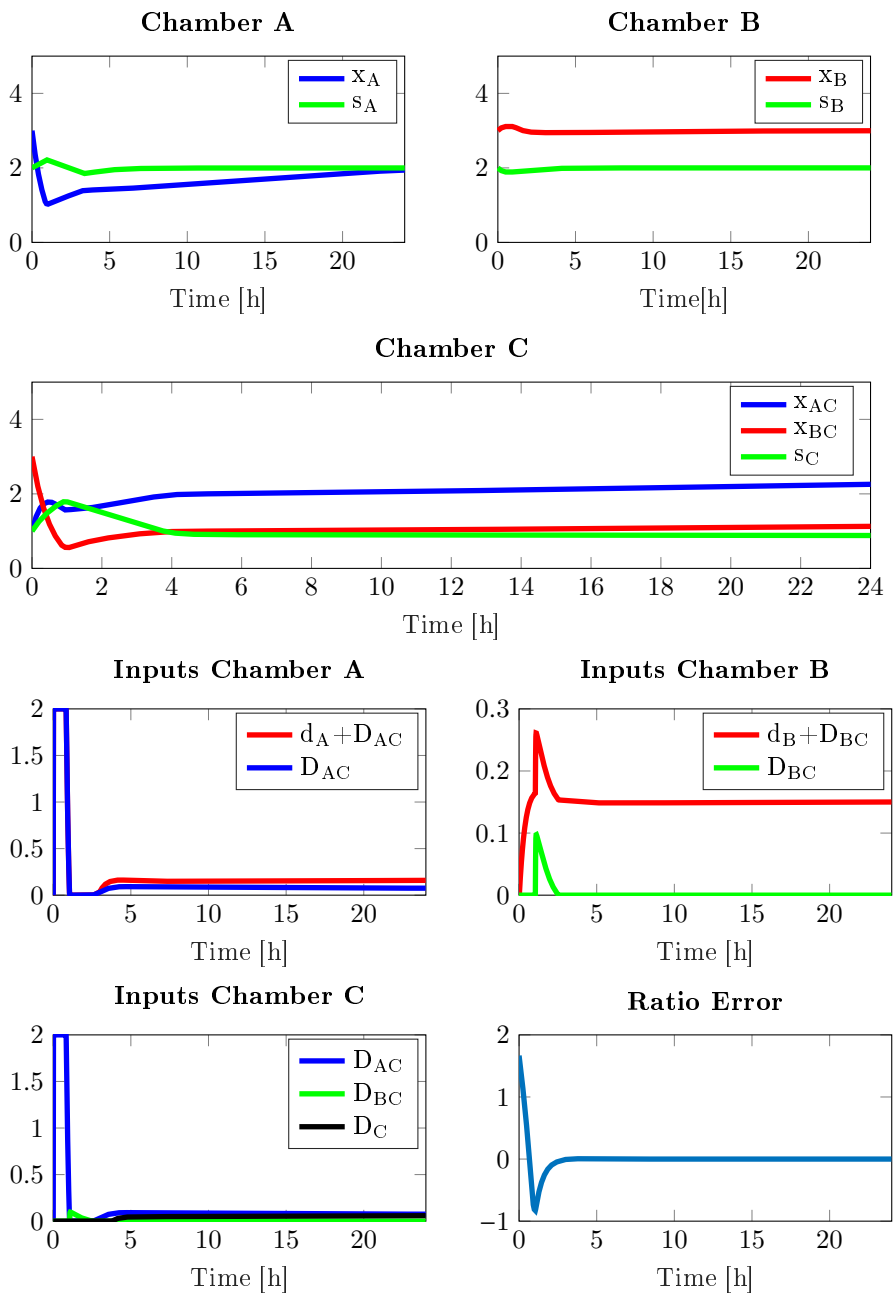

Figure 5.26: Numerical results of the control strategy. Each panel shows the evolution over time of the quantities reported in legends.

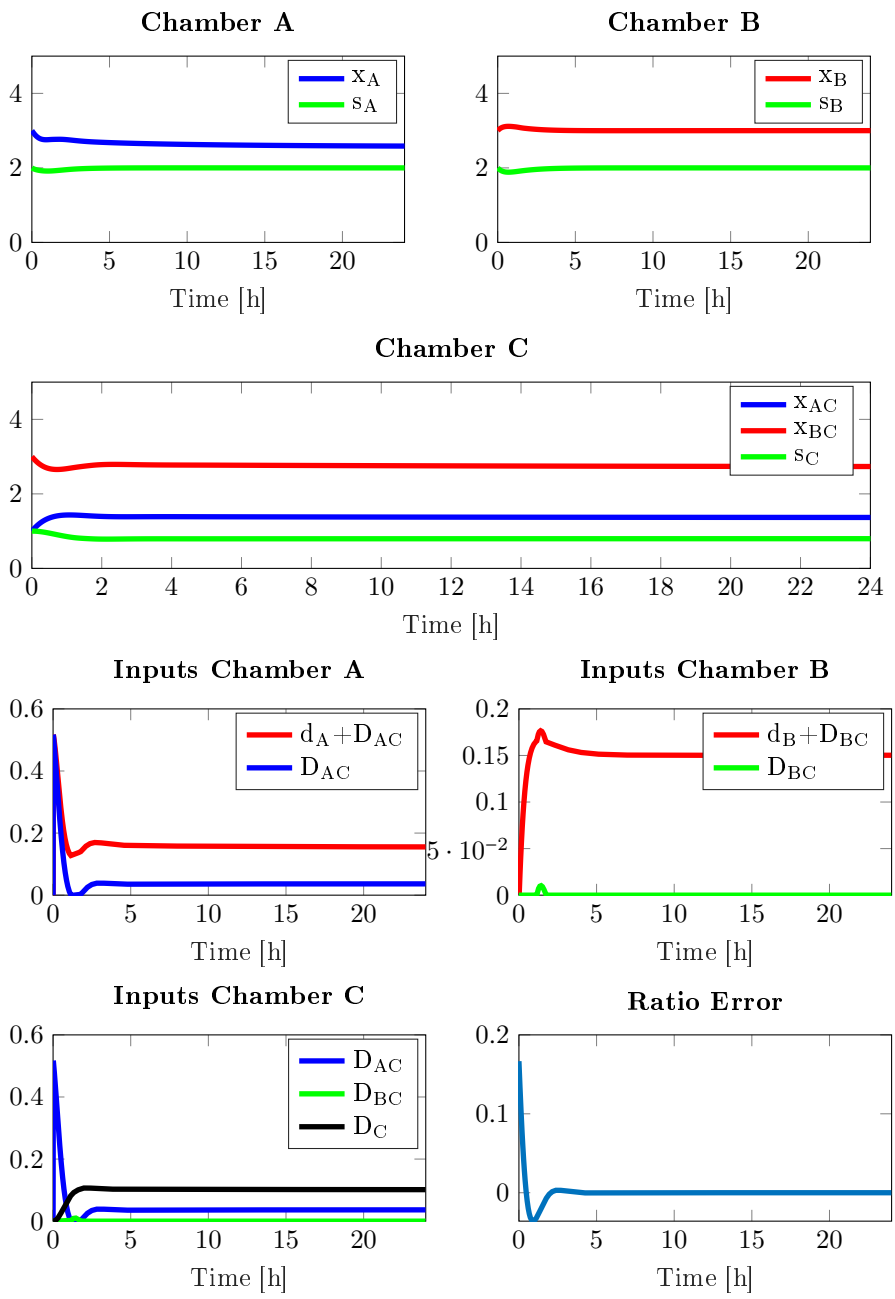

Figure 5.27: Numerical results of the control strategy. Each panel shows the evolution over time of the quantities reported in legends.

Robustness to parameter variation

Being controlled by PI controllers with no information about the model of the plant, any variation in the parameters of the growth functions do not reflect in any change of the closed loop equilibrium. We repeated the simulations presented in the previous section, under the same perturbations considered for the previous layout. In both cases, $r_d = 2$ reported in Figure 5.28 and $r_d = 0.5$ reported in Figure 5.29, the error on the ratio goes to 0, assuring perfect regulation.

5.7 Discussion

In this Chapter, after motivating the importance of designing a control strategy for a bioreactor such that two cell populations can coexist in a stable manner, we presented and analysed two possible designs for multicellular bioreactors. The first design presented can exhibit long timescales of the experiments, that span the range of days, and lack of robustness towards parameter variations. The second multi-chamber design, conversely, has a more complex structure that guarantees the satisfaction of the control problem with ease. A strategy based on PI controllers has been numerically shown to be effective to regulate of the ratio between the two populations. Further improvements can involve a more precise tuning of the control gains and the study of alternative control strategies.

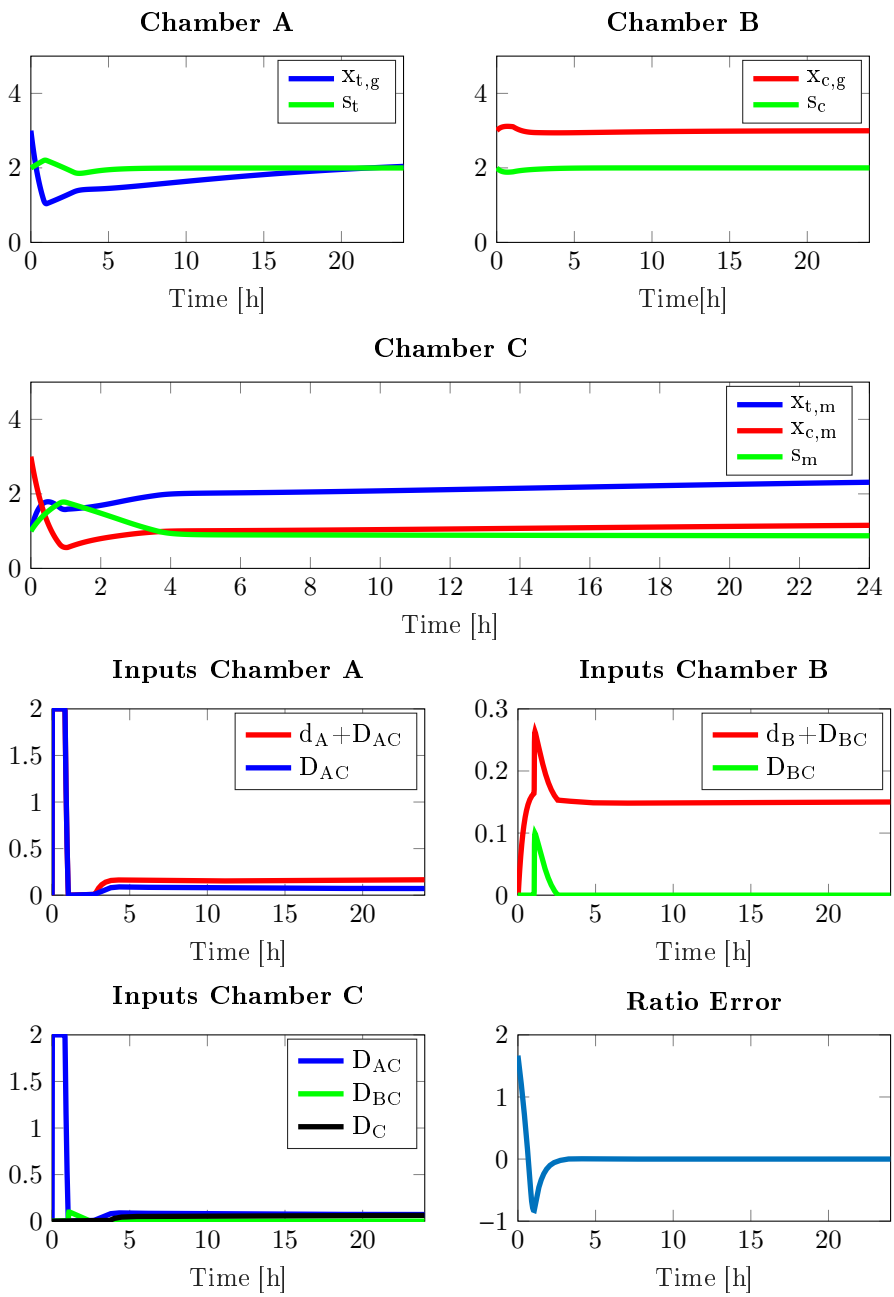

Figure 5.28: Numerical results of the control strategy. Each panel shows the evolution over time of the quantities reported in legends.

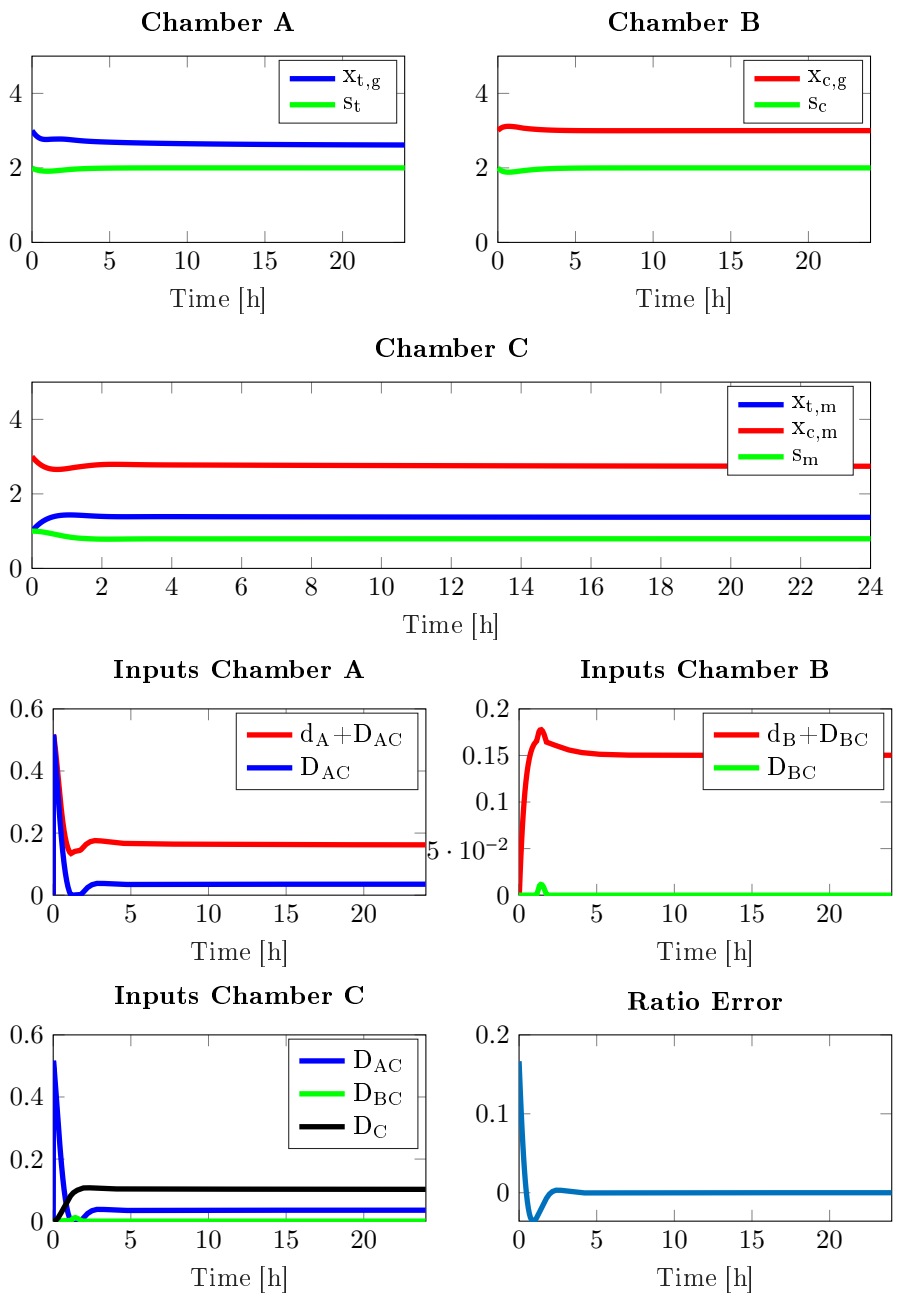

Figure 5.29: Numerical results of the control strategy. Each panel shows the evolution over time of the quantities reported in legends.

6 Conclusions

In this thesis, we explored different strategies for the analysis and control of bacterial populations.

In the first part of the thesis we addressed the challenging problem of balancing a genetic toggle switch in the surroundings of its unstable equilibrium point via external (*in silico*) control actions. We presented two closed-loop feedback strategies, PIPWM and MPC, for the regulation of the features of mutually exclusive pulse wave inputs. We showed that both the strategies are effective and satisfy the control goal, even in the presence of *hard non-linearities* introduced by the cell membrane, validating the results via agent-based simulations in BSim [55]. Then, we compared the two proposed strategies with an Open-Loop control that has been proved to be effective in the stabilization of a population during *in vivo* experiments. By evaluating some aggregate control indexes, we quantified the performance improvement that justify the adoption of closed-loop strategies.

An open problem concerns the implementation of these strategies *in vivo*. From our *in silico* experiments, it follows that, in general, MPC leads to better regulation than using PIPWM, however PIPWM has a simpler implementation and a lower computational load. Indeed, the implementation of the MPC controller requires the solution of an optimization problem via a genetic algorithm, requiring the algorithm to be run on a *high-end* computer to avoid excessive delays in the control loop. Conversely, the PIPWM requires light-weighted algebraic computations that can be performed by cheaper microcontrollers, significantly simplifying the architecture of devices required to implement the control strategies.

In the second part of the thesis, we moved from the problem of achieving the *phenotypic* control of a cell population to the problem of controlling its growth. We proposed an open-source, modular and versatile turbidostat that can be easily assembled. The device we designed can be built with a very small budget of less than $200, assuming access to free 3D printing services. Although the presented design is very basic, its Arduino-based structure is very flexible and allows new functionalities to be easily added, such as the actuation of LEDs for optogenetics experiments or the insertion of a simple fluorescence measurement circuit.

Then, we analysed the problem of controlling the ratio of two cell populations in a chemostat to guarantee their coexistence. The motivation behind this

comes from the idea of adapting the turbidostat we designed to host multicellular *in vivo* experiments, with two competing populations fed by the same limiting nutrient source in the same environment. We described the rich dynamics that the system can show and we addressed the problem of designing control strategies that guarantee species survival while regulating their ratio. Our *in silico* experiments, however, showed some peculiar aspects of this simple solution that limit the control performance, leading to long and unsustainable settling times and poor rejection of model uncertainties. Therefore, in Chapter 5 we presented a new 3-chambers layout that can overcome the above issues. Under some realistic assumptions, we derived a mathematical model for this architecture and designed a simple MIMO control strategy that is capable of guaranteeing species survival in the experimental chamber, while perfectly regulating the ratio of the two populations.

The evaluation of the concentration of two species mixed in the same chamber is, probably, the most interesting problem to be faced during the implementation of the presented 3-chambers design. Theoretically, the turbidostat designed in Chapter 4 could be extended and rearranged to implement this design, using peristaltic pumps to deliver flow from the growth chambers to the mixing one. However, the above mentioned problem still undermine its realization. Further studies could be aimed at solving this practical problems. A possible solution could be that of bonding different fluorescence proteins to the two populations and designing effective fluorescence measurement circuits to perform the measures. However, we believe that the presented 3-chambers layout is a valuable solution to perform *large-scale* multicellular *in vivo* control experiments.

A Further Details about the Turbidostat Design

Part List

The list of all the parts needed to assemble the turbidostat discussed in Chapter 4 is reported in Table A.1. The list does not include other necessary parts such as connection jumpers, connection pins, screws and glue that can be commonly found in each workshop.

3D printable parts can be found at https://github.com/diBernardoGroup/Turbidostat/tree/master/3D%20Printed%20Parts/STL%20files

Electronics

In this section we report the electronics diagrams of the prototype of turbidostat we assembled. Figure A.1 shows a sketch of how each module is connected to the main Arduino board. Figure A.2 shows in details the connections between the functional modules that compose the electronic diagram.

Q.ty	Name	Description
1	Arduino Mega 2560 Rev3	Main control Board
1	9V Power supply	Main board power supply
1	Adafruit Motor Shield v3	Motor Driver Board
1	12V Power supply	Motor driver board power supply
1	Silent acquarium pump	Air Pump
1	OSRAM SHF 4544	LED at 950nm
1	Vishay Semi-conductors BP104	Photodiode with 950nm pin-hole filter
1	220Ω Resistor	Used in the optical circuit
1	$10k\Omega$ Potentiometer	Tunable resistor for the calibration
1	6-wire Stepper Motor	To drive the peristaltic pump
2	Standard Servo (180°)	To drive syringe pump and pinch valve
1	Set of Plastic Gears	For syringe pump and pinch valve
1	DC Motor	To stir the solution
2	Magnets N50	To mount on the stirring support
1	Magnetic stirring pill	To place in the chamber for stirring
1	I2C 20x4 LCD module	LCD display
1	4×4 Membrane Keypad	Keypad
1	DS3231 RTC module	Real-time clock module
1	SPI SD card shield	SD card module
1	Clear-glass Test Tube	Chamber of the device
1	Rubber lid for test tubes	To close the chamber
3	14 Gauge Needles	To insert in the rubber lid
3	Luer Connectors	To connects tubes to needles
	Plastic tubes	for hydraulic connections

Table A.1: Part List

Group	Part Name	Description
Chamber	Chamber_board_holder.stl	Optical density board sliding holder
Chamber	Chamber_bottom.stl	Bottom part of the chamber
Chamber	Chamber_top.stl	Top part of the chamber
Chamber	Stirrer_DC_support.stl	Support for the DC motor for the stirring
Chamber	Stirrer_holder.stl	Bottom part of the chamber with room for the magnets
Chamber		Magnetic stirrer
Syringe Pump	SyringePump_holder.stl	Syringe holder bottom part
Syringe Pump	SyringePump_holder_top.stl	Syringe holder top part
Syringe Pump	SyringePump_servo_slider_holder.stl	Slider and Servo motor holder
Syringe Pump	SyringePump_slider.stl	Slider that moves the syringe
Pinch Valve	PinchValve_servo_slider_holder.stl	Body of the valve and Servo Motor Holder
Pinch Valve	PinchValve_slider.stl	Slider that opens and closes the ways
Peristaltic Pump	PeristalticPump.stl	Body of the Planetary peristaltic pump to be mounted on the servo motor.

Table A.2: 3D Printed Part List

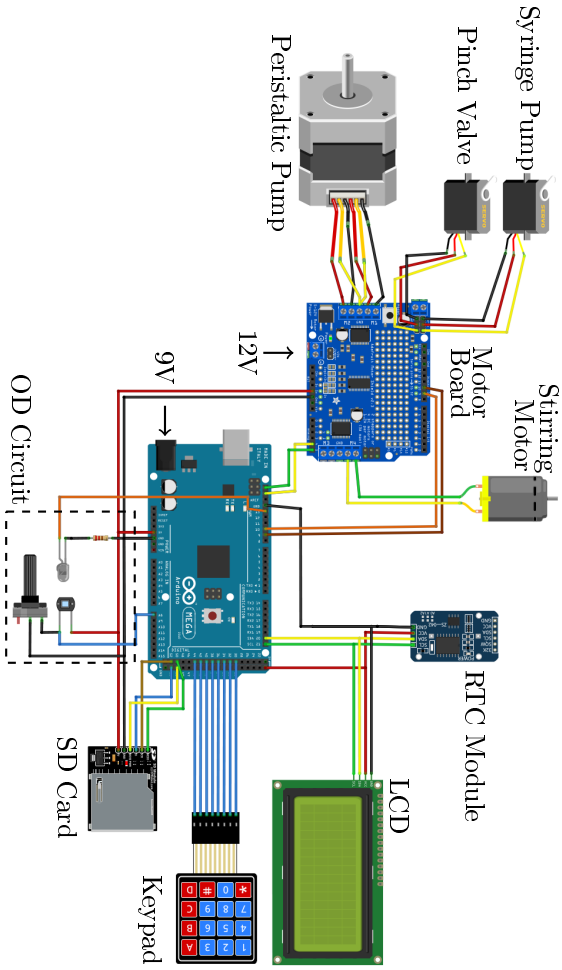

Figure A.1: Sketch of the connections of the modules that compose the turbidostat.

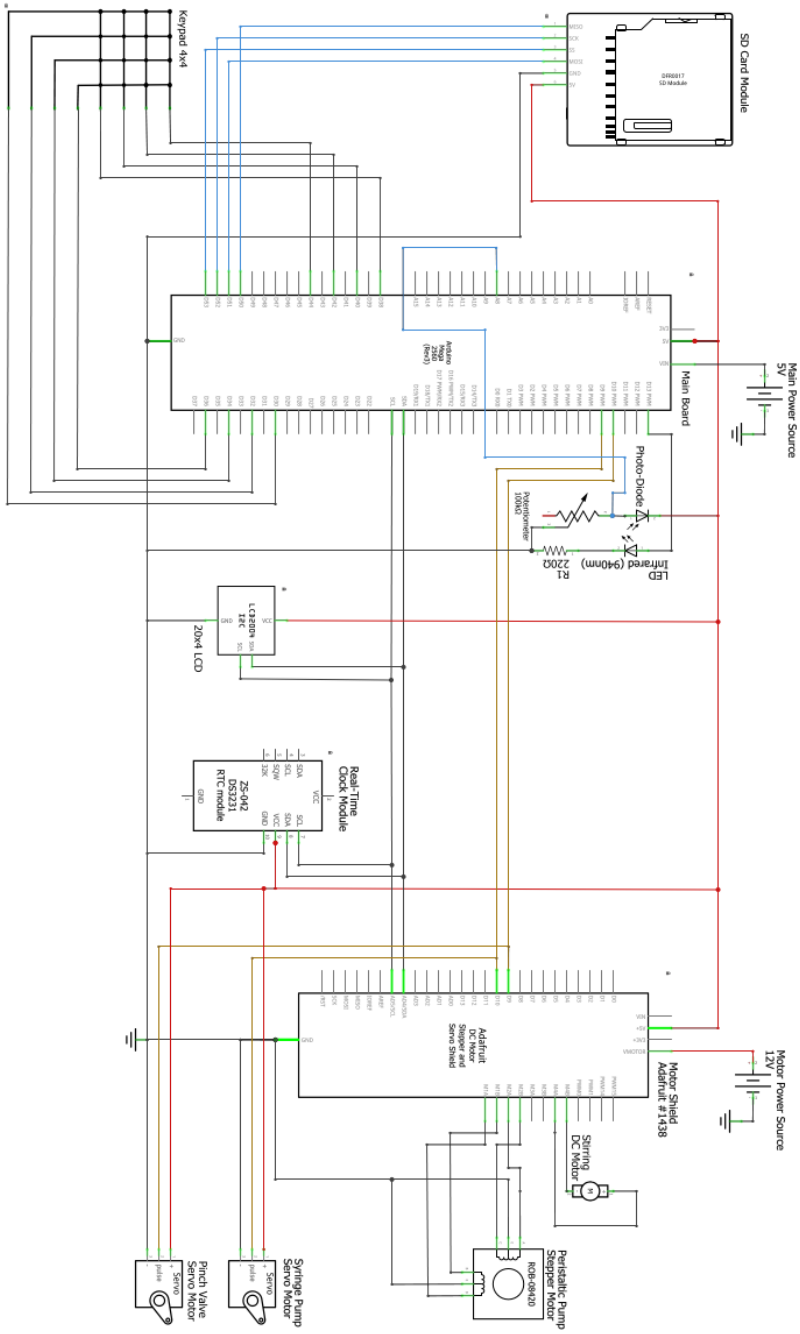

Figure A.2: Electrical connection diagram of the turbidostat we proposed.

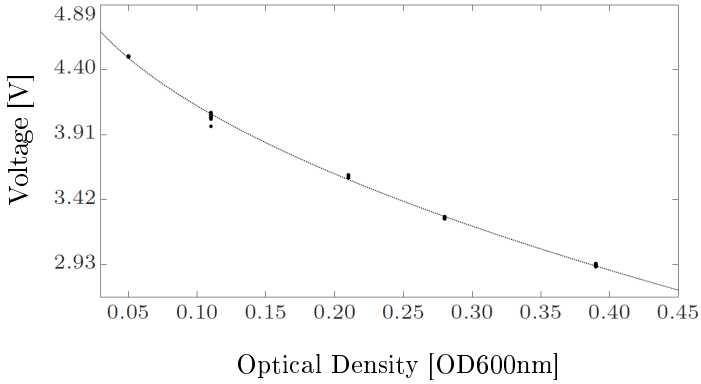

Figure A.3: Calibration of the OD reading. Black dots represent the value of the voltage against the OD for 5 different samples. Dotted line is a 2nd order polynomial obtained from data fitting.

OD600	Mean Voltage [V]	σ^2
0.05	4.50	0.0024
0.11	4.05	0.0217
0.21	3.60	0.0077
0.28	3.28	0.0054
0.39	2.93	0.0071

Table A.3: OD calibration Table

Calibration of the optical density measure circuit

Calibration experiments were conducted to reconstruct the relationship between voltage and optical density. In particular, 25 voltage measurements of 5 different samples (whose OD was measured independently using a spectrophotometer - WPA CO 8000 Cell Density Meter) were performed. The test samples, together with the results of the experiment, are reported in Table A.3. A 2nd-order polynomial was used to interpolate the data points and obtain the voltage-OD relationship; the result is reported in Figure A.3. To validate the interpolated curve, the mean OD readings of the turbidostat were compared to those measured by the spectrophotometer for samples with ODs different from those used for calibration. The results are reported in Table A.4 confirming that the calibration is extremely precise for OD600nm values between 0.05-0.2, which is the range the turbidostat we designed typically work within.

The conversion formula we fitted is a 2^{nd} order polynomial curve whose parameters are $a_0 \approx 1.88$, $a_1 \approx -3.43 \cdot 10^{-3}$, $a_2 \approx 1.56 \cdot 10^{-6}$.

OD600	Mean Read OD	Mean Reading [V]
0.07	0.0597	4.40
0.12	0.1053	4.09
0.15	0.1366	3.92
0.26	0.3174	3.16
0.37	0.4522	2.73

Table A.4: OD Validation Table

Bibliography

[1] Arduino AG. Arduino. https://www.arduino.cc/, 2021. Online, accessed 1st April 2021.

[2] Deepak K. Agrawal, Ryan Marshall, Vincent Noireaux, and Eduardo D. Sontag. In vitro implementation of robust gene regulation in a synthetic biomolecular integral controller. *Nature Communications*, 10(5760):1–12, 2019.

[3] Réka Albert and Albert-László Barabási. Statistical mechanics of complex networks. *Reviews of modern physics*, 74(1):47, 2002.

[4] Razan N Alnahhas, James J Winkle, Andrew J Hirning, Bhargav Karamched, William Ott, Kresimir Josic, and Matthew R Bennett. Spatiotemporal dynamics of synthetic microbial consortia in microfluidic devices. *ACS synthetic biology*, 8(9):2051–2058, 2019.

[5] Uri Alon. *An introduction to systems biology: design principles of biological circuits*. CRC press, 2006.

[6] Fabio Annunziata, Antoni Matyjaszkiewicz, Gianfranco Fiore, Claire S Grierson, Lucia Marucci, Mario di Bernardo, and Nigel J Savery. An orthogonal multi-input integration system to control gene expression in escherichia coli. *ACS synthetic biology*, 6(10):1816–1824, 2017.

[7] Stephanie K Aoki, Gabriele Lillacci, Ankit Gupta, Armin Baumschlager, David Schweingruber, and Mustafa Khammash. A universal biomolecular integral feedback controller for robust perfect adaptation. *Nature*, 570(7762):533–537, 2019.

[8] Pierre Apkarian and Richard J Adams. Advanced gain-scheduling techniques for uncertain systems. In *Advances in linear matrix inequality methods in control*, pages 209–228. SIAM, 2000.

[9] Murat Arcak. Pattern formation by lateral inhibition in large-scale networks of cells. *IEEE Transactions on Automatic Control*, 58(5):1250–1262, 2012.

[10] Robert A. Armstrong and Richard McGehee. Competitive Exclusion. *The American Naturalist*, 115(2):151–170, 1980.

[11] Frederick K Balagaddé, Hao Song, Jun Ozaki, Cynthia H Collins, Matthew Barnet, Frances H Arnold, Stephen R Quake, and Lingchong You. A synthetic escherichia coli predator–prey ecosystem. *Molecular systems biology*, 4(1):187, 2008.

[12] Caleb J Bashor, Noah C Helman, Shude Yan, and Wendell A Lim. Using engineered scaffold interactions to reshape map kinase pathway signaling dynamics. *Science*, 319(5869):1539–1543, 2008.

[13] Georges Bastin. *On-line estimation and adaptive control of bioreactors*, volume 1. Elsevier, 2013.

[14] Attila Becskei and Luis Serrano. Engineering stability in gene networks by autoregulation. *Nature*, 405(6786):590–593, 2000.

[15] Steven A Benner and A Michael Sismour. Synthetic biology. *Nature Reviews Genetics*, 6(7):533–543, 2005.

[16] Philip Bittihn, M Omar Din, Lev S Tsimring, and Jeff Hasty. Rational engineering of synthetic microbial systems: from single cells to consortia. *Current opinion in microbiology*, 45:92–99, 2018.

[17] Corentin Briat, Ankit Gupta, and Mustafa Khammash. Antithetic integral feedback ensures robust perfect adaptation in noisy biomolecular networks. *Cell systems*, 2(1):15–26, 2016.

[18] Alina Burmeister, Fabienne Hilgers, Annika Langner, Christoph Westerwalbesloh, Yannic Kerkhoff, Niklas Tenhaef, Thomas Drepper, Dietrich Kohlheyer, Eric von Lieres, Stephan Noack, et al. A microfluidic cocultivation platform to investigate microbial interactions at defined microenvironments. *Lab on a Chip*, 19(1):98–110, 2019.

[19] Olguta Buse, Rodrigo Pérez, and Alexey Kuznetsov. Dynamical properties of the repressilator model. *Physical Review E*, 81(6):066206, 2010.

[20] Sa Cai, Xiaobing Fu, and Zhiyong Sheng. Dedifferentiation: A New Approach in Stem Cell Research. *BioScience*, 57(8):655–662, 2007.

[21] D Ewen Cameron, Caleb J Bashor, and James J Collins. A brief history of synthetic biology. *Nature Reviews Microbiology*, 12(5):381–390, 2014.

[22] Tomás Caraballo, Javier Lüpez-de-la Cruz, and Alain Rapaport. Modeling bounded random fluctuations in biological systems: application to the chemostat model with two species. *IFAC-PapersOnLine*, 52(26):187–192, 2019.

[23] Stefano Cardinale and Adam Paul Arkin. Contextualizing context for synthetic biology–identifying causes of failure of synthetic biological systems. *Biotechnology journal*, 7(7):856–866, 2012.

[24] Madalena Chaves and Hidde de Jong. Qualitative modeling, analysis and control of synthetic regulatory circuits. In *Synthetic Gene Circuits*, pages 1–40. Springer, 2021.

[25] Madalena Chaves and Jean-Luc Gouzé. Exact control of genetic networks in a qualitative framework: the bistable switch example. *Automatica*, 47(6):1105–1112, 2011.

[26] Vijaysekhar Chellaboina, Sanjay P Bhat, Wassim M Haddad, and Dennis S Bernstein. Modeling and analysis of mass-action kinetics. *IEEE Control Systems Magazine*, 29(4):60–78, 2009.

[27] Luonan Chen, Ruiqi Wang, Chunguang Li, and Kazuyuki Aihara. *Modeling biomolecular networks in cells*. Springer-Verlag London, 2010.

[28] Ye Chen, Jae Kyoung Kim, Andrew J Hirning, Krešimir Josić, and Matthew R Bennett. Emergent genetic oscillations in a synthetic microbial consortium. *Science*, 349(6251):986–989, 2015.

[29] Francis HC Crick. On protein synthesis. *Symposia of the Society for Experimental Biology*, 12(138-63):8, 1958.

[30] Francis HC Crick. Central dogma of molecular biology. *Nature*, 227(5258):561–563, 1970.

[31] Hernán De Battista, Martín Jamilis, Fabricio Garelli, and Jesús Picó. Global stabilisation of continuous bioreactors: Tools for analysis and design of feeding laws. *Automatica*, 89:340–348, 2018.

[32] Hernán De Battista, Enric Picó-Marco, Fernando N Santos-Navarro, and Jesús Picó. Output feedback linearization of turbidostats after time scaling. *IEEE Transactions on Control Systems Technology*, 27(4):1668–1676, 2018.

[33] Patrick De Leenheer and Hal Smith. Feedback control for chemostat models. *Journal of Mathematical Biology*, 46(1):48–70, 2003.

[34] Alex Reis de Souza, Denis Efimov, Andrey Polyakov, and Jean-Luc Gouzé. Robust stabilization of competing species in the chemostat. *Journal of Process Control*, 87:138–146, 2020.

[35] Karl Deisseroth. Optogenetics. *Nature methods*, 8(1):26–29, 2011.

[36] Domitilla Del Vecchio, Aaron J Dy, and Yili Qian. Control theory meets synthetic biology. *Journal of The Royal Society Interface*, 13(120):20160380, 2016.

[37] Domitilla Del Vecchio, Yili Qian, Richard M Murray, and Eduardo D Sontag. Future systems and control research in synthetic biology. *Annual Reviews in Control*, 45:5–17, 2018.

[38] Denis Dochain, Patrick De Leenheer, and Alain Rapaport. About transgressive over-yielding in the chemostat. *IFAC Proceedings Volumes*, 45(2):653–658, 2012.

[39] Michael B Elowitz and Stanislas Leibler. A synthetic oscillatory network of transcriptional regulators. *Nature*, 403(6767):335–338, 2000.

[40] Frank Emmert-Streib, Matthias Dehmer, and Benjamin Haibe-Kains. Gene regulatory networks and their applications: understanding biological and medical problems in terms of networks. *Frontiers in cell and developmental biology*, 2:38, 2014.

[41] Peyman Mohajerin Esfahani, Andreas Milias-Argeitis, and Debasish Chatterjee. Analysis of controlled biological switches via stochastic motion planning. In *2013 European Control Conference (ECC)*, pages 93–98. IEEE, 2013.

[42] Alex JH Fedorec, Behzad D Karkaria, Michael Sulu, and Chris P Barnes. Single strain control of microbial consortia. *Nature communications*, 12(1):1–12, 2021.

[43] Davide Fiore, Fabio Della Rossa, Agostino Guarino, and Mario di Bernardo. Feedback ratiometric control of two microbial populations in a single chemostat. *bioRxiv*, 2021.03.05.434159, 2021.

[44] Davide Fiore, Agostino Guarino, and Mario di Bernardo. Analysis and Control of Genetic Toggle Switches Subject to Periodic Multi-Input Stimulation. *IEEE Control Systems Letters*, 3(2):278–283, 2019.

[45] Davide Fiore, Davide Salzano, Enric Cristòbal-Cóppulo, Josep M Olm, and Mario di Bernardo. Multicellular feedback control of a genetic toggle-switch in microbial consortia. *IEEE Control Systems Letters*, 5(1):151–156, 2020.

[46] Gianfranco Fiore, Antoni Matyjaszkiewicz, Fabio Annunziata, Claire Grierson, Nigel J Savery, Lucia Marucci, and Mario di Bernardo. In-silico analysis and implementation of a multicellular feedback control strategy in a synthetic bacterial consortium. *ACS Synthetic Biology*, 6(3):507–517, 2017.

[47] Gianfranco Fiore, Giansimone Perrino, Mario di Bernardo, and Diego di Bernardo. In vivo real-time control of gene expression: a comparative analysis of feedback control strategies in yeast. *ACS Synthetic Biology*, 5(2):154–162, 2015.

[48] Chiara Fracassi, Lorena Postiglione, Gianfranco Fiore, and Diego di Bernardo. Automatic control of gene expression in mammalian cells. *ACS synthetic biology*, 5(4):296–302, 2016.

[49] Limor (ladyada) Fried. Adafruit motor shield v2. https://learn.adafruit.com/adafruit-motor-shield-v2-for-arduino, 2013. Online, accessed 1st April 2021.

[50] Ari E Friedland, Timothy K Lu, Xiao Wang, David Shi, George Church, and James J Collins. Synthetic gene networks that count. *Science*, 324(5931):1199–1202, 2009.

[51] Chikara Furusawa and Kunihiko Kaneko. A dynamical-systems view of stem cell biology. *Science*, 338(6104):215–217, 2012.

[52] Jordi Garcia-Ojalvo, Michael B Elowitz, and Steven H Strogatz. Modeling a synthetic multicellular clock: repressilators coupled by quorum sensing. *Proceedings of the National Academy of Sciences*, 101(30):10955–10960, 2004.

[53] Timothy S Gardner, Charles R Cantor, and James J Collins. Construction of a genetic toggle switch in Escherichia coli. *Nature*, 403(6767):339–342, 2000.

[54] M Gen and R Cheng. *Genetic algorithms and engineering optimization*. John Wiley & Sons, 2000.

[55] Thomas E Gorochowski, Antoni Matyjaszkiewicz, Thomas Todd, Neeraj Oak, Kira Kowalska, Stephen Reid, Krasimira T Tsaneva-Atanasova, Nigel J Savery, Claire S Grierson, and Mario di Bernardo. Bsim: an agent-based tool for modeling bacterial populations in systems and synthetic biology. *PLOS One*, 7(8):e42790, 2012.

[56] Agostino Guarino, Davide Fiore, and Mario di Bernardo. In-silico feedback control of a mimo synthetic toggle switch via pulse-width modulation. In *2019 18th European Control Conference (ECC)*, pages 680–685. IEEE, 2019.

[57] Agostino Guarino, Davide Fiore, Davide Salzano, and Mario di Bernardo. Balancing cell populations endowed with a synthetic toggle switch via adaptive pulsatile feedback control. *ACS synthetic biology*, 9(4):793–803, 2020.

[58] Agostino Guarino, Barbara Shannon, Lucia Marucci, Claire Grierson, Nigel Savery, and Mario di Bernardo. A low-cost, open-source turbidostat design for in-vivo control experiments in synthetic biology. *IFAC-PapersOnLine*, 52(26):244–248, 2019.

[59] Călin C Guet, Michael B Elowitz, Weihong Hsing, and Stanislas Leibler. Combinatorial synthesis of genetic networks. *Science*, 296(5572):1466–1470, 2002.

[60] Jérôme Harmand, Alain Rapaport, and Tibault Nidelet. About overyielding with mixed cultures in batch processes. *IFAC-PapersOnLine*, 52(26):163–168, 2019.

[61] Navarro Herrero, Jose Luis Navarro Herrero, Jesus Pico Marco, Jose Manuel Bruno Barcena, Salvador Valles Albentosa, and Enrique Pico Marco. Online method and equipment for detecting, determining the evolution and quantifying a microbial biomass and other substances that absorb light along the spectrum during the development of biotechnological. *United States Patent No. US 6,975,403 B2*, Date of Patent: Dec 13, 2005.

[62] Leonard A Herzenberg, David Parks, Bita Sahaf, Omar Perez, Mario Roederer, and Leonore A Herzenberg. The history and future of the fluorescence activated cell sorter and flow cytometry: a view from Stanford. *Clinical chemistry*, 48(10):1819–1827, 2002.

[63] Desmond J Higham. An algorithmic introduction to numerical simulation of stochastic differential equations. *SIAM Review*, 43(3):525–546, 2001.

[64] Patrick Hillenbrand, Georg Fritz, and Ulrich Gerland. Biological Signal Processing with a Genetic Toggle Switch. *PLOS One*, 8(7):e68345, 2013.

[65] Stefan A Hoffmann, Christian Wohltat, Kristian M Müller, and Katja M Arndt. A user-friendly, low-cost turbidostat with versatile growth rate estimation based on an extended kalman filter. *PLoS One*, 12(7):e0181923, 2017.

[66] Jan Homolak, Monika Mudrovčić, Barbara Vukić, and Karlo Toljan. Circadian rhythm and alzheimer's disease. *Medical Sciences*, 6(3):52, 2018.

[67] Victoria Hsiao, Anandh Swaminathan, and Richard M. Murray. Control Theory for Synthetic Biology: Recent Advances in System Characterization, Control Design, and Controller Implementation for Synthetic Biology. *IEEE Control Systems*, 38(3):32–62, 2018.

[68] Sze-Bi Hsu, S Hubbell, and Paul Waltman. A mathematical theory for single-nutrient competition in continuous cultures of micro-organisms. *SIAM Journal on Applied Mathematics*, 32(2):366–383, 1977.

[69] Hawoong Jeong, Bálint Tombor, Réka Albert, Zoltan N Oltvai, and Albert-László Barabási. The large-scale organization of metabolic networks. *Nature*, 407(6804):651–654, 2000.

[70] Kenneth A Johnson and Roger S Goody. The original michaelis constant: translation of the 1913 michaelis–menten paper. *Biochemistry*, 50(39):8264–8269, 2011.

[71] Mads Kaern, William J Blake, and James J Collins. The engineering of gene regulatory networks. *Annual review of biomedical engineering*, 5(1):179–206, 2003.

[72] Pyotr Leonidovich Kapitza. Dynamic stability of a pendulum with an oscillating point of suspension. *Journal of experimental and theoretical physics*, 21(5):588–597, 1951.

[73] Ciarán L Kelly, Andreas W K Harris, Harrison Steel, Edward J Hancock, John T Heap, and Antonis Papachristodoulou. Synthetic negative feedback circuits using engineered small RNAs. *Nucleic Acids Research*, 46(18):9875–9889, 2018.

[74] Ahmad S Khalil and James J Collins. Synthetic biology: applications come of age. *Nature Reviews Genetics*, 11(5):367–379, 2010.

[75] Hassan K Khalil. *Nonlinear systems*. Prentice Hall, 3rd edition, 2002.

[76] Mustafa Khammash, Mario di Bernardo, and Diego di Bernardo. Cybergenetics: Theory and methods for genetic control system. In *2019 IEEE 58th Conference on Decision and Control (CDC)*, pages 916–926. IEEE, 2019.

[77] MH Kim, M Liang, QP He, and J Wang. A novel bioreactor to study the dynamics of co-culture systems. *Biochemical Engineering Journal*, 107:52–60, 2016.

[78] Hiroaki Kitano. Computational systems biology. *Nature*, 420(6912):206–210, 2002.

[79] Hiroaki Kitano. Systems biology: a brief overview. *Science*, 295(5560):1662–1664, 2002.

[80] József Klespitz and Levente Kovács. Peristaltic pumps—a review on working and control possibilities. In *2014 IEEE 12th International Symposium on Applied Machine Intelligence and Informatics (SAMI)*, pages 191–194. IEEE, 2014.

[81] Yuri A Kuznetsov, Sergio Rinaldi, and Alessandra Gragnani. One-parameter bifurcations in planar filippov systems. *International Journal of Bifurcation and chaos*, 13(08):2157–2188, 2003.

[82] Roberta Kwok. Five hard truths for synthetic biology. *Nature News*, 463(7279):288–290, 2010.

[83] Emmett Lalish. Gear bearing. http://www.thingiverse.com/thing:53451. Online, accessed 1st April 2021.

[84] Michel Laurent and Nicolas Kellershohn. Multistability: a major means of differentiation and evolution in biological systems. *Trends in Biochemical Sciences*, 24(11):418–422, 1999.

[85] Hannah C Leeson, Tailoi Chan-Ling, Michael D Lovelace, Jeremy D Brownlie, Michael W Weible II, and Ben J Gu. Real-time live-cell flow cytometry to investigate calcium influx, pore formation, and phagocytosis by p2x7 receptors in adult neural progenitor cells. *JoVE (Journal of Visualized Experiments)*, 146:e59313, 2019.

[86] Douglas J Leith and William E Leithead. Survey of gain-scheduling analysis and design. *International journal of control*, 73(11):1001–1025, 2000.

[87] Michael Levine and Eric H Davidson. Gene regulatory networks for development. *Proceedings of the National Academy of Sciences*, 102(14):4936–4942, 2005.

[88] Yueqin Li, Ata Mahjoubfar, Claire Lifan Chen, Kayvan Reza Niazi, Li Pei, and Bahram Jalali. Deep cytometry: deep learning with real-time inference in cell sorting and flow cytometry. *Scientific reports*, 9(1):1–12, 2019.

[89] Gabriele Lillacci, Stephanie Aoki, David Schweingruber, and Mustafa Khammash. A synthetic integral feedback controller for robust tunable regulation in bacteria. *bioRxiv*, 170951, 2017.

[90] Zedao Liu, Jizhong Zhang, Jiao Jin, Zilong Geng, Qingsheng Qi, and Quanfeng Liang. Programming bacteria with light-sensors and applications in synthetic biology. *Frontiers in microbiology*, 9:2692, 2018.

[91] RW Lovitt and JWT Wimpenny. The gradostat: a bidirectional compound chemostat and its application in microbiological research. *Microbiology*, 127(2):261–268, 1981.

[92] Jean-Baptiste Lugagne. *Real-time control of a genetic toggle switch*. PhD thesis, Université Sorbonne Paris Cité, 2016.

[93] Jean-Baptiste Lugagne, Sebastián Sosa Carrillo, Melanie Kirch, Agnes Köhler, Gregory Batt, and Pascal Hersen. Balancing a genetic toggle switch by real-time feedback control and periodic forcing. *Nature communications*, 8(1):1–8, 2017.

[94] Nicholas M Luscombe, Dov Greenbaum, and Mark Gerstein. What is bioinformatics? a proposed definition and overview of the field. *Methods of information in medicine*, 40(04):346–358, 2001.

[95] Javier Macía, Francesc Posas, and Ricard V Solé. Distributed computation: the new wave of synthetic biology devices. *Trends in biotechnology*, 30(6):342–349, 2012.

[96] Dominick Matteau, Vincent Baby, Stéphane Pelletier, and Sébastien Rodrigue. A small-volume, low-cost, and versatile continuous culture device. *PLoS One*, 10(7):e0133384, 2015.

[97] Marco Mauri, Jean-Luc Gouzé, Hidde De Jong, and Eugenio Cinquemani. Enhanced production of heterologous proteins by a synthetic microbial community: Conditions and trade-offs. *PLoS computational biology*, 16(4):e1007795, 2020.

[98] Harley H McAdams and Adam Arkin. Gene regulation: Towards a circuit engineering discipline. *Current Biology*, 10(8):R318–R320, 2000.

[99] Harley H McAdams and Lucy Shapiro. Circuit simulation of genetic networks. *Science*, 269(5224):650–656, 1995.

[100] Anna M McGeachy, Zuriah A Meacham, and Nicholas T Ingolia. An accessible continuous-culture turbidostat for pooled analysis of complex libraries. *ACS synthetic biology*, 8(4):844–856, 2019.

[101] Justin Melendez, Michael Patel, Benjamin L Oakes, Ping Xu, Patrick Morton, and Megan N McClean. Real-time optogenetic control of intracellular protein concentration in microbial cell cultures. *Integrative Biology*, 6(3):366–372, 2014.

[102] Andreas Milias-Argeitis, Marc Rullan, Stephanie K Aoki, Peter Buchmann, and Mustafa Khammash. Automated optogenetic feedback control for precise and robust regulation of gene expression and cell growth. *Nature communications*, 7(1):1–11, 2016.

[103] Andreas Milias-Argeitis, Sean Summers, Jacob Stewart-Ornstein, Ignacio Zuleta, David Pincus, Hana El-Samad, Mustafa Khammash, and John Lygeros. In silico feedback for in vivo regulation of a gene expression circuit. *Nature biotechnology*, 29(12):1114–1116, 2011.

[104] Melissa B Miller and Bonnie L Bassler. Quorum sensing in bacteria. *Annual Reviews in Microbiology*, 55(1):165–199, 2001.

[105] Petros Mina, Krasimira Tsaneva-Atanasova, and Mario di Bernardo. Entrainment and control of bacterial populations: an in silico study over a spatially extended agent based model. *ACS Synthetic Biology*, 5(7):639–653, 2016.

[106] Jacques Monod. The growth of bacterial cultures. *Annual Reviews in Microbiology*, 3(1):371–394, 1949.

[107] Vivek K Mutalik, Joao C Guimaraes, Guillaume Cambray, Quynh-Anh Mai, Marc Juul Christoffersen, Lance Martin, Ayumi Yu, Colin Lam, Cesar Rodriguez, Gaymon Bennett, et al. Quantitative estimation of activity and quality for collections of functional genetic elements. *Nature methods*, 10(4):347, 2013.

[108] Evangelos-Marios Nikolados, Andrea Y Weiße, Francesca Ceroni, and Diego A Oyarzún. Growth defects and loss-of-function in synthetic gene circuits. *ACS synthetic biology*, 8(6):1231–1240, 2019.

[109] Evan J Olson, Lucas A Hartsough, Brian P Landry, Raghav Shroff, and Jeffrey J Tabor. Characterizing bacterial gene circuit dynamics with optically programmed gene expression signals. *Nature methods*, 11(4):449–455, 2014.

[110] Evan J Olson and Jeffrey J Tabor. Optogenetic characterization methods overcome key challenges in synthetic and systems biology. *Nature chemical biology*, 10(7):502–511, 2014.

[111] Bernadett Papp and Kathrin Plath. Reprogramming to pluripotency: stepwise resetting of the epigenetic landscape. *Cell research*, 21(3):486–501, 2011.

[112] Helen Pearson. What is a gene? *Nature*, 441(7092):398–401, 2006.

[113] Giansimone Perrino, Cathal Wilson, Marco Santorelli, and Diego di Bernardo. Quantitative characterization of α-synuclein aggregation in living cells through automated microfluidics feedback control. *Cell reports*, 27(3):916–927, 2019.

[114] Lorena Postiglione, Sara Napolitano, Elisa Pedone, Daniel L Rocca, Francesco Aulicino, Marco Santorelli, Barbara Tumaini, Lucia Marucci, and Diego di Bernardo. Regulation of gene expression and signaling pathway activity in mammalian cells by automated microfluidics feedback control. *ACS synthetic biology*, 7(11):2558–2565, 2018.

[115] EO Powell. Criteria for the growth of contaminants and mutants in continuous culture. *Microbiology*, 18(1):259–268, 1958.

[116] Erzsébet Ravasz, Anna Lisa Somera, Dale A Mongru, Zoltán N Oltvai, and Albert-László Barabási. Hierarchical organization of modularity in metabolic networks. *science*, 297(5586):1551–1555, 2002.

[117] Xinying Ren, Ania-Ariadna Baetica, Anandh Swaminathan, and Richard M Murray. Population regulation in microbial consortia using dual feedback control. In *2017 IEEE 56th Annual Conference on Decision and Control (CDC)*, pages 5341–5347. IEEE, 2017.

[118] Mehdi Sadeghpour, Alan Veliz-Cuba, Gábor Orosz, Krešimir Josić, and Matthew R Bennett. Bistability and oscillations in co-repressive synthetic microbial consortia. *Quantitative Biology*, 5(1):55–66, 2017.

[119] Alok J Saldanha, Matthew J Brauer, and David Botstein. Nutritional homeostasis in batch and steady-state culture of yeast. *Molecular biology of the cell*, 15(9):4089–4104, 2004.

[120] Davide Salzano, Davide Fiore, and Mario di Bernardo. Ratiometric control for differentiation of cell populations endowed with synthetic toggle switches. In *2019 IEEE 58th Conference on Decision and Control (CDC)*, pages 927–932. IEEE, 2019.

[121] Spencer R Scott, M Omar Din, Philip Bittihn, Liyang Xiong, Lev S Tsimring, and Jeff Hasty. A stabilized microbial ecosystem of self-limiting bacteria using synthetic quorum-regulated lysis. *Nature microbiology*, 2(8):1–9, 2017.

[122] Shai S Shen-Orr, Ron Milo, Shmoolik Mangan, and Uri Alon. Network motifs in the transcriptional regulation network of escherichia coli. *Nature genetics*, 31(1):64–68, 2002.

[123] Sae Shimizu-Sato, Enamul Huq, James M Tepperman, and Peter H Quail. A light-switchable gene promoter system. *Nature biotechnology*, 20(10):1041–1044, 2002.

[124] Velia Siciliano, Immacolata Garzilli, Chiara Fracassi, Stefania Criscuolo, Simona Ventre, and Diego di Bernardo. Mirnas confer phenotypic robustness to gene networks by suppressing biological noise. *Nature communications*, 4(1):1–7, 2013.

[125] Hal L Smith. Competitive coexistence in an oscillating chemostat. *SIAM Journal on Applied Mathematics*, 40(3):498–522, 1981.

[126] Aivar Sootla and Damien Ernst. Pulse-based control using koopman operator under parametric uncertainty. *IEEE Transactions on Automatic Control*, 63(3):791–796, 2017.

[127] Aivar Sootla, Alexandre Mauroy, and Damien Ernst. Optimal control formulation of pulse-based control using koopman operator. *Automatica*, 91:217–224, 2018.

[128] Aivar Sootla, Diego Oyarzún, David Angeli, and Guy-Bart Stan. Shaping pulses to control bistable systems: Analysis, computation and counterexamples. *Automatica*, 63:254–264, 2016.

[129] Aivar Sootla, Natalja Strelkowa, Damien Ernst, Mauricio Barahona, and Guy-Bart Stan. Toggling a genetic switch using reinforcement learning. *arXiv*, 1303.3183, 2015.

[130] Harrison Steel, Robert Habgood, Ciarán L Kelly, and Antonis Papachristodoulou. Chi. bio: An open-source automated experimental platform for biological science research. *bioRxiv*, 796516, 2019.

[131] Harrison Steel, Robert Habgood, Ciarán L Kelly, and Antonis Papachristodoulou. In situ characterisation and manipulation of biological systems with chi. bio. *PLoS biology*, 18(7):e3000794, 2020.

[132] Harrison Steel, Robert Habgood, Anthonis Papachristodoulou, and Ciarán L Kelly. Chi.bio. https://chi.bio/, 2021. Online, accessed 1st April 2021.

[133] Zuzanna Szymańska, Maciej Cytowski, Elaine Mitchell, Cicely K Macnamara, and Mark AJ Chaplain. Computational modelling of cancer development and growth: modelling at multiple scales and multiscale modelling. *Bulletin of mathematical biology*, 80(5):1366–1403, 2018.

[134] Chris N. Takahashi, Aaron W. Miller, Felix Ekness, Maitreya J. Dunham, and Eric Klavins. A low cost, customizable turbidostat for use in synthetic circuit characterization. *ACS Synthetic Biology*, 4(1):32–38, 2015.

[135] Fatima-Zahra Tani, Alain Rapaport, and Térence Bayen. A hybrid control against species invasion in the chemostat. In *2019 IEEE 58th Conference on Decision and Control (CDC)*, pages 2814–2819. IEEE, 2019.

[136] RN Tchuraev, IV Stupak, TS Tropynina, and EE Stupak. Epigenes: design and construction of new hereditary units. *FEBS letters*, 486(3):200–202, 2000.

[137] Mukund Thattai and Alexander Van Oudenaarden. Intrinsic noise in gene regulatory networks. *Proceedings of the National Academy of Sciences*, 98(15):8614–8619, 2001.

[138] Tianhai Tian and Kevin Burrage. Stochastic models for regulatory networks of the genetic toggle switch. *Proceedings of the National Academy of Sciences*, 103(22):8372–8377, 2006.

[139] Katrin Tomson, Jill Barber, and Kalju Vanatalu. Adaptastat—a new method for optimising of bacterial growth conditions in continuous culture: Interactive substrate limitation based on dissolved oxygen measurement. *Journal of microbiological methods*, 64(3):380–390, 2006.

[140] Mark K Transtrum and Peng Qiu. Bridging mechanistic and phenomenological models of complex biological systems. *PLoS computational biology*, 12(5):e1004915, 2016.

[141] Ping Wang, Lydia Robert, James Pelletier, Wei Lien Dang, Francois Taddei, Andrew Wright, and Suckjoon Jun. Robust growth of escherichia coli. *Current Biology*, 20(12):1099–1103, 2010.

[142] Wei-Chih Wang. Optical detectors. National Tsinghua University, Available at https://depts.washington.edu/mictech/optics/me557/detector.pdf, 2011. Online, accessed 1st April 2021.

[143] Terence G Watson. The present status and future prospects of the turbidostat. *J. appl. Chem. Biotechnol*, 22:229–243, 1972.

[144] Ron Weiss and Subhyu Basu. The device physics of cellular logic gates. In *NSC-1: The First Workshop of Non-Silicon Computing. Boston, Massachusetts*, 2002.

[145] Andrea Y Weiße, Diego A Oyarzún, Vincent Danos, and Peter S Swain. Mechanistic links between cellular trade-offs, gene expression, and growth. *Proceedings of the National Academy of Sciences*, 112(9):E1038–E1047, 2015.

[146] Brandon G Wong, Christopher P Mancuso, Szilvia Kiriakov, Caleb J Bashor, and Ahmad S Khalil. Precise, automated control of conditions for high-throughput growth of yeast and bacteria with evolver. *Nature biotechnology*, 36(7):614–623, 2018.

[147] Min Wu, Ri-Qi Su, Xiaohui Li, Tom Ellis, Ying-Cheng Lai, and Xiao Wang. Engineering of regulated stochastic cell fate determination. *Proceedings of the National Academy of Sciences*, 110(26):10610–10615, 2013.

[148] Wen Xiong and James E. Ferrell. A positive-feedback-based bistable 'memory module' that governs a cell fate decision. *Nature*, 426(6965):460–465, 2003.

[149] Lingchong You, Robert Sidney Cox, Ron Weiss, and Frances H. Arnold. Programmed population control by cell–cell communication and regulated killing. *Nature*, 43(20):868–871, 2004.

[150] Kelly A. Zalocusky, Lief E. Fenno, and Karl Deisseroth. Current challenges in optogenetics. https://www.sfn.org/~/media/SfN/Documents/Short%20Courses/2013%20Short%20Course%20I/SC1%20Deisseroth.ashx, 2013. Online, accessed 1st April 2021.